

# Cavity QED with Erbium Doped Crystals Coupled to Microwave Resonators

Mikrowellen Resonator-Quantenelektrodynamik  
mit Erbium-dotierten Kristallen

Master Thesis of

**Andrej Tkalcec**

At the Department of Physics  
Physical Institute (PI):  
Research Group Ustinov

Reviewer: Prof. Dr. Alexey V. Ustinov  
Advisor: Prof. Dr. Pavel A. Bushev

Duration: 17. June 2013 – 16. December 2013



---

I herewith declare that the present thesis is original work written by me alone and that I have indicated completely and precisely all aids used as well as all citations, whether changed or unchanged, of other theses and publications.

**Karlsruhe, 16. December 2013**

.....  
(Andrej Tkalcec)



# Contents

<b>1. Abstract</b>	<b>1</b>
<b>2. Introduction</b>	<b>3</b>
<b>3. Theory</b>	<b>5</b>
3.1. Basics of Electron Spin Resonance (ESR) Spectroscopy . . . . .	5
3.1.1. The g-Factor and Magnetic Resonance . . . . .	5
3.1.2. Effective Spin and the Hyperfine Structure . . . . .	12
3.1.3. The g-Tensor and Anisotropy Effects . . . . .	15
3.1.4. Inhomogeneous Broadening and Spin-Spin Interaction . . . . .	17
3.1.5. Spin-Lattice Interactions . . . . .	20
3.2. Erbium ( $\text{Er}^{3+}$ ) Doped Crystals . . . . .	23
3.2.1. The Lanthanide (4f) Group and Erbium ( $\text{Er}^{3+}$ ) . . . . .	23
3.2.2. Erbium ( $\text{Er}^{3+}$ ) in Host Material YSO ( $\text{Y}_2\text{SiO}_5$ ) . . . . .	24
3.2.3. Erbium ( $\text{Er}^{3+}$ ) in Host Material YAlO ( $\text{YAlO}_3$ ) . . . . .	26
3.3. Waveguide Resonators . . . . .	27
3.3.1. Circuit Model, Q-Factors and the Observed Spectra . . . . .	28
3.3.2. Resonant Frequencies and the TE011 Mode . . . . .	33
3.3.3. Two-Port Networks and External Coupling . . . . .	36
3.4. Cavity Quantum Electrodynamics . . . . .	38
<b>4. Characterization and Measurement of Er:YSO filled Waveguide Resonators</b>	<b>43</b>
4.1. Experimental Setup . . . . .	43
4.2. Waveguide Resonator Version 1 . . . . .	45
4.2.1. Characteristics and Determination of the Resonant Frequencies . . . . .	45
4.2.2. ESR Spectroscopy of 200 ppm Doped Er:YSO at mK Temperatures . . . . .	48
4.3. Waveguide Resonator Version 2 . . . . .	51
4.3.1. Design and Characterization . . . . .	52
4.3.2. ESR Spectroscopy of 200 ppm Doped Er:YSO at mK Temperatures . . . . .	57
4.3.3. ESR Spectroscopy of 50 ppm Doped Er:YSO at mK Temperatures . . . . .	58
4.3.3.1. Strong Coupling . . . . .	68
4.3.3.2. Power Dependence of the Strongly Coupled Transition . . . . .	70
4.3.3.3. Coupling Strength Versus Temperature . . . . .	71
<b>5. Measurements using Superconductive Lumped-Element Resonators</b>	<b>75</b>
5.1. Experimental Setup . . . . .	75
5.2. ESR Spectroscopy of 200 ppm Doped Er:YAlO using a 9 LEKID Resonator . . . . .	76
5.3. ESR Spectroscopy of 200 ppm Doped Er:YAlO using a 3 LEKID Resonator . . . . .	78
5.3.1. Coupling Strength Versus Temperature . . . . .	80
5.3.2. Crystal Impurity ( $\text{Ce}^{3+}$ ) . . . . .	81
<b>6. Summary</b>	<b>83</b>

<b>7. Conclusions and Outlook</b>	<b>85</b>
<b>Bibliography</b>	<b>87</b>
<b>Appendix</b>	<b>91</b>
A. CST Microwave Studio (Simple Manual) . . . . .	91
B. Design Drawings of Waveguide Resonator Version 1 . . . . .	95
C. Design Drawings of Waveguide Resonator Version 2 . . . . .	96
D. Design Drawing of the Sample Holder . . . . .	97
<b>8. Acknowledgments</b>	<b>99</b>

# 1. Abstract

---

Quantum communication offers the exchange of information in an intrinsically secure way, where quantum memories will be an integral part of such a quantum infrastructure. This thesis covers electron spin resonance spectroscopy of erbium doped crystals which could serve as future quantum memories. Using a 3D waveguide resonator coupled to a 50 ppm erbium doped  $\text{Y}_2\text{SiO}_5$  (Er:YSO) crystal, strong coupling of 21 MHz with an inhomogeneous spin linewidth of 18 MHz was observed. Temperature dependent measurements of the coupling strength showed strong coupling up to approximately 700 mK. In addition, a 200 ppm erbium doped  $\text{YAlO}_3$  crystal was coupled to a superconducting lumped element resonator, where strong coupling of 34 MHz with an inhomogeneous spin linewidth of 22 MHz was measured. In contrast to Er:YSO coupled to a waveguide resonator, strong coupling was measured up to approximately 100 mK. Furthermore, the rare earth impurity cerium was observed in the Er: $\text{YAlO}_3$  crystal.



## 2. Introduction

---

Today, nearly for everyone the access and exchange of information e.g. via the internet is obvious. Since the beginning of the 90's of the last century the information network is rapidly growing and efforts have been done to establish fast, easy and secure ways of information exchange. As fast as this information technology is growing, as more difficult it becomes to keep the exchange of information secure.

A way to solve this problem could be found in the discipline of Quantum Communication, which allows the transmission of information in an intrinsically secure way [GT07]. Quantum Communication Networks are able to combine several types of systems which transmit, receive and process information using quantum algorithms [Kim08]. The nodes of such networks can be realized using e.g. superconducting (SC) quantum circuits operating in the GHz frequency range [CW08], whereas fiber optics operating at near infrared can be used to link them over long distances.

An already well established technique in today's telecommunication industry is the usage of the Telecom C-band in optical fibers at a wavelength between 1.530 and 1.565  $\mu\text{m}$ . The so called conventional erbium window provides very low signal attenuation in optical fibers, whereas additionally high performance erbium doped fiber amplifiers are available. Therefore, the usage of the rare earth element erbium ( $\text{Er}^{3+}$ ) embedded in crystalline host materials like yttrium orthosilicate ( $\text{Y}_2\text{SiO}_5$ , YSO) or yttrium orthoaluminate ( $\text{YAlO}_3$ , YAlO) may be a good choice for a hybrid network architecture, where also important properties like the coherence time and the spin linewidth seem to be beneficial [BSTC06, PRW<sup>+</sup>13]. The nodes of such Hybrid Quantum Networks typically operate in the microwave and radio frequency range. In order to link both, the reversible conversion of quantum information between a microwave resonator and an erbium spin ensemble is beneficial [Ima09].

In this thesis we study the coupling properties of erbium doped crystals to microwave resonators using Electron Spin Resonance (ESR) spectroscopy [Poo67], also sometimes termed as Electron Paramagnetic Resonance (EPR) [AB70]. We start with the theoretical description of the ESR spectroscopy, the crystal and resonator properties, where all the described components come together in section 3.4 about Cavity Quantum Electrodynamics. Equipped with the theoretical background, subsequent chapters show the achieved measuring results.

The main focus of this thesis lies on the measurements of different erbium doped crystals (Er:YSO), coupled to waveguide resonators. In addition, we also mention a short chapter using superconducting lumped element resonators coupled to a erbium doped crystal with a different host (Er:YAlO).



## 3. Theory

---

This chapter will furnish our knowledge about Electron Spin Resonance (ESR) of erbium doped crystals coupled to waveguide resonators, which is useful to interpret and determine the physical meaning of the results presented in later chapters. The theory starts with some basics according to ESR spectroscopy, whereas the properties of the samples, namely the erbium doped crystals, are shortly introduced afterwards. We then continue with the main measurement devices, which are the waveguide resonators and finish our theoretical discussions with a combination of some previously discussed properties and effects covered by Cavity Quantum Electrodynamics.

### 3.1. Basics of Electron Spin Resonance (ESR) Spectroscopy

Electron Paramagnetic Resonance (EPR) and Electron Spin Resonance were first discovered by Zavoisky in 1945 [Ort68]. The year of discovery coincides not just by accident with the end of World War II. During this period high research efforts have been done on the development of the radar technology [Poo67], which was also definitely pushing the microwave technology.

For example, today electronic transitions are induced by e.g. incandescent lamps or laser irradiation with frequencies lying in the optical range occupying oscillations in the THz region. Whereas, ESR studies the required energy to reorient the electronic magnetic moments via microwaves, occupying typical frequencies in the GHz region. In order to get familiar with the ESR spectroscopy, some basic principles are described in subsequent sections.

#### 3.1.1. The g-Factor and Magnetic Resonance

ESR spectroscopy measures the energy needed to induce a change in orientation of the electronic magnetic moment in atoms or molecules which contain unpaired electrons. In principal, paramagnetism is an effect of permanently existing magnetic dipoles, which is caused by the presence of a non-zero angular momentum.

The total angular momentum  $J$  and the magnetic dipole moment  $\mu$  are related by the formula

$$\mu = \gamma J, \tag{3.1}$$

where  $\gamma$  is the gyromagnetic ratio. The total angular momentum  $J$  is the sum of the particle's orbital angular momentum  $L$  and its spin  $S$  (LS-coupling). Therefore, a free

atom or ion takes values of the gyromagnetic ratio of  $\gamma = g(q/2m)$ . Equation 3.1 can also be written in terms of the gyromagnetic ratio, written as

$$\mu = g(q/2m)J. \quad (3.2)$$

For electrons the letter q (particle charge) is the electron charge (-e) and m equals the electron mass ( $m_e$ ).

The quantity  $g$  is the so called g-factor, which is a pure number of order unity, whose value depends on the relative contributions of orbit and spin to the total angular momentum [AB70]. If for example only the electron spin momentum is present (free atom or ion), the g-factor ( $g_S$ ) equals approximately<sup>1</sup> 2 and  $\gamma=q/m$ .

For J being only L, the g-factor ( $g_L$ ) equals 1. In case of LS-coupling, the more appropriate value for  $g$  is

$$g = \frac{J(J+1)(g_L + g_S) + [L(L+1) - S(S+1)](g_L - g_S)}{2J(J+1)}, \quad (3.3)$$

which is the Landé formula [AB70]. For an atom or ion, e.g. confined in a crystal structure, the g-factor differs from the Landé formula and is rather known as the spectroscopic splitting factor.

In presence of a magnetic field<sup>2</sup> B, a torque should be present. Such a torque equals  $\vec{\mu} \times \vec{B}$ , which leads to a precession of the magnetic moment and the total angular momentum about an axis parallel to the magnetic field.

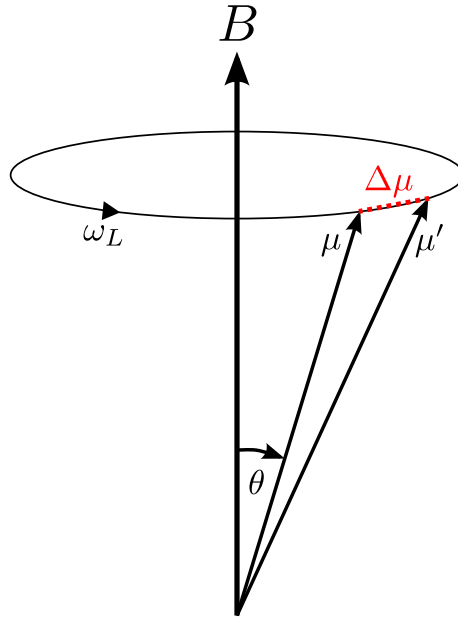


Figure 3.1.: Precession of a magnetic moment  $\mu$  around an applied magnetic field B and an angle  $\theta$  between  $\mu$  and B with Larmor frequency  $\omega_L$ .

<sup>1</sup> The more precise value is rather  $g = 2(1 + \alpha/2\pi - \dots) = 2.0023$  with  $\alpha$  being the fine-structure constant [AB70].

<sup>2</sup> Sometimes in literature the letter H is used for the magnetic field instead of B. However, both values are connected via the permeability  $\mu = H/B$ . (Please note:  $\mu$  is here not the magnetic moment!)

Figure 3.1 shows that the change of the magnetic moment  $\Delta\mu$  in a certain time interval  $\Delta t$  is given as

$$\frac{\Delta\mu}{\Delta t} = \omega_L \mu \sin(\theta). \quad (3.4)$$

The angular precession frequency  $\omega_L$  is the so called Larmor frequency. Equation 3.4 can also be written in terms of the total angular momentum  $J$  using equation 3.2. Knowing that the torque equals  $dJ/dt = \mu B \sin(\theta)$ , the Larmor frequency results in

$$\omega_L = g \frac{q}{2m} B, \quad (3.5)$$

where the ratio of  $\mu/J$  was used according to equation 3.2. In addition, the magnetic moment could also be defined in terms of energy, which is in classical terms  $E = \vec{\mu} \cdot \vec{B}$ . Also classically, there would be an infinite number of possible energy states (all of the same energy), where the word 'state' describes a particular direction of the total angular momentum vector.

On the other hand, in quantum mechanics such states are degenerate or quantized. The z-component of the total angular momentum can have only certain discrete values, indicated by the total angular momentum quantum number  $j$  with values of  $j\hbar, (j-1)\hbar, \dots, -j\hbar$  [FLS64].

If for example  $j$  equals  $1/2$ , indicating that the angular momentum quantum number  $l$  is zero and the spin quantum number  $s$  is  $1/2$ , this leads to  $2j+1$  states. Thus, two states valued with  $+1/2\hbar$  and  $-1/2\hbar$  are referenced as the total magnetic quantum number  $m_j$  [SMM05].

The result for the energy along the z axis is

$$E = \vec{\mu} \cdot \vec{B} = \mu_z B_z = g \left( \frac{q}{2m} \right) J_z B_z = g \left( \frac{q}{2m} \right) m_j \hbar B_z, \quad (3.6)$$

with  $J_z$  being  $m_j \hbar$ . Therefore the energy of the system changes linearly with the magnetic field  $B$  and a slope given by  $g(q/2m)m_j \hbar$ , as depicted in figure 3.2:

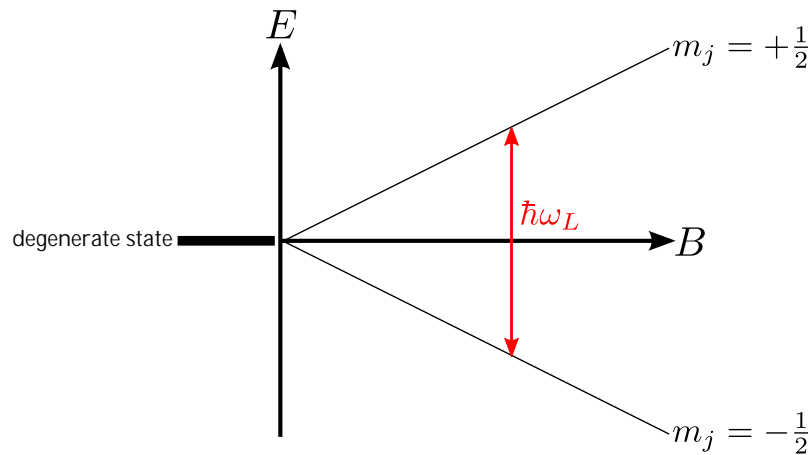


Figure 3.2.: Splitting of a degenerate state in presence of a magnetic field  $B$  due to the Zeeman effect. The energy difference between the two new states with total magnetic quantum numbers  $m_j = \pm 1/2$  is the Zeeman energy with energy quanta of  $\hbar\omega_L$ .

Equation 3.6 could be further simplified as

$$E = g\mu_B m_j B, \quad (3.7)$$

using  $\mu_B$  as the Bohr magneton and dropping the subscript  $z$ . Furthermore, the energy difference in figure 3.2, denoted by  $\hbar\omega_L$ , is the energy quantum called Zeeman energy, which is for the example of  $j=1/2$  and the selection rule  $\Delta m_j = \pm 1$ :

$$\Delta E = E_{Zee} = g\mu_B B \left( \frac{1}{2} - \left( -\frac{1}{2} \right) \right) = g\mu_B B = \hbar\omega_L. \quad (3.8)$$

The same result is also achieved by just multiplying equation 3.5 by  $\hbar$ . It is helpful to write equation 3.8 in terms of numerical values and frequency  $f$ , where we use  $9.274 \cdot 10^{-24}$  J/T for the Bohr magneton ( $\mu_B$ ) and  $6.626 \cdot 10^{-34}$  Js for the Planck constant ( $h$ ) [SMM05]. The final result is given as

$$g \approx 0.71447 \cdot 10^{-10} \cdot \frac{f}{B} \quad (3.9)$$

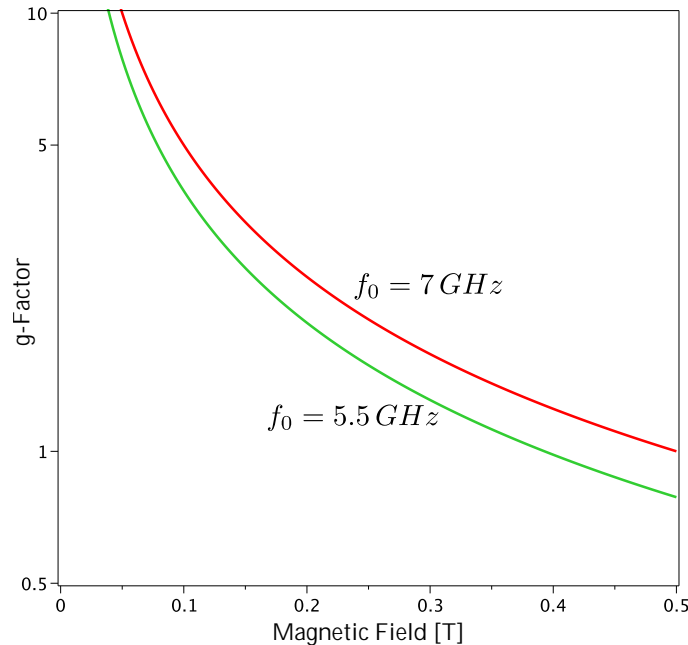


Figure 3.3.: Dependence of the spectroscopic g-factor according to the magnetic field  $B$  and two examples of resonant frequencies  $f_0$ . (Plot according to equation 3.9)

The green curve in figure 3.3 is plotted for  $f_0 = 5.5$  GHz and the red curve is plotted for  $f_0 = 7$  GHz. It is clearly seen, that with increased magnetic field  $B$  the g-factor drops nonlinearly (vertical axis in logarithmic scale). In order to measure low g-factors, either relative high magnetic fields have to be applied, or the resonance frequency has to be reduced.

As it was previously discussed, in presence of an external magnetic field, a degenerate state splits up into new states. This is classically pictured as a magnetic moment which is aligned parallel or anti-parallel to the  $B$ -field, precessing with angular frequency  $\omega_L$ . Quantum mechanically, rather we say that the system is in the upper state (if e.g.  $m_j = +1/2$ ) or in the lower or down state (if e.g.  $m_j = -1/2$ ), using here again the example of a two state

system with energy  $\hbar\omega$ . Therefore, the system has to be in one of the mentioned states due to quantization, if the system is measured (observed). Otherwise also superposition states (neither up nor down, but rather both) are possible. However, by absorbing or emitting a certain amount of energy quantum, which corresponds to the energy state difference (the Zeeman energy), transitions from one energy state to the other are possible.

This brings us to the resonance phenomenon, as only in magnetic resonance the reorientation of the magnetic moment is sufficiently possible. In order to reorientate the magnetic moment parallel to e.g. a z-axis, following considerations can be done. If taking a rotating coordinate system, which rotates with the same angular frequency  $\omega$  as the precession  $\omega_L$  about this z-axis, the vector of magnetic moment is at rest in the frame of the rotating coordinate system. This could now be assumed like there is no applied magnetic field in the z-direction, as the magnetic moment is not precessing any more. Therefore, applying now a magnetic field perpendicular to the z-axis, this results in a precession of the magnetic moment around e.g. the x-axis with a precession frequency proportional to the applied magnetic field (see equation 3.5). Thus a reorientation of the magnetic moment with respect to the z-axis is achieved.

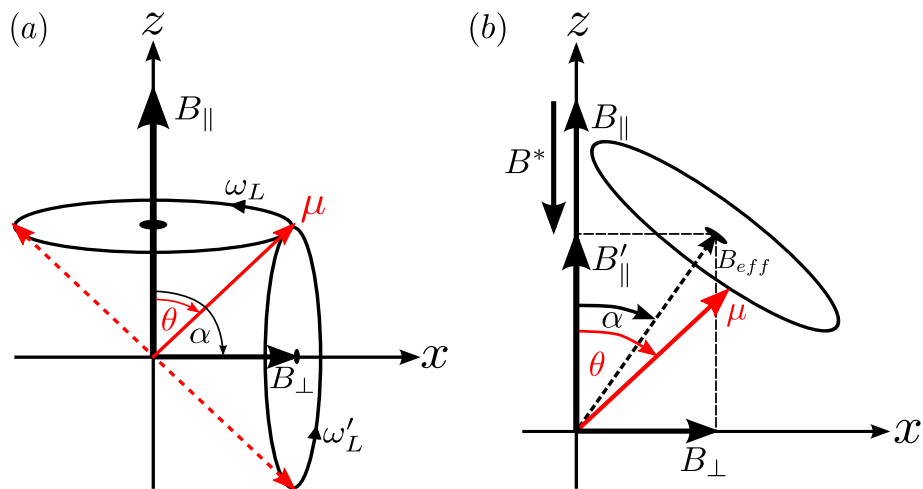


Figure 3.4.: Schematic illustration of magnetic resonance. (a) Precession of the magnetic moment  $\mu$  with frequency  $\omega_L$  around an applied, static magnetic field  $B_{||}$  with an angle  $\theta$ . If a perpendicular magnetic field  $B_{\perp}$  is applied ( $\alpha = 90^\circ$ ), in terms of a rotating frame ( $\omega = \omega_L$ ),  $\mu$  precesses around  $B_{\perp}$  with frequency  $\omega'_L$ . (b) Same situation as in part (a), except that the frame is not rotating at  $\omega_L$ . This leads to an effective magnetic field  $B_{eff}$  under an angle  $\alpha$ . Now the precession takes place around  $B_{eff}$ .

Figure 3.4 (a) depicts schematically the previously mentioned considerations. Figure 3.4 (b) in turn shows the case, where  $\omega \neq \omega_L$ . As the coordinate system is not any more rotating with the Larmor frequency  $\omega < \omega_L$ , a partial magnetic field in the direction of the z-axis is again observed ( $B'_{||}$ ). Such a field is described in terms of the applied static magnetic field  $B_{||}$  as

$$B'_{||} = \frac{1}{\gamma} (\omega_L - \omega) = B_{||} + B^*, \quad (3.10)$$

where  $B^*$  is  $-\omega/\gamma$  [AB70]. As the perpendicular magnetic field  $B_{\perp}$  is still present, the precession takes place normal to the direction of an effective magnetic field  $B_{eff}$ , spanned

by  $B_{\perp}$  and  $B'_{\parallel}$  under the angle  $\alpha$ . And from geometrical considerations it is shown, that

$$\gamma B_{eff} = \sqrt{(\gamma B_{\perp})^2 + ((\omega_L - \omega))^2} = \omega_{eff}. \quad (3.11)$$

In practice, the coordinate system is not rotating, but instead the perpendicular magnetic field  $B_{\perp}$  is used to oscillate [ $B_{\perp} = a \cos(\omega t)$ ], in order to achieve the same effect. Therefore, only the oscillation of this field has to match the magnetic resonance condition  $\omega_L = \omega$  in order to rotate the magnetic moment proportional to the magnitude of  $B_{\perp}$  with respect to the z-axis and thus to the static magnetic field  $B_{\parallel}$ . Hence, it is also possible to achieve this effect if  $B_{\perp} \ll B$ , i.e. for relatively small values of  $B_{\perp}$ , as indicated in figure 3.4 by a smaller arrow compared to  $B_{\parallel}$ . A relatively simple correspondence between the classical approach and quantum mechanics is given in the case of having  $j = 1/2$ . The wave-function for this case will generally be a linear combination of the wave-functions of the states  $|J_z\rangle = +1/2$  and  $-1/2$ , which can be written as  $|+\rangle$  and  $|-\rangle$ . A suitable combination with normalized coefficients is given by Abragam [AB70] as

$$\psi = \cos\left(\frac{1}{2}\beta\right) |+\rangle + \sin\left(\frac{1}{2}\beta\right) |-\rangle, \quad (3.12)$$

where  $\beta$  is the angle of circulation like shown in figure 3.5 below. The z-component of the magnetic moment is given as [AB70]:

$$\begin{aligned} \mu_z &= \langle \psi^* | \gamma \hbar J_z | \psi \rangle = \frac{1}{2} \gamma \hbar \left( \cos^2\left(\frac{1}{2}\beta\right) - \sin^2\left(\frac{1}{2}\beta\right) \right) \\ &= \frac{1}{2} \gamma \hbar \cos(\beta) = \mu \cos(\beta). \end{aligned} \quad (3.13)$$

The same result can also be deduced from figure 3.5:

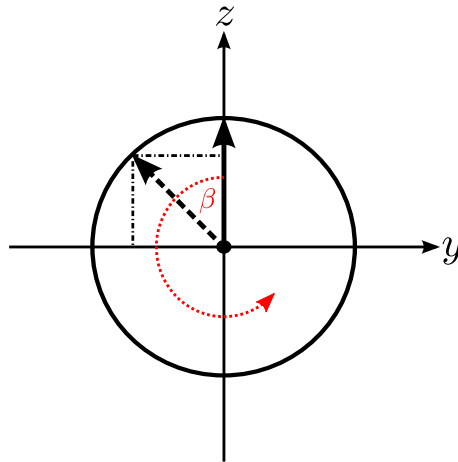


Figure 3.5.: Rotation of the magnetic moment  $\mu$  (black solid and dashed arrow) around the x-axis, which is the same direction of the applied magnetic field  $B_{\perp}$ . Obviously the component of  $\mu_z$  changes with angle  $\beta$ .

Figure 3.5 shows the case, where the coordinate system of figure 3.4 is rotated clockwise by 90 degrees around the z-axis. Now, the magnetic moment vector precesses around the x-axis, pointing out of the paper plane due to the applied magnetic field  $B_{\perp}$ . Therefore, the component of the magnetic moment with respect to the z-axis ( $\mu_z$ ) is changing with angle  $\beta$ . This indicates, that  $\mu_z = \mu \cos(\beta)$ , the same result as for equation 3.13 [AB70].

It may be noted that the exchange of energy between the oscillatory field and the magnetic moment is only effective, if the direction of the precession is synchronous with the oscillatory magnetic field, i.e. a circularly polarized field. However, a linearly polarized field can be decomposed into two circularly polarized fields with opposite senses of rotation. Thus, surely one of these circularly fields will be in the right sense of rotation with the precession [Poo67].

Up to now we know, that transitions can be induced by certain energy quanta or photons of appropriate energy equal to the Zeeman energy. Due to the environment, the transitions could also be induced thermally by photons lying in that energy region. They are typically described by  $k_B T$ , with the Boltzmann constant and the temperature in Kelvin, respectively. In statistical mechanics the probability to find a atom or ion being in one of the previously mentioned states is proportional to

$$e^{-(\Delta E)/k_B T}, \quad (3.14)$$

where we will treat not just a single atom or ion, but  $N$  atoms or ions contributing all together to a net magnetization per unit volume [FLS64]. Those atoms or ions being in the upper state we denote as  $N_{up} = \tilde{a} e^{-g\mu_B B(1/2)/k_B T}$ , and being in the lower state as  $N_{down} = \tilde{a} e^{+g\mu_B B(1/2)/k_B T}$ , where equation 3.7 was used for the state energy with  $m_j = \pm 1/2$ . The constant  $\tilde{a}$  is determined via  $N_{up} + N_{down} = N$ . The weighted average of the magnetic moment  $\langle \mu_z \rangle$  along the z-axis is given by  $[N_{up}(-m_j) + N_{down}(+m_j)] / N$ , resulting in

$$\begin{aligned} \langle \mu_z \rangle &= j \frac{e^{+g\mu_B B(1/2)/k_B T} - e^{-g\mu_B B(1/2)/k_B T}}{e^{+g\mu_B B(1/2)/k_B T} + e^{-g\mu_B B(1/2)/k_B T}} \\ &= j \tanh\left(\frac{g\mu_B B j}{k_B T}\right), \end{aligned} \quad (3.15)$$

where  $m_j$  was replaced by  $j = 1/2$ . Plotting this formula, the typical hyperbolic tangent behavior is observed as expected.

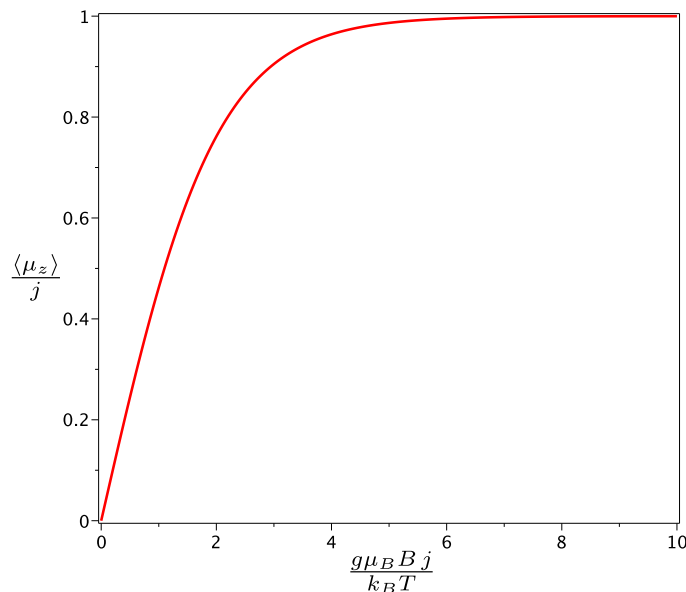


Figure 3.6.: Equation 3.15 plotted according to the argument of the hyperbolic tangent function resulting in normalized values of the z-component of the magnetic moment. In order to find the magnetic moment in a defined state, the argument has to have a relatively large value (if  $g\mu_B B j$  is  $\gg k_B T$ ). Typically such a case is achieved by low (cryogenic) temperatures  $T$ .

Applying some numbers to equation 3.15 shows, that for  $g = 1$ ,  $B = 300$  mT and  $T = 30$  K, the normalized average of 'all' atoms or ions per unit volume being in e.g. the down state is  $\approx 0.17$  %, whereas for a temperature of 30 mK it is already  $\approx 93$  %. Therefore, it is best to perform ESR spectroscopy at low temperatures.

### 3.1.2. Effective Spin and the Hyperfine Structure

Dealing with solid state host materials or crystals, like it is the case for this thesis, the contributions of such an environment onto the paramagnetic ion have to be taken into account. The unpaired electron, which is localized on its central ion, moves in such a crystal field or potential and thus experiences e.g. a 'Stark splitting' of its orbital states. In terms of a crystalline field approximation, the result is a splitting of the states, leaving groups of rather small degeneracy.

This degeneracy within each group depends on the symmetry of the complex and in case of lower symmetry, the levels may often be only single or degenerate in pairs [AB70]. An important theorem due to Kramers states, that the degeneracy of such pairs, or doublets (Kramer doublets), cannot be raised by an electric field, thus any ion with an odd number of unpaired electrons must always have a doublet as its lowest state [Ort68].

In turn, by the application of a magnetic field and due to the Zeeman effect, ESR is possible. For an even number of electrons, Kramers theorem no longer applies and the degeneracy may be completely raised by a crystal field of low symmetry so that singlet levels remain, may separated by energies too large for ESR spectroscopy [Ort68].

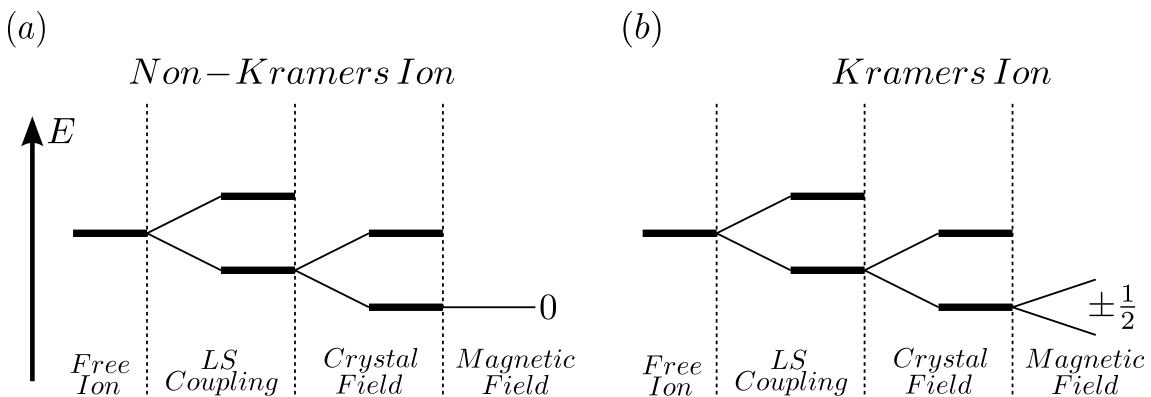


Figure 3.7.: Energy level scheme. (a) Ions possessing an even number of unpaired electrons are called Non-Kramers ions, where a magnetic field has no influence on the degenerate states, originating from a weak crystal field. (b) Ions possessing an odd number of unpaired electrons are called Kramers ions. An applied magnetic field splits the degenerate state caused by a weak crystal field.

Figure 3.7 displays schematically the behavior of the energy levels for an ion in terms of a weak crystal field. Figure 3.7 (a) displays the case for a non Kramers ion with a even number of unpaired electrons, whereas (b) depicts the case for a Kramers ion with a odd number of unpaired electrons. In order to describe such group of energy states in an easy way, an effective spin  $S'$  is typically used [Ort68, AB70].

This enables us now to write an electronic Zeeman interaction Hamiltonian as

$$\mathcal{H}_{Zee} = g\mu_B \left( \vec{B} \cdot \vec{S}' \right). \quad (3.16)$$

For example, with  $s' = 1/2$  as the effective spin quantum number,  $(2s'+1)$  states with the effective spin magnetic quantum number  $m_{s'} = \pm 1/2$  are present in a magnetic field. Thus the energy is similar to equation 3.7, just replacing the magnetic quantum number with the effective one.

These energy levels could then be treated as a two level system at cryogenic temperatures, where only the lowest doublet is populated.

In analogy to the beforehand mentioned unpaired electrons which possess a magnetic moment, equal considerations could be adopted for the nucleus with a total nuclear angular momentum  $I$ . Thus, the nucleus with an odd number of protons and neutrons, i.e. with unpaired nucleons, will show behaviors of a magnetic moment.

If now the nucleus of a paramagnetic ion has such properties, its magnetic moment will interact with the magnetic moment of the electron, both resulting in the so called hyperfine structure. The energy needed to observe such structure is given by Abragam [AB70] to be  $\approx 10^{-1} \text{ cm}^{-1}$ , which is termed as the magnetic hyperfine interaction in the 'spectroscopic' energy notation<sup>3</sup>.

In order to have some order of magnitudes to compare, the energy involved for ESR interaction is typically  $\approx 1 \text{ cm}^{-1}$  or less and that for spin-orbit coupling amounts to be  $\approx 10^2\text{-}10^3 \text{ cm}^{-1}$  [Ort68]. Such interaction of the total electronic angular momentum  $J$  and the total nuclear angular momentum  $I$  is described for a free atom or ion by the Hamiltonian

$$\mathcal{H}_{free} = \bar{a} \left( \vec{J} \cdot \vec{I} \right), \quad (3.17)$$

and in a solid by

$$\mathcal{H}_{solid} = \bar{A} \left( \vec{S}' \cdot \vec{I} \right). \quad (3.18)$$

The coefficients  $\bar{a}$  and  $\bar{A}$  are the magnetic hyperfine constants [AB70] and are rather determined by experiment [Ort68].

In case of a free atom or ion a set of levels with quantum numbers  $F = (J+I), (J+I-1), \dots, |J-I|$  are formed, where in terms of an effective spin  $S'$ ,  $J$  is replaced.

<sup>3</sup> Wave-number notation ( $\text{cm}^{-1}$ ), in terms of the reciprocal wavelength  $\lambda$ .

The energy in terms of electron volts is given by  $E = hc/\lambda e$ , with  $h$  = Planck's constant,  $c$  the speed of light in vacuum and  $e$  the electron charge. Hence  $1 \text{ cm}^{-1} \approx 0.124 \text{ meV} \approx 30 \text{ GHz}$

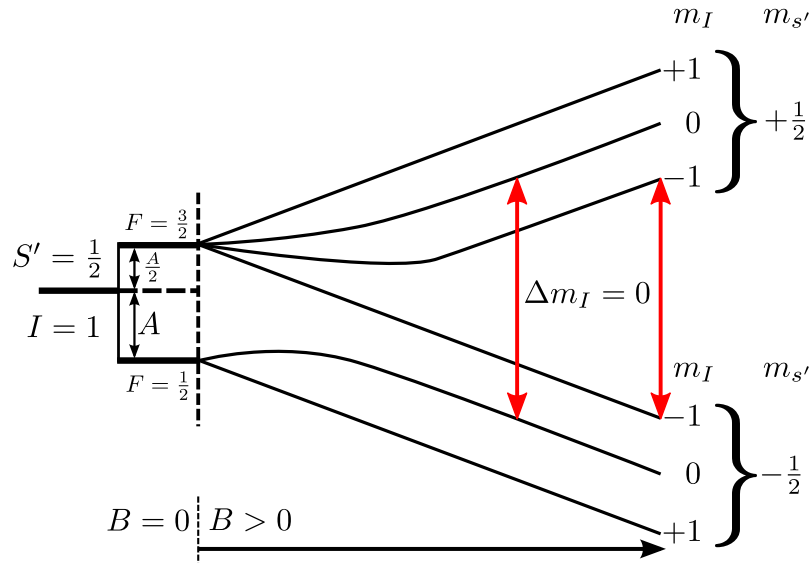


Figure 3.8.: Hyperfine splitting of an odd valued isotope at externally applied magnetic fields. Due to the interaction of the magnetic moment of an unpaired electron with effective spin  $S'$  and a magnetic moment of the nuclei with quantum number  $I$ , the degenerate state splits with quantum numbers  $F$ . Such a state again split in presence of a magnetic field  $B$ . According to the selection rules, equidistant hyperfine transitions are observed for magnetic fields  $B \gg 0$ , whereas non-equidistant transitions are more likely at regions with fields  $B > 0$ . (see also [AB70])

Figure 3.8 depicts schematically the energy levels for  $S' = 1/2$  and  $I = 1$  having a Hamiltonian of  $\mathcal{H}_{Zee} + \mathcal{H}_{solid}$ , where  $A = \bar{A}$ .

In the zero B-field region a set of levels with  $F=3/2$  (quadruplet) and  $F=1/2$  (doublet) are present according to  $2F+1$ . In the high magnetic field region ( $B \gg 0$ ) the levels diverge linearly with the B-field for constant frequency.

The level separation for the magnetic quantum numbers  $m_{S'}$  (electronic) and  $m_I$  (nuclear) is in this region equidistant. Therefore, equidistant transitions should be observed according to  $\Delta m_{S'} = \pm 1$  and  $\Delta m_I = 0$ .

Getting in the non-linear regime for fields equal to  $B > 0$ , the observed transitions are not equidistant and the situation becomes more complicated to describe. Discussions according such a regime are rather taken from Abragam [AB70].

Furthermore, it is important to mention, that transitions are best observed at cryogenic temperatures due to the population of the states. Using the magnetic hyperfine interaction with  $\approx 10^{-1} \text{ cm}^{-1}$ , this would correspond to  $\approx 150 \text{ mK}$  ( $E = hc/\lambda = k_B T$ ).

### 3.1.3. The g-Tensor and Anisotropy Effects

In the previous sections the g-factor was assumed to be equal in all directions, i.e. that  $g_x = g_y = g_z = g$ .

The same case is present if dealing with a cubic crystal field. In case of crystal environments which create different kinds of fields, the situation changes and the g-factor takes the form of a tensor, where equation 3.16 is rewritten to

$$\mathcal{H}_{Zee} = \mu_B \left( \vec{B} \cdot \hat{g} \cdot \vec{S}' \right), \quad (3.19)$$

with  $\hat{g}$  as the g-factor tensor representing

$$\hat{g} = \begin{pmatrix} g_{xx} & g_{xy} & g_{xz} \\ g_{yx} & g_{yy} & g_{yz} \\ g_{zx} & g_{zy} & g_{zz} \end{pmatrix}. \quad (3.20)$$

The same is true for equation 3.18 and the magnetic hyperfine constant  $\bar{A}$ , which changes to the magnetic hyperfine tensor  $\hat{A}$ .

Usually the g-tensor is diagonalized, yielding just the principal values of the tensor for a suitable choice of axes (principal axes). Thus, equation 3.19 can be written as  $\mathcal{H}_{Zee} = \mu_B \{g_{xx}B_xS'_x + g_{yy}B_yS'_y + g_{zz}B_zS'_z\}$ , where  $g_{xx}$ ,  $g_{yy}$  and  $g_{zz}$  can be further simplified in notation just as  $g_x$ ,  $g_y$  and  $g_z$ .

With the direction cosines  $l$ ,  $m$  and  $n$  the g-factor is given as:

$$g^2 = l^2 g_x^2 + m^2 g_y^2 + n^2 g_z^2. \quad (3.21)$$

When the crystal field is axial ( $x = y \neq z$ ), i.e. showing tetragonal or trigonal behavior, the g-factor also shows axial symmetry ( $g_x = g_y \neq g_z$ ).

In order to demonstrate how the g-factor depends on the magnetic field orientation, the case where a magnetic field  $B$  lies in the xz-plane with  $\theta$  as the angle from the z-axis is considered. If changing furthermore to a set of rotated axes ( $x'$  and  $z'$ ) about the y-axis by an angle  $\phi$ , the following transformations and definitions are required [AB70]

$$\begin{aligned} S'_x &= S'_{z'} \sin(\phi) + S'_{x'} \cos(\phi) \\ S'_y &= S'_{y'} \\ S'_z &= S'_{z'} \cos(\phi) - S'_{x'} \sin(\phi) \\ g^2 &= g_x^2 \sin^2(\theta) + g_z^2 \cos^2(\theta) \\ \sin(\phi) &= \frac{g_x}{g} \sin(\theta) \\ \cos(\phi) &= \frac{g_z}{g} \cos(\theta). \end{aligned} \quad (3.22)$$

In addition, an oscillating magnetic field  $B \sim \cos(\omega t)$  is applied with the y-axis having an angle  $\eta$  and an angle  $\theta \sim$  as its projections on the xz-plane with the z-axis. The situation is depicted in figure 3.9 on the next page for more clarity.

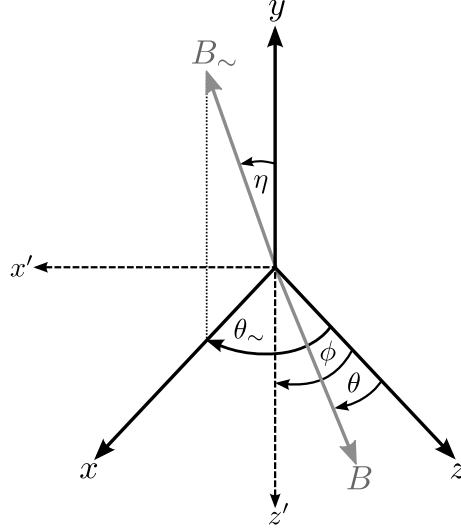


Figure 3.9.: Applied static magnetic field in the  $xz$ -plane with angle  $\theta$  from the  $z$ -axis. Rotated axes  $x'$  and  $z'$  with offset  $\phi$  according to the  $z$ -axis. An additional oscillating magnetic field  $B_{\sim}$  is applied to the  $y$ -axis, possessing an angle  $\eta$  with respect to the  $y$ -axis. The projection of  $B_{\sim}$  is determined by the angle  $\theta_{\sim}$  with respect to the axis  $z$ .

The components of  $B_{\sim}$  are  $B_{x_{\sim}} = B_{\sim} \sin(\eta) \sin(\theta_{\sim})$ ,  $B_{y_{\sim}} = B_{\sim} \cos(\eta)$  and  $B_{z_{\sim}} = B_{\sim} \sin(\eta) \cos(\theta_{\sim})$ . The definition of the Hamiltonian for the oscillatory magnetic field is  $\mathcal{H}_{\sim} = \mu_B B_{\sim} \cos(\omega t) \{g_x S'_x l_{\sim} + g_y S'_y m_{\sim} + g_z S'_z n_{\sim}\}$  [AB70]. For  $l_{\sim}$ ,  $m_{\sim}$  and  $n_{\sim}$  the angular functions of the previously mentioned components  $B_{x_{\sim}}$ , etc. are used for the direction cosines. Finally this results in

$$\mathcal{H}_{\sim} = \mu_B B_{\sim} \cos(\omega t) \left[ \begin{array}{c} S'_{x'} \frac{g_x g_z}{g} \sin(\eta) \sin(\theta_{\sim} - \theta) + \\ S'_{y'} g_y \cos(\eta) + \\ S'_{z'} ([g_x^2 \sin(\theta) \sin(\theta_{\sim}) + g_z^2 \cos(\theta) \cos(\theta_{\sim})] / g) \sin(\eta) \end{array} \right], \quad (3.23)$$

where for  $S'_{x'}$ , the term was simplified by  $\sin(\theta_{\sim} - \theta) = \sin(\theta_{\sim}) \cos(\theta) - \cos(\theta_{\sim}) \sin(\theta)$ . Now, the  $g$ -factor for the direction of the magnetic oscillating field  $g_{\sim}$  is found to be

$$g_{\sim}^2 = \left( \frac{g_x g_z}{g} \right)^2 \sin^2(\eta) \sin^2(\theta_{\sim} - \theta) + g_y^2 \cos^2(\eta), \quad (3.24)$$

where the last term of equation 3.23 for  $S'_{z'}$ , was dropped, as for this case  $B_{\sim}$  is parallel to the static magnetic field  $B$  and from the discussion in section 3.1.1, no transitions would be observed. But this does not mean, that the value for  $g_{\sim}$  is zero. However, from equation 3.24 it is clear, that  $g_{\sim}$  has highest values if  $B_{\sim}$  is perpendicular to  $B$ .

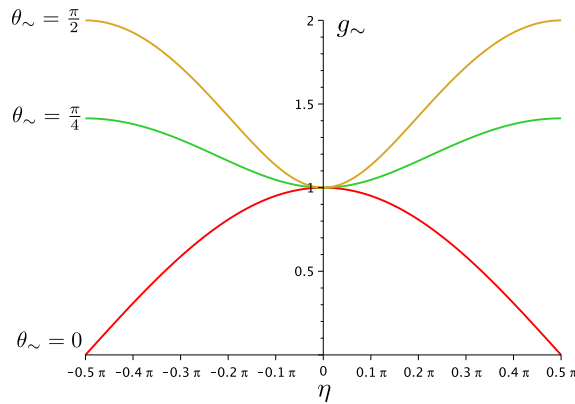


Figure 3.10.: Dependence of  $g_{\sim}$  according to the angles  $\eta$  and  $\theta_{\sim}$ . In case of axial symmetry with  $g_{\perp} = 1$  and  $g_{\parallel} = 2$ , largest values of  $g_{\sim}$  are achieved when  $\eta = 90^\circ$ , i.e. when  $B_{\sim}$  lies in the  $xz$ -plane (see figure 3.9). Only if  $\theta_{\sim} = 0$  (if  $B_{\sim} \parallel B$ ),  $g_{\sim}$  vanishes (red curve), whereas for values of  $\theta_{\sim} > 0$  to  $90^\circ$ ,  $g_{\sim}$  increases (green and yellow curve). For  $\theta_{\sim} = 90^\circ$  and  $\eta = 90^\circ$  the case  $B_{\sim} \perp B$  is given ( $xz$ -plane), reaching highest values of  $g_{\sim}$ .

Figure 3.10 illustrates the case for axial symmetry, typically written  $g_x = g_y = g_{\perp}$  and  $g_z = g_{\parallel}$ , where  $g_{\perp} = 1$  and  $g_{\parallel} = 2$  was chosen. The plot depicts that highest values are achieved for  $\eta = \pi/2$  (or  $\eta = 0.5\pi$ ). For  $\theta_{\sim} = 0$  (red curve in figure 3.10), being the case  $B_{\sim} \parallel B$ , the value for this example is zero, but increases for  $\theta_{\sim} \rightarrow \pi/2$  (green and yellow curve of figure 3.10).

### 3.1.4. Inhomogeneous Broadening and Spin-Spin Interaction

Further anisotropy effects are associated with the interaction between neighboring paramagnetic ions (magnetic dipole interaction), called spin-spin interaction. This arises generally if the magnetic ions have anisotropic g-factors, i.e. a g-tensor. The distance of interaction or influence is roughly  $\mu/r^3$  between the ions, being  $\approx 0.3$  to  $0.8$  nm [AB70]. This anisotropy effect leads to an inhomogeneous broadening of the spectrum.

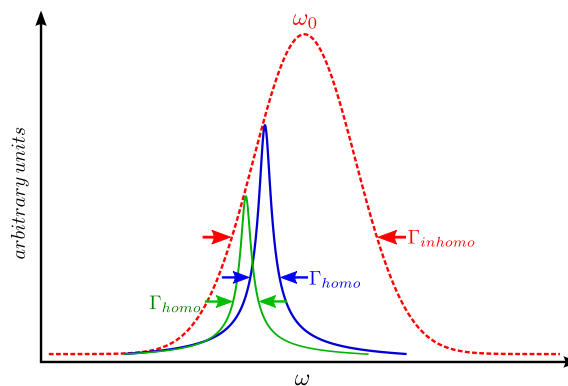


Figure 3.11.: Due to various effects like spin-spin interactions in anisotropic media the spectra are typically inhomogeneously broadened (red, dashed curve).  $\Gamma_{inhomo}$  schematically describes such effects, being the spin linewidth at full width, half maximum. The inhomogeneous broadening results out of several homogeneously broadened Lorentz curves (green and blue curves), originating from e.g. individual groups of ions, distributed around the main resonance angular frequency  $\omega_0$ . Typical values for  $\Gamma_{homo}$  are found in the Hz range (e.g. 50 Hz), whereas  $\Gamma_{inhomo}$  features values of some tens of MHz [PRW<sup>+</sup>13], up to several GHz [TAC<sup>+</sup>10].

Assuming, there would not be an interaction of the magnetic dipole moments of the paramagnetic ions between themselves and neglecting other broadening effects up to now, on applying an external magnetic field all these moments would precess with the same frequency. At resonance only one absorption peak at the resonance frequency should be observed as indicated in figure 3.11 via a green or blue Lorentz curve with  $\Gamma_{\text{homo}}$  as the homogeneous broadening at full width and half maximum (FWHM).

Theoretically this should just be a delta peak in the spectrum, which is not true in reality, as the absorption and emission of an energy quanta is related via<sup>4</sup>  $\Delta E \Delta t \approx \hbar$  (Heisenberg uncertainty relation). As  $1/\Delta t \approx \Delta \nu$ , every energy difference is related with a frequency difference  $\Delta \nu$  or bandwidth. Furthermore, such transitions have an exponential behavior in the time domain, which transforms to a Lorentzian shape function in the frequency domain, like described in section 3.1.1.

If every paramagnetic ion absorbs or re-emits an energy difference at just one distinct frequency with a certain bandwidth, this leads to a single Lorentz peak. If there is now the spin-spin interaction, this could be assumed like a distortion of the mean precession frequency to slightly other precession frequencies or shifts. Thus, depending on the positions of the paramagnetic ions in a crystal material, also the influence of the neighboring ion varies and the precession of the ion is slightly changed.

Such different frequencies are displaced from the mean frequency value, where the intensity or amplitude of the absorption changes from the center. This causes a broadening of the spectrum and thus a different shape function results, indicated by the envelope in figure 3.11.

An inhomogeneous external magnetic field would lead to the same effect. For a homogenous external magnetic field and no spin-spin interaction the term 'homogenous broadening' is used.

The frequency bandwidth due to inhomogeneous broadening is a representation of the average duration of the 'wave train' emitted or absorbed by the spin system, which is a combination of the spin-spin interaction and the relaxation time,  $\tau_1$ . M. Fox is declaring in his book [Fox06]  $\tau_2$  ( $T_2$ ) as the total dephasing rate, written

$$\frac{1}{\tau_2} = \frac{1}{2\tau_1} + \frac{1}{\tau_{2*}}, \quad (3.25)$$

where here the greek letter notation is used. Usually,  $\tau_{2*}$  is the so called pure dephasing, e.g. due to spin-spin interaction. Therefore, if  $\tau_1 \gg \tau_{2*}$ , equation 3.25 just reduces to  $\tau_{2*} = \tau_2$ . On the other hand, if  $\tau_{2*} \gg \tau_1$ ,  $2\tau_1$  equals just  $\tau_2$  [Fox06].

Typically,  $\tau_1$  is associated with the spin-lattice relaxation time or the longitudinal relaxation time, which describes the interaction of a populated or excited upper energy level with the crystal lattice. The terms, transverse or longitudinal are chosen in analogy to the cartesian coordinate system with the vertical z-axis (longitudinal) and the perpendicular xy-plane (transverse).

As the Zeeman energy introduced in section 3.1.1 is typically determined along the z-axis, the local magnetic moments of the individual paramagnetic ions are not pointing necessary into the same direction as the external applied magnetic field. The net effect onto the z component will be therefore relatively constant if the applied magnetic field is large compared to the local ones. But this is not necessarily true for the transverse components x and y.

---

<sup>4</sup>  $\Delta E$  = energy difference,  $\Delta t$  = time difference,  $\hbar = h/2\pi$  = reduced Planck's constant

Such considerations have also been assumed by Bloch (1946) [AB70]. The easiest way to describe such dephasing effects is therefore the use of the Bloch representation.

The vector sum of individual magnetic moments pointing parallel to the applied magnetic field are typically defined as the energetically lowest state. In the Bloch representation an arrow or several arrows (the Bloch vectors) would point into the negative z-direction of the Bloch sphere. An energetically higher state is reached when the moment points anti-parallel to the magnetic field, indicated by a vector or vectors pointing into the positive z-direction.

If now the negative z-direction is defined as the 0 state, the positive z-direction is defined as state 1. Flipping the vectors from minus z to plus z by a rotation of  $\pi$  will lead to an increase of the z-component. If now recalling section 3.1.1, the precession of the magnetic moment about a magnetic field could be indicated by a rotation of the vectors in the Bloch sphere.

For example, if the vectors would lie in the horizontal plane, they would rotate with the total precession frequency around the origin of the sphere. Rotations of the vectors from state 0 to state 1 by  $\pi$  would then result in a helical movement. In the picture of an rotating frame the vectors will stay at rest. Furthermore, the tips of the vectors will just follow now a straight line on the surface of the sphere.

The sens of rotation (clockwise or counter-clockwise) depends on the polarization of the oscillating magnetic field, as discussed in section 3.1.1.

In case of the times  $\tau_1$  and  $\tau_2^*$ ,  $\tau_1$  would be the time where the vectors in the Bloch sphere flip back to its initial state (here 0). Thus, the z-component changes in a certain time interval proportional to a energy change.

The physical explanation of this 'back-flip' or relaxation will be given after the Bloch sphere discussion in more detail.

In order to determine  $\tau_2^*$ , the vectors have to be flipped to the horizontal or transverse plane (xy-plane), where the individual Bloch vectors do not necessarily precess at the main frequency. Therefore, they would start slowly to rotate in that plane or to fan out. This leads now to a noticeable change of the x and y-components. This fanning out is now the previously mentioned pure dephasing effect, indicating that the individual magnetic moments are not oscillating in phase (e.g. due to inhomogeneous broadening). By rotating again the vectors by  $\pi$  around the xy-plane, the fanning out process is now reversed. This will lead to a restoration of the phase relation between the individual vectors and thus to an emission of a photon (or photons) due to coherent oscillations in phase.

This rephasing time can be used in the so called spin-echo experiments to determine  $\tau_2^*$ . When measuring  $\tau_1$ , there is always a contribution of  $\tau_2^*$ , as the vectors have always to pass the xy-plane (equation 3.25). Such rotations of  $\pi$  or  $\pi/2$  are realized in experiments by applying appropriate electromagnetic pulses (i.e. the pulse area [Fox06]) at appropriate resonance frequencies. The recent discussion is depicted in figure 3.12 on the next page.

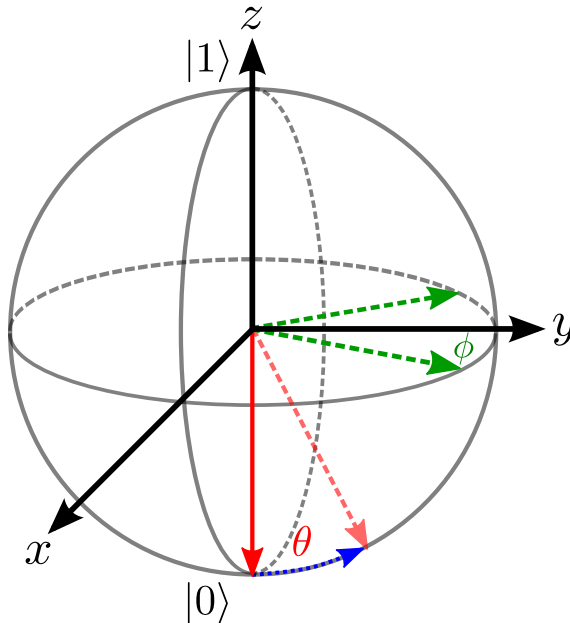


Figure 3.12.: The Bloch sphere representation, where typically the z-axis is defined as state 0 (-z) and state 1 (+z). The Bloch vector (e.g. the magnetic moment) is pointing in one of these directions for a certain situation. The vector is rotated (blue, dotted arrow) around the sphere center by an angle  $\theta$ , which e.g. represents a transition given in a two level system of certain energy. Rotations of  $\theta$  are indicated by  $\tau_1$ , where rotations of  $\phi$  (green, dotted arrow) are typically denoted as  $\tau_2^*$ . The green, dashed arrows represent a fanning out or dephasing of the individual vectors in the xy-plane, which are then out of phase with respect to each other.

### 3.1.5. Spin-Lattice Interactions

In order to understand the spin lattice interaction, some considerations regarding the lifetime of an energy state or level will be treated first.

Via absorption of e.g. a photon of a certain energy quantum  $\hbar\omega$  a lower energetically state is 'lifted' into a higher one. Usually, such a system tends to recover back to its initial lower energy state via a spontaneous or stimulated emission of e.g. a photon, or even non-radiatively.

However, such transitions are usually described by the Einstein coefficients  $A$  for spontaneous emission and  $B$  for stimulated emission or absorption, where the transition rates are given as follows [Eic13]:

$$\begin{aligned}
 \left(\frac{dN_2}{dt}\right)_{\text{absor}} &= -\left(\frac{dN_1}{dt}\right)_{\text{absor}} = +BuN_1 \\
 \left(\frac{dN_2}{dt}\right)_{\text{stimu}} &= -\left(\frac{dN_1}{dt}\right)_{\text{stimu}} = -BuN_2 \\
 \left(\frac{dN_2}{dt}\right)_{\text{spont}} &= -\left(\frac{dN_1}{dt}\right)_{\text{spont}} = -AN_2 .
 \end{aligned} \tag{3.26}$$

$N_1$  is the number of absorbers,  $N_2$  is the number of emitters and  $u$  is the electromagnetic (EM) radiation density. This equations already assume that stimulated emission or

absorption ( $B$ ) is 'triggered' by the EM-field, whereas the spontaneous emission<sup>5</sup> ( $A$ ) is not.

From the last row of equation 3.26 it is deducible that  $N_2$  has an negative exponential time behavior with  $-t/\tau$  as argument. This behavior leads to an Lorentzian shape in the Fourier domain.

In thermal equilibrium the populations of both levels or states is constant and their ratio can be described by a Boltzmann distribution as  $N_2/N_1 = B\mathbf{u}/(A + B\mathbf{u}) = \exp(-\hbar\omega/k_B T)$  [Eic13]. Using this relation and knowing that  $\tau = (A + 2B\mathbf{u})^{-1}$ , following equation is observed

$$\frac{1}{\tau} = \frac{\hbar\omega^3}{\pi^2 c^3} B \coth\left(\frac{\hbar\omega}{2k_B T}\right) = A \coth\left(\frac{\hbar\omega}{2k_B T}\right), \quad (3.27)$$

where  $\mathbf{u}$  was used as  $(\hbar\omega^3/\pi^2 c^3)(1/(\exp(\hbar\omega/k_B T) - 1))$  [AB70].

A quick analysis of equation 3.27 already shows that  $\tau = B/A = \pi^2 c^2/\hbar\omega^3$ . This indicates that for higher frequencies coefficient  $A$  is dominating<sup>6</sup>. Thus, the lifetime of a upper state is primarily depopulated via spontaneous emission.

Under considerations that  $\hbar\omega \gg k_B T$  in the hyperbolic cosine term,  $\tau$  becomes independent of temperature. For such a case  $\tau$  is again entirely determined by  $A$ , where for frequencies typically used in ESR spectroscopy spontaneous emission could be neglected [Poo67]. On the other hand, for  $\hbar\omega \ll k_B T$ ,  $\tau$  depends also on temperature. Such interactions are typically called thermal electromagnetic radiation field density interactions.

If using  $B = (2\pi^2/3)\gamma^2$  [AB70] according to  $J = 1/2$  and  $g = 2$ , for a frequency of 5 GHz and a temperature of 1 K a result of  $\tau \approx 2 \cdot 10^6$  seconds is found.

In experiments, such values are of course not observed, as we are typically not dealing with just single spins.

Furthermore, we are also faced with a solid state surrounding, where interactions are rather induced by lattice vibrations, i.e. mechanical motions which create oscillatory electromagnetic fields. In analogy to the thermal electromagnetic radiation field density, such lattice vibrations could be associated with a phonon radiation field density.

Previously, the radiation density  $\mathbf{u}$  was used for photons, with  $c^3$  in the denominator as the speed of light. Now, the radiation density is rewritten in case of lattice vibrations, i.e. replacing  $c^3$  by  $v^3$ , where  $v$  is the velocity of sound.

The phonon radiation field density is:

$$\mathcal{U} d\omega = \frac{3\hbar\omega^3}{2\pi^2 v^3} \frac{d\omega}{\exp(\hbar\omega/k_B T) - 1}, \quad (3.28)$$

where the prefactor of 3/2 results out of the possible phonon-modes [AB70]. In order to describe now the spin-lattice relaxation time  $\tau_1$ , there are typically three processes involved. They are the direct process, the two-phonon Raman process and the two-phonon Orbach process.

<sup>5</sup> Quantization of the EM-field (quantum electrodynamics) provides a solution termed vacuum fluctuations. Such fluctuations are expected today to act as the 'trigger' for spontaneous emission

<sup>6</sup> This is also one of the reasons why it is quite difficult to build e.g. x-ray or gamma lasers. The lifetime of such upper states is too short to be 'triggered' via stimulated emission.

Then,  $\tau_1$  is given as

$$\frac{1}{\tau_1} = \mathcal{A} \coth\left(\frac{\hbar\omega}{2k_B T}\right) + \mathcal{B}T^n + \frac{\mathcal{C}}{\exp(\Delta/k_B T) - 1}, \quad (3.29)$$

using  $n = 7$  for a non-Kramers doublet,  $n = 9$  for Kramer doublet and  $\Delta$  being the energy difference between a two level system and a third energy level in the Orbach process [AB70]. The Orbach process is a kind of direct process, where a phonon of energy  $\hbar\omega_1$  is absorbed from the first excited state of a two level system to a higher one. Emission from this state to the ground state happens with energy  $\hbar\omega_2$ . The direct process would mean, that a phonon of energy difference  $\hbar\omega$  is absorbed and emitted according to the energy difference of the two level system. The Raman process is similar to the Orbach process, just with the difference that no direct processes are involved, but implies virtual states or energy levels.

However, from equation 3.29 it is clear, that contributions to the spin-lattice relaxation time due to Raman ( $\mathcal{B}$ ) or Orbach ( $\mathcal{C}$ ) processes depend mainly on the temperature  $T$ . Therefore, if the temperature is rather low (e.g.  $< 1$  K), both mentioned terms are rather neglected.

Finally,  $\mathcal{A}$  is determined to be just  $B\mathcal{U}\{\exp(\hbar\omega/k_B T) - 1\}$ , where  $B$  has to be determined in order to calculate  $\tau_1$ . One approach to do so, is for example to evaluate the transition probability  $W$ :

$$W_{fi} = \frac{2\pi}{\hbar^2} \epsilon^2 \left| \langle i | \mathcal{V}^{(1)} | f \rangle \right|^2 f(\omega). \quad (3.30)$$

The complete Hamiltonian would be  $\mathcal{H} = \mathcal{H}_{Zee} + \mathcal{V}$ , with  $\mathcal{V} = V^{(0)} + \epsilon V^{(1)} + \epsilon^2 V^{(2)} + \dots$  as the crystalline electric potential in powers of the strain [AB70]. We assume that the transition  $W_{fi}$  is caused mainly by the lattice vibrations described by  $\epsilon V^{(1)}$  (neglecting higher terms), where  $V^{(0)}$  represents the static potential term.  $\mathcal{H}_{Zee}$  and the static potential should not have an strong influence and are thus not mentioned in equation 3.30. Furthermore, the strain could be considered as  $2\rho v^2 \epsilon^2 = \mathcal{U}d\omega$ , with  $\rho$  as the crystal density [AB70]. The line shape function  $f(w)$  integrated over  $d\omega$  is usually taken to be 1. The transition probability of stimulated emission is  $W = B\mathcal{U}$  (neglecting spontaneous emission), where  $B$  is determined as  $\approx (\pi/\hbar^2 \rho v^2) \cdot |V^{(1)}|^2$  [AB70]. Hence, in case of a Kramers doublet,  $V^{(1)}$  is further approximated by  $(\hbar\omega/\Delta_c)V^{(1)}$ , with  $\Delta_c$  as the crystal field splitting [AB70]. The final equation is given as:

$$\tau_1 \approx \left(\frac{2\pi}{3\hbar}\right) \left(\frac{\Delta_c^2 \rho v^5}{|V^{(1)}|^2}\right) \left(\frac{1}{\omega^5 \coth(\hbar\omega/2k_B T)}\right). \quad (3.31)$$

The second part in brackets of the right hand side of equation 3.31 are the parameters given by the crystal, where the first part are just constants. The last bracket is indicating the influences from outside as the angular frequency  $\omega$  and temperature  $T$ . If a Kramers doublet is present,  $\tau_1$  is enhanced by e.g. the crystal field splitting  $\Delta_c^2$ . Moreover,  $\tau_1$  is further enhanced by factors like  $v$  and  $\rho$ , which could be explained physically by lower lattice vibrations for higher sound velocities. In such a case the lattice is following rather less the motions of a driving force due to the inertia of e.g. bigger ion masses ( $\rho = \text{mass}/\text{vol.}$ ). Usually  $v$  and  $\rho$  are connected with each other, meaning that the velocity of sound depends also on the density  $\rho$ . However, by increasing the density also other effects like spin-spin interactions are of course enhanced, which is maybe impeded by dilution of the paramagnetic ion in the host material.

There are several ways to measure  $\tau_1$ , e.g. by the techniques of spin-echo, line broadening or continuous saturation. However, the most widely used and very effective method is that of the pulse saturation recovery. The transition under investigation is saturated by a pulse of microwave power at the resonance frequency, where the subsequent return to equilibrium is observed by monitoring the population difference with a lower power source close to the main frequency [Ort68]. It is sufficient to fit standard exponential curves to the measured signal in order to determine  $\tau_1$ .

## 3.2. Erbium ( $\text{Er}^{3+}$ ) Doped Crystals

Rare-earth (RE) metals doped or implanted into inorganic solid state hosts or crystals have been studied for more than half a century. Particularly due to interest for solid state lasers, fiber optics amplifiers, laser stabilization for programmable frequency standards and radio frequency analyzers. Usual investigations are focused on thulium, europium, neodymium and erbium, typically in  $\text{Y}_2\text{SiO}_5$  or  $\text{LiNbO}_3$  [TAC<sup>+</sup>10].

In this thesis the main focus of interest lies on erbium doped crystals, where  $\text{Y}_2\text{SiO}_5$  (YSO) is used as host material.

Already today much spectroscopic investigation was done on temperatures typically at 6-10 K for erbium doped YSO hosts [GNBG<sup>+</sup>06], [SBTC08]. Our interest lies more on the ability to study such doped crystals for hybrid quantum system (HQS) applications.

Furthermore, also a second host material  $\text{YAlO}_3$  (YAlO) is used, where rather few investigations have been done by the scientific world on low temperatures ESR spectroscopy. This sections are going to give just a short introduction on the REs, especially erbium and its environment, the host materials YSO and YAlO.

### 3.2.1. The Lanthanide (4f) Group and Erbium ( $\text{Er}^{3+}$ )

The lanthanide group or the rare earths have the significant feature of filling the  $4f^n$  shell successively by  $n$  ( $n \geq 0$  &  $n \leq 14$ ) unpaired electrons in case of a tripositive ion, where the filling of the  $4f$  shell is different for dipositive and quadripesitive ions or natural atoms.

In case of Lanthanum, for example, the electron is rather occupying the  $5d$  shell instead of  $4f$ . The closed or completely filled orbitals correspond to the Xenon core, where the closed shells  $5s^25p^6$  shield the  $4f$  electrons from its environment. Furthermore, such unpaired electrons are of course necessary for ESR or any kind of spin experiments.

For the sake of clarity, all tripositive lanthanide ions with its atomic number  $Z$ , the  $4f^n$  configuration, the ground state, its number of the odd isotopes and the corresponding nuclear spin  $I$  are summarized in table 3.1 on the next page.

Focusing now in more detail onto the tripositive ion of erbium ( $\text{Er}^{3+}$ ), table 3.1 shows that erbium has eleven electrons in the  $4f$  shell, which we can treat as a Kramers ion.

Furthermore, the ground state  $^{2S+1}L_J$  has the values  $^4I_{15/2}$ , leading to  $L = 6$  and  $S = 3/2$ .

As mentioned before, dealing with a Kramers ion, the degeneracy is split due to a crystal field in  $J = 15/2 + 1/2 = 8$  doublets, where for the lowest doublet an effective spin  $S' = 1/2$  at low temperatures can be assumed.

$Z$	Name	Symbol	4f Config.	Grd. State	Isotope	Spin <sub>Nuclear</sub> ( $I$ )
57	Lanthanum	La <sup>3+</sup>	4f <sup>0</sup>	—	—	—
58	Cerium	Ce <sup>3+</sup>	4f <sup>1</sup>	<sup>2</sup> F <sub>5/2</sub>	—	—
59	Praseodymium	Pr <sup>3+</sup>	4f <sup>2</sup>	<sup>3</sup> H <sub>4</sub>	141	5/2
60	Neodymium	Nd <sup>3+</sup>	4f <sup>3</sup>	<sup>4</sup> I <sub>9/2</sub>	143   145	7/2   7/2
61	Promethium	Pm <sup>3+</sup>	4f <sup>4</sup>	<sup>5</sup> I <sub>4</sub>	147	7/2
62	Samarium	Sm <sup>3+</sup>	4f <sup>5</sup>	<sup>6</sup> H <sub>5/2</sub>	147   149	7/2   7/2
63	Europium	Eu <sup>3+</sup>	4f <sup>6</sup>	<sup>7</sup> F <sub>0</sub>	—	—
64	Gadolinium	Gd <sup>3+</sup>	4f <sup>7</sup>	<sup>8</sup> S <sub>7/2</sub>	—	—
65	Terbium	Tb <sup>3+</sup>	4f <sup>8</sup>	<sup>7</sup> F <sub>6</sub>	159	3/2
66	Dysprosium	Dy <sup>3+</sup>	4f <sup>9</sup>	<sup>6</sup> H <sub>15/2</sub>	161   163	5/2   5/2
67	Holmium	Ho <sup>3+</sup>	4f <sup>10</sup>	<sup>5</sup> I <sub>8</sub>	165	7/2
68	Erbium	Er <sup>3+</sup>	4f <sup>11</sup>	<sup>4</sup> I <sub>15/2</sub>	167	7/2
69	Thulium	Tm <sup>3+</sup>	4f <sup>12</sup>	<sup>3</sup> H <sub>6</sub>	169	1/2
70	Ytterbium	Yb <sup>3+</sup>	4f <sup>13</sup>	<sup>2</sup> F <sub>7/2</sub>	171   173	1/2   5/2
71	Lutetium	Lu <sup>3+</sup>	4f <sup>14</sup>	—	—	—

Table 3.1.: The lanthanide or rare earths with atomic number  $Z$ , full name, chemical symbol, the 4f shell configuration, the ground state, the odd numbered isotopes with the nuclear spin  $I$ . Data taken from [AB70]

With <sup>4</sup>I<sub>15/2</sub> for the erbium ion in the ground state, the first excited state is <sup>4</sup>I<sub>13/2</sub>. The separation between both states is  $\approx 6500 \text{ cm}^{-1}$  [AB70], which corresponds to  $\approx 1538 \text{ nm}$  and lies in the Telecom C-band. Also seen from table 3.1 is the odd valued isotope <sup>167</sup>Er with a nuclear spin of  $I = 7/2$ . In addition, erbium has five even isotopes <sup>162</sup>Er, <sup>164</sup>Er, <sup>166</sup>Er, <sup>168</sup>Er and <sup>170</sup>Er, possessing a nuclear spin  $I = 0$  and a natural abundance of 77.05 %. The natural abundance of the single odd valued isotope is typically 22.95 % [GNBG<sup>+</sup>06]. Such odd valued isotopes lead to hyperfine splittings, as discussed in section 3.1.2. In some systems the f electrons sometimes interact with nuclei of surrounding ligands, leading to the so called super-hyperfine or transferred hyperfine interaction, but can differ quite dramatically from one system to another ([TAC<sup>+</sup>10] see e.g. reference R.M. Macfarlane).

However, the super-hyperfine interaction will not be discussed in this thesis, where the interested reader is rather forwarded to last mentioned reference.

### 3.2.2. Erbium (Er<sup>3+</sup>) in Host Material YSO (Y<sub>2</sub>SiO<sub>5</sub>)

In erbium doped host crystals like YSO (yttrium orthosilicate, Y<sub>2</sub>SiO<sub>5</sub>), the erbium ion substitutes typically for the Y<sup>3+</sup> ions, occupying two distinct crystallographic sites, each with C<sub>1</sub> local symmetry<sup>7</sup>.

For each site there are four subclasses of sites with different orientations [SBTC08]. The crystal itself has the space group C<sub>2h</sub><sup>6</sup> with C<sub>2</sub> as the crystal  $b$  axis and  $a$ ,  $c$  perpendicular to it being the mirror plane. The lattice constants are  $a = 1.041 \text{ nm}$ ,  $b = 0.6721 \text{ nm}$  and  $c = 1.249 \text{ nm}$  with angle  $\beta$  (between  $a$  and  $c$ ) having a value of  $102^\circ 39'$  [SBTC08].

The previously mentioned four subclasses of sites are related by the C<sub>2</sub> rotation and inversion, which means, those related by inversion interact identically with a magnetic field vector lying in the mirror plane or along the  $b$  axis, quoting magnetic equivalent. Whereas those related by a C<sub>2</sub> rotation are magnetically inequivalent.

<sup>7</sup> Using in this thesis the Schönflies notation

By convention, the crystal axes in the mirror plane are labeled according to the optical extinction axes  $D_1$  and  $D_2$ , where  $D_1$  is  $23.8^\circ$  from the  $c$  axis and  $78.7^\circ$  from the  $a$  axis, with  $D_1$  perpendicular to  $D_2$  [SBTC08]. We will use the  $D_1$ - $D_2$ - $b$  coordinate system in this thesis, where the azimuthal angle  $\phi$  lies in the  $D_1$ - $D_2$  plane, defined counterclockwise from  $D_1$ . The polar angle  $\theta$  is defined from  $b$ . The angles  $\phi$  and  $\theta$  are used to define the position according to an applied magnetic field. These conditions are schematically presented in figure 3.13:

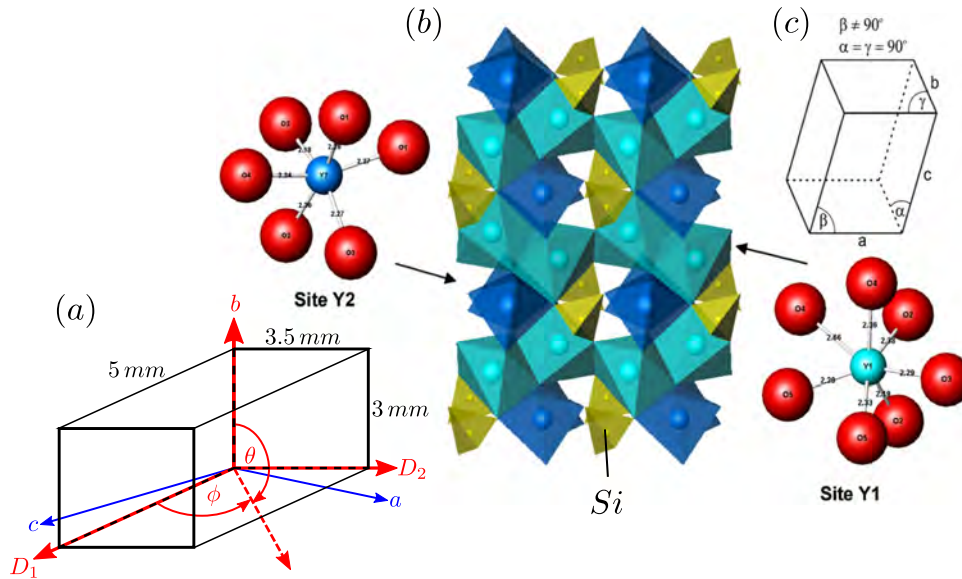


Figure 3.13.: Yttrium orthosilicate (YSO). (a) Crystal dimensions with crystal axes  $a$ ,  $b$  and  $c$ , as used in experiment. More frequently the axes  $b$ ,  $D_1$  and  $D_2$  (optical excitation axes) are used.  $\theta$  and  $\phi$  describe the crystal position according to an applied magnetic field. (b) Schematic crystalline structure of YSO. Site 1 is colored in cyan or light blue and site 2 in dark blue. The difference between site 1 and site 2 is the number of neighboring Oxygen ions of the yttrium ion. Site 1 possesses 7 Oxygen ions, whereas site 2 has 6. Silicon is marked in yellow. Typically the erbium ion substitutes for the yttrium ion. (c)  $C_{2h}$  monoclinic Schönflies representation of the crystal geometry. The lengths  $a$ ,  $b$  and  $c$  are not equal and angle  $\beta = 102^\circ 39'$  ( $\beta \neq 90^\circ$ ). (b) and (c) taken from [DVA<sup>+</sup>08]

For the magnetically equivalent sites, there should be only two transitions observed for each site regarding the ground state in ESR spectroscopy, whereas for the magnetically inequivalent sites maximum four transitions (i.e. two per each site) are observable. In ESR spectroscopy these transitions are observed due to the splitting of the lowest Kramers doublet in a static magnetic field.

In principal, the 'free ion' levels are modified by the weak crystal field, where the term weak means a relatively low interaction or influence of the 4f electrons due to the shielding of higher occupied shells.

In case of the odd electron number of the 4f shell, each level (here  $^4I_{15/2}$  and  $^4I_{13/2}$ ) is split into eight degenerate Kramers doublets ( $J + 1/2$ ), there the lowest two doublets of the ground state  $^4I_{15/2}$  are separated by  $\approx 33.3 \text{ cm}^{-1}$  or  $\approx 1 \text{ THz}$  [BFR<sup>+</sup>11].

At low temperatures the lowest lying doublet is treated typically as effective spin  $S'$  at cryogenic temperatures, which split according to the applied magnetic field and due to Kramers theorem. This splitting lies in the typical ESR region of some GHz [BFR<sup>+</sup>11], depending on the applied external magnetic field.

Furthermore, due to the odd valued isotope  $^{167}\text{Er}$ , additional hyperfine splittings occur, splitting the effective spin energy levels into eight ( $I + 1/2$ ), each with nuclear magnetic numbers  $7/2, \dots, -7/2$ .

The previously discussed energy levels are summarized in figure 3.14:

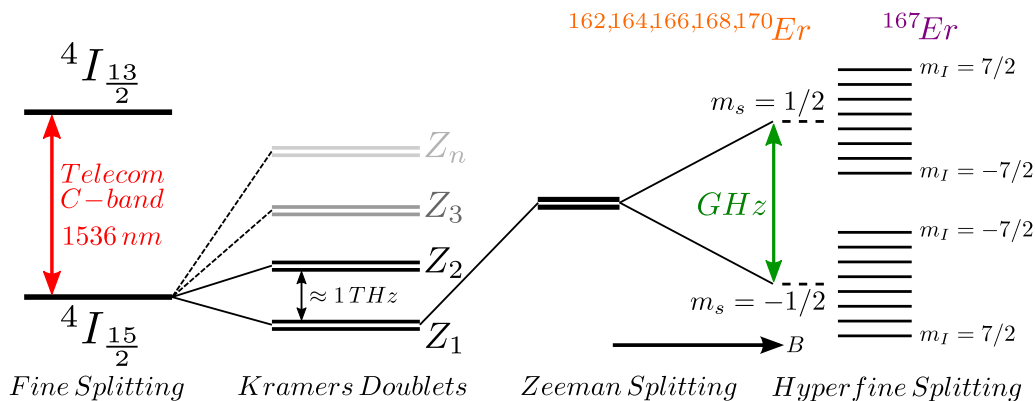


Figure 3.14.: Energy level scheme of Er:YSO. The fine splitting energy difference lies in the Telecom C-band region, whereas a weak crystal field splits the Kramers ion into 8 doublets for each fine splitting energy level. Furthermore, the Kramers doublet splits in presence of a magnetic field into two levels, each with 8 hyperfine levels if an odd valued erbium isotope is present. (See also [BFR<sup>+</sup>11])

### 3.2.3. Erbium ( $\text{Er}^{3+}$ ) in Host Material YAlO (YAlO<sub>3</sub>)

Yttrium orthoaluminate (YAlO) or yttrium aluminum perovskite (YAP), according to its orthorhombically distorted perovskite structure, belongs to the  $D_{2h}$ , Pnma space group number 62 [BSBS09].

Using the Pnma description, the lattice parameters are given as  $a = 0.5330$  nm,  $b = 0.7375$  nm and  $c = 0.5180$  nm [BSBS09], whereas describing it for the orthorhombic space group D-Pbnm, the parameters are  $a = 0.5180$  nm,  $b = 0.5330$  nm and  $c = 0.7375$  nm [ARM97].

The elementary orthorhombic cell contains four magnetic sites for  $\text{Al}^{3+}$  and  $\text{Y}^{3+}$ . The locations of the  $\text{Y}^{3+}$  ions are paired by an inversion through the  $\text{Al}^{3+}$  sites. Therefore containing two magnetically non-equivalent positions which can be resolved when a magnetic field is applied in the plane of  $a$  and  $b$  according to the D-Pbnm space group description.

In case of planes  $bc$  and  $ac$ , all positions are magnetically equivalent. Thus they are unresolved in ESR spectroscopy [ARM97].

The nearest neighbors of  $\text{Al}^{3+}$  are six oxygen ions with a weakly perturbed octahedral structure and in case of  $\text{Y}^{3+}$ , the local environment consist out of eight oxygen ions. Typically, the RE ions (e.g. erbium) substitute for the  $\text{Y}^{3+}$  ions [ARM97].

The described structure is schematically presented in figure 3.15 on the next page.

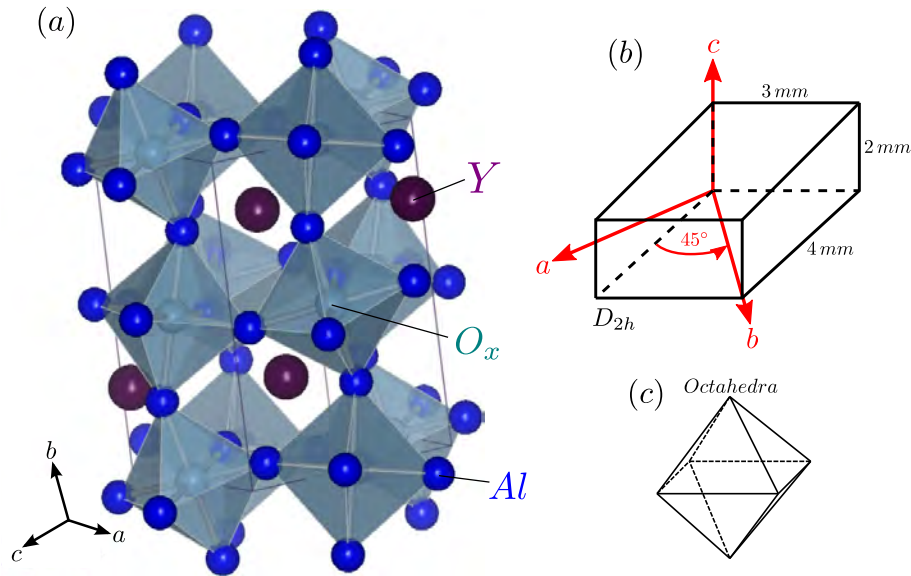


Figure 3.15.: Yttrium orthoaluminate (YAIO). (a) Schematic crystalline structure of Er:YAIO. Yttrium ions are colored in purple, whereas the Oxygen ions are colored light blue. Aluminum is colored dark blue. The coordinate system is presented for the  $Pnma$  space group description. (b) Crystal dimensions with crystal axes  $a$ ,  $b$  and  $c$ , as used in experiment. The crystal has a  $D_{2h}$  representation according to the Schönflies notation. Local octahedral (c) structures are formed by Aluminum and Oxygen ions. (a) taken from [BSBS09]

In principle, the same energy level diagram as seen in in figure 3.14 can be adopted for erbium in YAIO.

### 3.3. Waveguide Resonators

Resonator cavities, no matter if rectangular, cylindrical or even arbitrary shaped, are an important part of ESR spectroscopy, e.g. as used by J. Colton and L. Wienkes [CW09].

Since decades such cavities are used as filters, frequency meters, or as powerful tools to determine specimen properties like the permittivity [KKS<sup>+</sup>12]. Due to cavity design possibilities, the ability of choosing or selecting certain frequency modes is given, as well as to have a certain area or volume with distinct electric and magnetic fields. Such fields, e.g. the magnetic field, could be found to penetrate oscillatory a certain volume of interest in a homogeneous manner, as homogeneity is an important aspect as discussed in section 3.1.3.

This section will focus on discussions regarding cylindrically shaped waveguide cavity resonators and its properties. Furthermore, we will discuss how such properties could be modified in order to reach certain criteria for ESR spectroscopy, as well as how to extract and interpret the signals.

Discussion including other types of cavity resonators are found in [Hil09, ZL08, Col01].

In this thesis such resonators are termed 'three dimensional' (3D), which, besides the entire size of such an cavity, could be associated with relatively 'big' modal volumes occupied by the electromagnetic field as compared to e.g. lumped element resonators.

### 3.3.1. Circuit Model, Q-Factors and the Observed Spectra

Before describing the cavity of a cylindrical waveguide resonator (CWR) in detail, first a treatment in case of simplified lumped elements is given. Such description of the operation of a microwave resonator is very similar to that used in circuit theory.

In this section we will treat the case of series and parallel resonant circuits, where the case of being close to the resonance frequency is used in order to be able to use the *RLC* (Resistor, Inductor and Capacitor, respectively) model of equivalent lumped element circuits [Poz11].

The circuit representation of a series (a) and parallel (b) *RLC* resonator is depicted in figure 3.16, also showing the response of such a circuit as the input impedance versus angular frequency, (b) and (d) respectively:

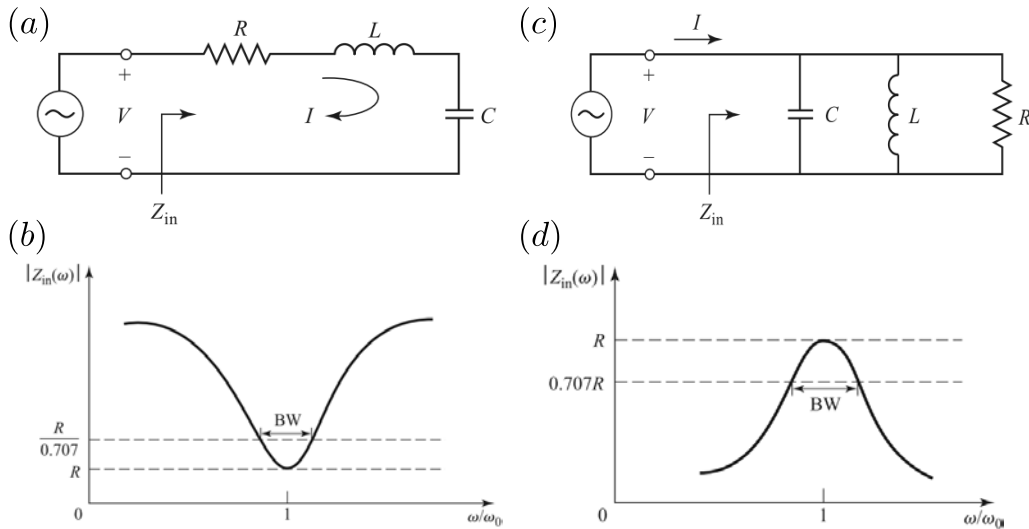


Figure 3.16.: (a) Circuit representation of a lumped element series *RLC* (Resistor, Inductor and Capacitor).  $L$  and  $C$  describe the resonance frequency according to  $\omega = LC^{-1/2}$ , whereas  $R$  represents the resonator losses. (b) Response graph of a series *RLC* resonator in terms of the impedance  $Z$  and angular frequency  $\omega$ . Only at resonance ( $\omega = \omega_0$ ) the impedance is mainly determined by the resistance  $R$ . Otherwise for  $\omega \neq \omega_0$  the impedance is increasing. (c) Circuit representation of a parallel *RLC* resonator with lumped elements. (d) Response graph of a parallel *RLC* resonator. Nearly the same situation like in (b), except that for  $\omega \neq \omega_0$  the impedance is decreasing. Figures taken from [Poz11]

As it is seen from figure 3.16 (d), for a parallel resonant circuit at resonance ( $\omega = \omega_0$ ) the magnitude of the input impedance ( $|Z_{in}|$ ) of the system equals just  $R$  (real value), i.e. the supplied power is completely dissipated at an equivalent resistor (accounting for power loss) if the impedance of the power supply port is matched.

Same applies for the series resonant circuit [figure 3.16 (b)], except that for frequency detuning ( $\Delta\omega = \omega - \omega_0$ ) the input impedance is rising, where in the parallel case the magnitude of  $|Z_{in}|$  is dropping. Therefore the series *RLC* is the dual impedance of the parallel *RLC*.

However, in both cases the resonance frequency  $\omega_0$  is determined by the values of the inductance ( $L$ ) and capacitance ( $C$ ) part, given as [Poz11]

$$\omega_0 = \frac{1}{\sqrt{LC}}. \quad (3.32)$$

In a picture of a propagating electromagnetic (EM) wave with certain impedance, e.g. in case of the parallel circuit, such a wave will propagate without reflections [ $r = (Z_{Wave} - Z_{in}) / (Z_{Wave} + Z_{in})$ ] if both impedance values are equal ( $r = 0$ ). For a dropping  $|Z_{in}|$  [figure 3.16 (d)] the incoming wave is rather reflected than transmitted. Thus, only in case of resonance a signal is detected in transmission, which can be seen as a bandpass filter only transmitting signals in the region around  $\omega_0$ .

Another way to picture this behavior is presented figure 3.17:

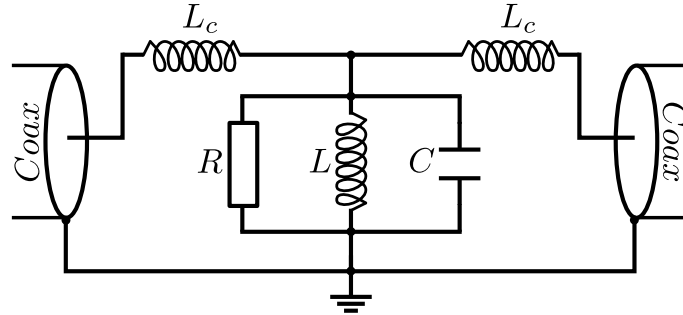


Figure 3.17.: Parallel  $RLC$  representation of a resonator modeled via lumped elements. The coupling is indicated by  $L_c$  (inductive) to an external circuitry, being here the coaxial cables. Furthermore, capacitive coupling is also possible, just replacing the elements  $L_c$  by  $C_c$ .

Figure 3.17 is again the parallel case, but now connected to coaxial cables. Two additional inductors ( $L_c$ ) just represent an inductive coupling to the circuit. Ways to couple to a resonator will be explained in section 3.3.3 in more detail and should not be taken into account for now.

Remembering the impedance behavior of the parallel circuit, for transmitting signals from one transmission line to the other, apart from resonance, the incoming signal will take the 'short' way via the  $RLC$  circuit to ground. Only in the vicinity of resonance a signal will be transmitted, as previously described in case of the EM wave. For a series  $RLC$  the impedance behavior is vice versa and therefore only at resonance the signal will take the short to the ground, indicated by an inverted transmission signal compared to the parallel  $RLC$  case. Typically such signals are measured in power ratios of decibels (dBm), where the measured power reference is 1 milliwatt (mW). The graphs are usually presented in dB versus frequency, where the applied power in watts should be known. If for example applying 1 mW, this refers to 0 dBm, calculated via

$$X_{dBm} = 10 \log_{10} \frac{P}{P_{ref}}. \quad (3.33)$$

$P$  is the applied power in milliwatts and  $P_{ref}$  is the reference power of 1 mW. Hence, if observing a certain dB value at resonance, say -3 dBm in case of a parallel circuit, 1 dBm (1 mW) is applied and only  $\approx 0.5$  mW are transmitted.

This value can be calculated by reformulating equation 3.33 for  $P$ . In terms of applied voltage this leads to a drop of  $1/\sqrt{2}$  or  $\approx 0.707$ , as also shown in figure 3.16. Frequency values found on this curve at values -3 dB from the peak value of the curve (resonance frequency) are referred to as the bandwidth. For a frequency detuning of  $\Delta\omega = \omega - \omega_0$ ,  $|\Delta\omega|$  is defined as the half width at half maximum (HWHM) bandwidth, whereas  $2 \cdot |\Delta\omega|$  is the full width at half maximum (FWHM). Recent discussion is graphically presented in figure 3.18 for more clarity on the next page.

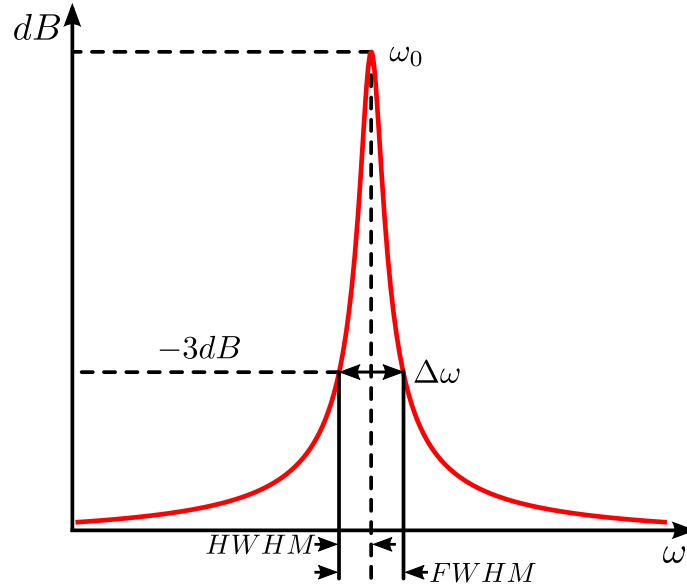


Figure 3.18.: Lorentzian shaped transmission signal in Decibel (dB) versus angular frequency  $\omega$ . The resonance frequency is indicated by  $\omega_0$  and the bandwidth  $\Delta\omega$  is determined at -3dB (at half values of the maximum). Such a bandwidth can be defined at half of full width values, typically abbreviated HWHM (Half Width at Half Maximum) and FWHM (Full Width at Half Maximum).

Another very important parameter using the values of the resonance frequency and bandwidth is the so called dimensionless quality factor  $Q$ . This parameter specifies the frequency selectivity and performance of a resonant circuit in general [Col01]. The very fundamental definition of the  $Q$ -factor is:

$$Q = \omega_0 \frac{\text{time averaged energy stored in a system}}{\text{energy loss of the system per period}}, \quad (3.34)$$

or just in terms of the angular frequency  $\omega$ :

$$Q = \frac{\omega_0}{\Delta\omega}. \quad (3.35)$$

At resonance, the lumped element  $R$  represents the losses of the circuit. In this case, usually the quality factor  $Q$  is called the unloaded or internal quality factor  $Q_i$ .

If other losses are present, e.g. due to external circuits coupled to the main circuitry, typically this is called the external quality factor  $Q_e$ . If determining the quality factor from a transmission signal, the measured  $Q$ -factor is often the sum of several reciprocal  $Q$ -factors, leading typically to the loaded quality factor

$$\frac{1}{Q_L} = \frac{1}{Q_i} + \frac{1}{Q_e} + \frac{1}{Q_x}, \quad (3.36)$$

where  $Q_x$  could be any kind of additional loss contribution.

Furthermore, the unloaded or intrinsic  $Q$ -factor of a cylindrical cavity resonator is described as

$$\frac{1}{Q_i} = \frac{1}{Q_c} + \frac{1}{Q_d}, \quad (3.37)$$

where  $Q_c$  represents the quality factor influenced by the material conductivity from which the cavity is made of.  $Q_d$  describes the quality factor influenced by dielectric material losses, if present in the cavity [Poz11]. The dielectric quality factor is  $Q_d = 1/\tan\delta$ , with  $\tan\delta$  as the dielectric loss tangent.

In turn, the expression for the quality factor according to the conductivity contains more terms and constants and is described by Collin [Col01] for  $TE_{nml}$  modes as

$$Q_c \frac{\delta}{\lambda} = \frac{\left[1 - \left(\frac{n}{p'_{nm}}\right)^2\right] \sqrt[3]{(p'_{nm})^2 + \left(\frac{l\pi a}{d}\right)^2}}{2\pi \left[(p'_{nm})^2 + \frac{2a}{d} \left(\frac{l\pi a}{d}\right)^2 + \left(1 - \frac{2a}{d}\right) \left(\frac{nl\pi a}{p'_{nm}d}\right)^2\right]} \quad (TE). \quad (3.38)$$

Here,  $n$  and  $l$  are the corresponding integer mode numbers, where  $p'_{nm}$  is the  $m^{th}$  root of the first derivative of the  $m^{th}$  Bessel function [Poz11]. Furthermore,  $a$  is the radius and  $d$  the length of the cavity.

Moreover, the skin depth is represented by  $\delta$ , where  $\lambda$  is the wavelength. All parameters are summarized in the following equation:

$$\delta = \frac{1}{\sqrt{2\pi f \mu \sigma / 2}}. \quad (3.39)$$

Equation 3.39 contains the material dependent properties of the cavity as the permeability  $\mu$  and the conductivity  $\sigma$ , where  $\lambda$  is the wavelength. Finally the quality factor for a certain mode is obtained in dependence of its frequency given by the geometry of the cavity and the material dependent values.

In order to calculate the quality factors for the  $TM_{nml}$  modes, the following equation has to be used [Col01]:

$$\begin{aligned} Q_c \frac{\delta}{\lambda} &= \frac{\sqrt{p_{nm}^2 + (l\pi a/d)^2}}{2\pi(1 + 2a/d)} \quad \text{for } l > 0 \quad (TM) \\ Q_c \frac{\delta}{\lambda} &= \frac{p_{nm}}{2\pi(1 + a/d)} \quad \text{for } l = 0 \quad (TM). \end{aligned} \quad (3.40)$$

At cryogenic temperatures the value of the conductivity  $\sigma$  changes, as its reciprocal value  $\rho$  (specific resistance) decreases due to less thermal interactions of the charge carriers with the crystalline lattice. One way to determine the new value of  $\sigma$  at cryogenic temperatures is the Widemann-Franz-Law, applicable from 4 to 300 Kelvin [Pob07].

An increasing conductivity will lead to a higher  $Q_c$  value, as the overall value in the square root of the skin depth  $\delta$  increases, which is seen from equations 3.38 and 3.39 or 3.40.

According to equation 3.37 the internal quality factor  $Q_i$  and proportional to it the loaded quality  $Q_L$  should rise.

In order to complete the discussion of this section, two ways of the observed spectra will be presented:

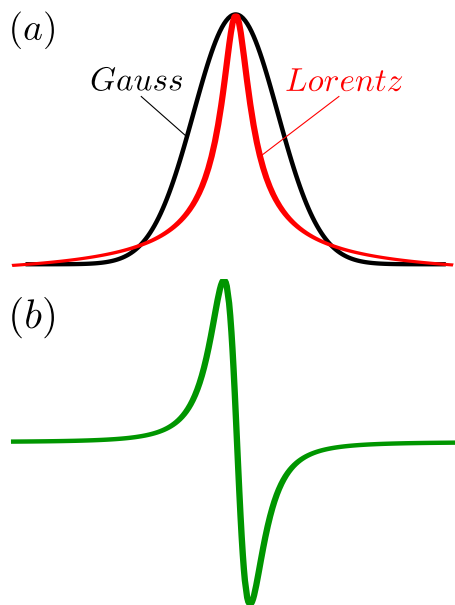


Figure 3.19.: (a) Transmission signals with a Lorentzian (red) or Gaussian (black) line shape. In this thesis usually Lorentzian shaped signals are observed. (b) First derivative of the Lorentzian line shape. Such a signal is e.g. observed on frequency changes of the main resonance frequency, indicating dispersion.

Figure 3.19 (a) shows the already know transmission signal. Depending on the physics acting inside a resonator, the observed signal could obtain a Lorentzian or Gaussian shape, represented respectively by its mathematical functions. Even sometimes convolutions of both kinds are possible, denoted as Voigt shaped [Eic13].

Assuming the signal being indicated by the Q-factor of the resonator, on magnetic resonance there will be also a contribution of  $Q_x$ . Thus, if a magnetic field is applied to the resonator, for zero field the value of  $1/Q_x$  in equation 3.36 could be neglected. But contributions are found maybe for a certain field strength  $> \text{zero}$  when in magnetic resonance.

Therefore, for the mentioned resonance case  $Q_L$  has to change as the value of  $\Delta\omega$  changes, indicating absorption. But also a change in frequency is possible, denoted as dispersion. If now the detected signal is plotted versus the magnetic field, both, the absorption and dispersion is detectable. Thus, figure 3.19 (b) will be obtained, which is in mathematical terms the first derivative of (a).

Such a correlation is typically found for the susceptibility  $\chi$ , which describes the response of a material to an applied external field, e.g. derived by the Drude-Lorenz model if describing  $\chi$  in terms of real and imaginary parts. In this case, the real part is typically observed as shown in figure 3.19 (a), describing the absorptive part of the material, whereas the imaginary part is observed as shown in figure 3.19 (b), describing the dispersion. Both parts could be interchanged by the Kramers-Kronig relation [Boy08].

### 3.3.2. Resonant Frequencies and the TE<sub>011</sub> Mode

Resonant frequencies in a waveguide resonator are achieved by introducing bottom and upper caps to the waveguide. In this case the propagating electromagnetic (EM) waves are reflected at such reflecting barriers, leading to certain standing waves determined by the dimensions. From considerations like found for laser resonators or the Fabry-Pérot-Interferometer, a longitudinal mode is determined by  $d = \lambda/2$ , where  $d$  is the distance between two reflecting barriers aligned parallel to each other and  $\lambda$  is the wavelength. In order to get a resonating longitudinal mode in the single valued GHz range, from  $\lambda = c/f$  and using  $f = 7$  GHz,  $\lambda$  equals approximately 4.28 cm. To get this wavelength resonating between to reflectors, its separation should therefore equal half of the wavelength or 2.14 cm.

In a waveguide resonator not only longitudinal modes are present, but also transverse modes, typically termed transverse electric (TE) or transverse magnetic (TM) modes, where transverse means transverse to the axis of EM wave propagation. In case of TE modes, the electric field component in the direction of propagation is zero, but which does not count for the magnetic field component (longitudinal component). The situation is reversed for TM modes. However, the waveguide, which is here a cylinder, is also determined by a radial dimension  $a$ , like depicted in figure 3.20:

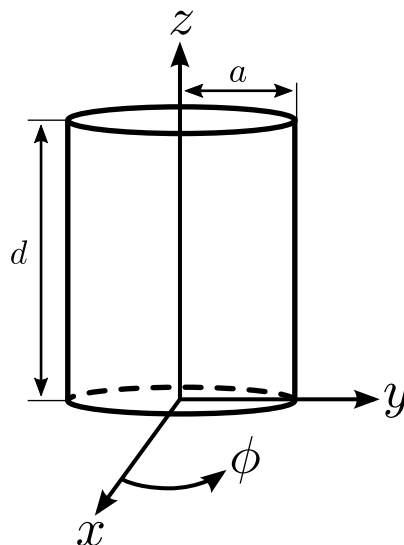


Figure 3.20.: Waveguide with end caps, forming a cylinder. Dimensions are described by  $a$  (radius) and  $d$  (length).  $\phi$  describes the azimuthal angle.

The resonant TE modes in terms of frequency for cylindrical cavities are thus determined by

$$f_{nml} = \frac{c}{2\pi\sqrt{\mu_r\epsilon_r}} \sqrt{\left(\frac{p'_{nm}}{a}\right)^2 + \left(\frac{l\pi}{d}\right)^2}, \quad (3.41)$$

where  $\mu_r$  and  $\epsilon_r$  (permeability and permittivity) describe the material properties inside the cylinder and  $p'_{nm}$  is the  $m^{\text{th}}$  root of the  $n^{\text{th}}$  Bessel function [Poz11]. For TE modes, the first derivative of the Bessel function is used, indicated by  $p'$ , whereas for TM modes also equation 3.41 applies, only replacing the first derivative of the Bessel function ( $p'_{nm}$ ) by its anti-derivative  $p_{nm}$ . As mentioned, the subscript letters  $n$  and  $m$  are represented by the Bessel function, whereas the final letter  $l$  indicates the number of half wavelengths resonating in the direction of propagation, which typically is set to the z-axis.

Some modal field distributions according to cylindrical waveguide resonators are presented in figure 3.21:

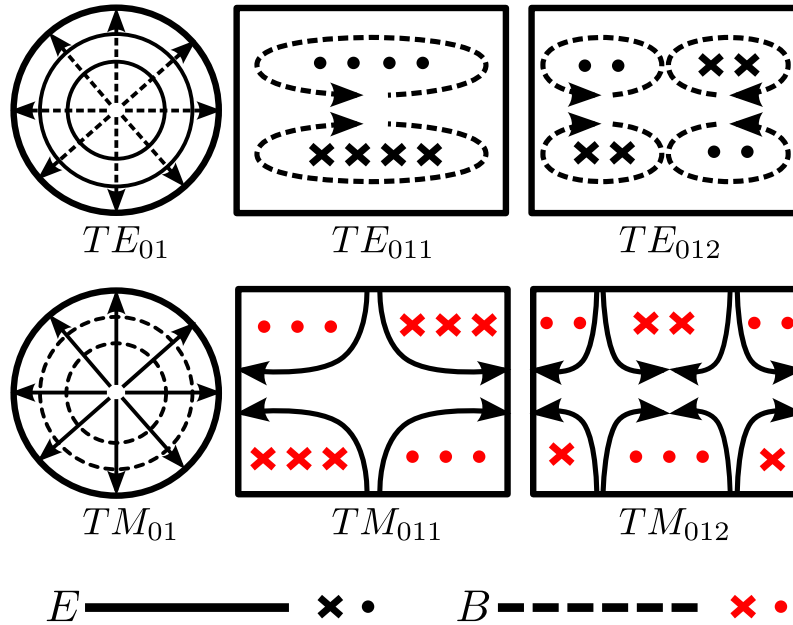


Figure 3.21.: Possible field distribution in a cylindrical cavity. The circles on the left hand side indicated by  $TE_{01}$  and  $TM_{01}$  are the top or bottom view of the cylinder ( $xy$ -plane). The rectangular shapes show the lateral view. Here  $x$  describes the field pointing into the paper plane and a dot indicates the field pointing out of the paper plane.

Figure 3.21 (a) shows that the  $TE_{011}$  mode has a special property. The magnetic field component  $B$  of the EM field is penetrating the center of the cylinder, where at the exact central point the magnetic field lines are parallel, i.e. homogenous (high concentration of magnetic field lines). Such a homogenous B-field is practicable in order to keep the inhomogeneous broadening of the spin ensemble low and to observe therefore a relatively small linewidth.

Usually, ESR experimentalists use this mode as there is no electric current flow into the radial ( $a$ ), nor the longitudinal direction ( $z$ ), but only in the azimuthal ( $\phi$ ) direction. This allows the usage of a tuning plunger on one of the end plates for frequency variations [Poo67].

Another advantage of such a current flow is the ability to make holes in the side of the cavity for e.g. optical access [CW09], or to couple external circuitry to the resonator, as it is used in this thesis.

Additional and more detailed modal field distributions regarding waveguide resonators are also found in [ZL08, Poz11], or in general for rectangular and circular waveguides C. S. Lee et al. [LLC85] is recommended.

For example, if using an air<sup>8</sup> filled copper cavity ( $\sigma = 5.96 \cdot 10^7$  S/m at 20° C [Poz11]) of dimensions  $a = 0.01$  m and  $d = 0.0205$  m, from equations 3.41, 3.38 and 3.40, subsequent values of table 3.2 are calculated.

Transverse Electric (TE)			Transverse Magnetic (TM)		
Freq. [GHz]	Mode [nml]	$Q_c (Q_i)$	Freq. [GHz]	Mode [nml]	$Q_c (Q_i)$
11.457	1 1 1	11636.08	11.475	0 1 0	11051.87
16.304	2 1 1	11225.06	13.607	0 1 1	9063.03
17.060	1 1 2	14313.88	18.284	1 1 0	13950.40
19.692	0 1 1	21612.41	18.589	0 1 2	10593.07
—	—	—	19.692	1 1 1	10902.83

Table 3.2.: First few TE/TM resonant frequency modes and its Q-factors for an air (or vacuum) filled cylindrical cavity with dimensions  $a = 0.01$  m and  $d = 0.0205$  m, up to a frequency of 20 GHz.

The values in table 3.2 have been calculated by using further values as  $\epsilon_0 = 8.854 \cdot 10^{-12}$  Am/Vs,  $\mu_0 = 4\pi \cdot 10^{-7}$  Vs/Am [Poz11], and the permeability of copper ( $\mu_r \approx 1$ ) for the skin depth formula. Furthermore, the calculations show that the lowest TE mode is found at 11.457 GHz with mode numbers 111. The lowest TM mode is also found at 11.457 GHz and is thus degenerate in frequency with the TE<sub>111</sub> mode. The difference between the modes is found for the intrinsic quality factors, which is higher for the TE<sub>111</sub> mode. The desired TE<sub>011</sub> mode is found at 19.692 GHz. In order to have the TE<sub>011</sub> mode resonating at lower frequencies, the usage of a high valued dielectric material with permittivity  $\epsilon_r$  is recommended. Subsequent figure demonstrates the effect of different valued dielectrics scaling the radius  $a$  of a cylindrical cavity for frequency values between 1 and 20 GHz:

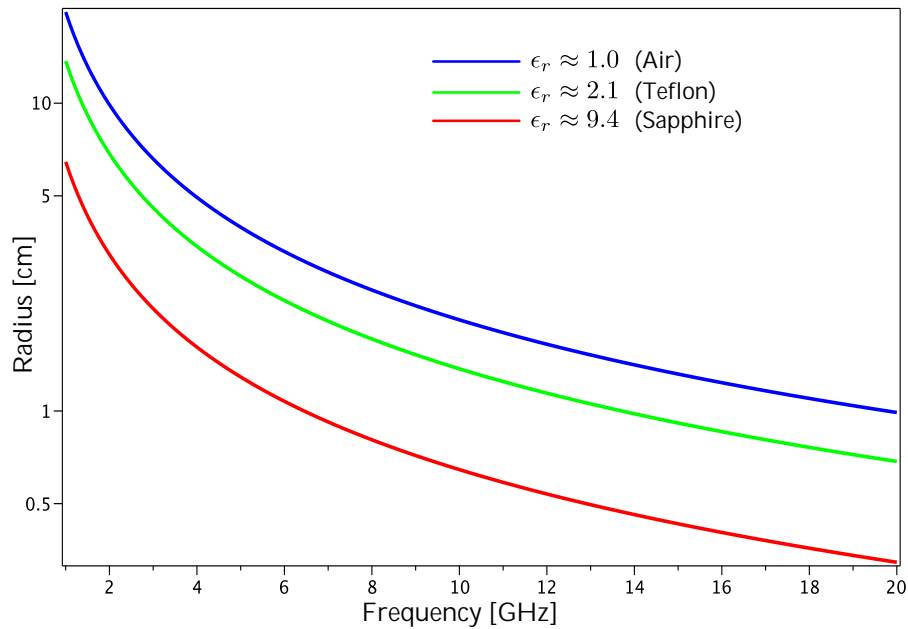


Figure 3.22.: Illustration of some dielectric materials with permittivity  $\epsilon_r$  influencing the resonant frequency of a certain mode with respect to the radius (here: logarithmic scaled) of a cylindrical cavity. In order to fix a mode at a certain frequency, values of the radius could be adjusted, whereas it is recommended to use a dielectric inside the cavity to scale down the resonant frequencies further.

Figure 3.22 clearly shows that for an air filled cavity the radius is increasing with decreasing resonance frequency. This effectively leads to an overall increase of the cavity volume. As

<sup>8</sup>  $\epsilon_r = 1$  and  $1/Q_d = 0$

it will be discussed in section 3.4, the volume of the cavity should be as small as possible. Therefore sapphire<sup>9</sup> as a high valued dielectric material with a loss tangent of  $\approx 1 \cdot 10^{-7}$  [TF85] is used to scale down the resonant frequencies of the waveguide resonators, as used in this thesis.

### 3.3.3. Two-Port Networks and External Coupling

Direct measurements of voltages and currents at microwave frequencies usually involve the magnitude and phase of a traveling or standing wave. Thus, equivalent voltages and currents become somewhat of an abstraction when dealing with high-frequency networks. A representation more in accord with direct measurements, and with the ideas of incident, reflected, and transmitted waves, is given by the scattering matrix. The scattering matrix provides a complete description of the network, where the parameters can be measured directly with a vector network analyzer (VNA). Once the scattering parameters of the network are known, conversion to other matrix parameters can be performed, if needed [Poz11].

A typical scattering matrix for a two port system is given as follows:

$$\begin{bmatrix} V_1^- \\ V_2^- \end{bmatrix} = \begin{bmatrix} S_{11} & S_{12} \\ S_{21} & S_{22} \end{bmatrix} \begin{bmatrix} V_1^+ \\ V_2^+ \end{bmatrix}, \quad (3.42)$$

where the physical meaning of  $S_{11}$  is the reflection on port 1 and  $S_{22}$  is the reflection at port 2.  $S_{12}$  is the transmission from port 1 to 2 and  $S_{21}$  is the transmission from port 2 to 1.  $V_1^+$  and  $V_2^+$  are the amplitudes of the incident voltage waves, and  $V_1^-$  and  $V_2^-$  are the amplitudes of the reflected voltage waves, as depicted in figure 3.23 using  $a_1$ ,  $a_2$  and  $b_1$ ,  $b_2$ , respectively.

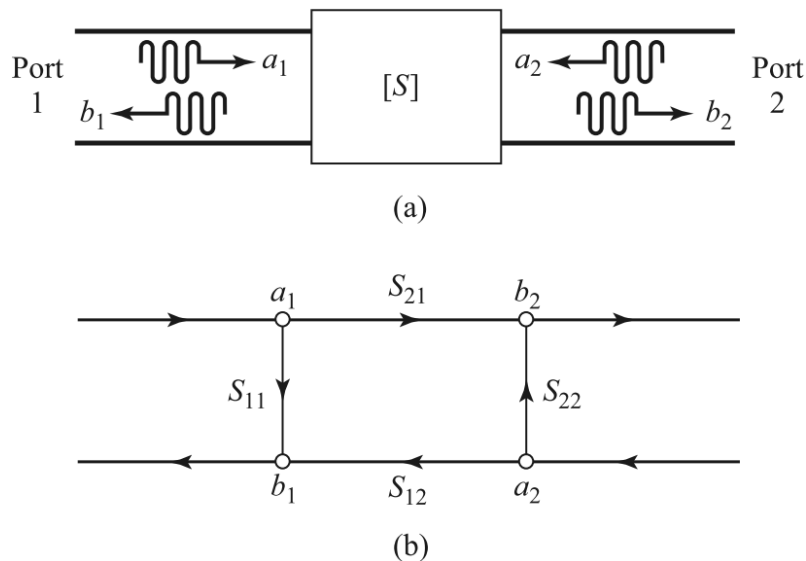


Figure 3.23.: (a) Schematic representation of the scattering matrix  $S$  (two port network), with incoming waves  $a_1$ ,  $a_2$  and reflected waves  $b_1$ ,  $b_2$  at ports 1 and 2. (b) Signal flow graph, in analogy to (a).  $S_{11}$  for example is measured between node  $a_1$  and  $b_1$ , i.e. incident and reflected waves. Figures taken from [Poz11].

<sup>9</sup> Sapphire has anisotropic  $\epsilon_r$  values, typically denoted by a value of  $\approx 11.6$  parallel and  $\approx 9.4$  perpendicular to the crystal axis (room temperature) [TF85]

Using scattering matrices, a complete description of the network is possible. However, for measuring or evaluating the resonant frequencies and quality factors, the transmission parameter  $S_{21}$  is sufficient and will be used usually in this thesis.

In order to provide microwave energy to the resonator, external couplers like probes, loops or apertures [Col01] are frequently used (figure 3.24). In case of probes or loops usually coaxial cables are used. In case of aperture coupling, EM waves are delivered via waveguides, which are themselves again probe or loop coupled.

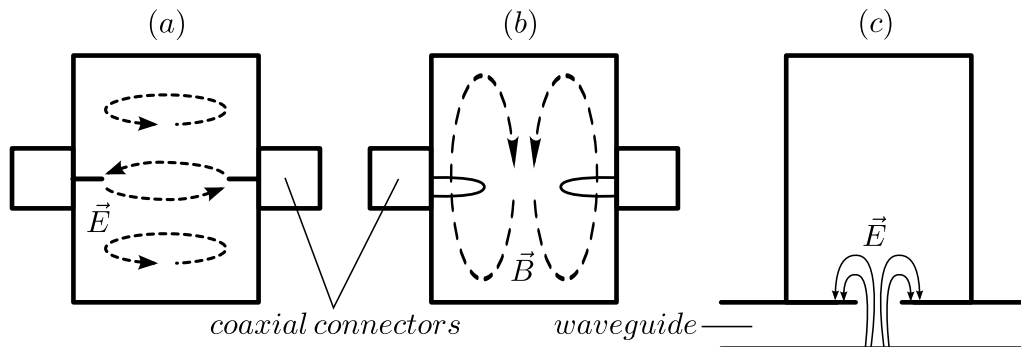


Figure 3.24.: External coupling to cavity. (a) Probe coupled cavity. The probes, or pins could be assumed to act like antennas. Such a variant is more sensitive to the E-field. (b) Loop coupled cavity, where in this case the end of the wire is grounded to the cavity wall. The flux of a B-field through the area spanned by the loops will determine the sensitivity or coupling, which is usually more sensitive to B-fields. (c) Aperture coupled cavity, where the size and shape of the aperture determines the coupling to the cavity.

Coupling to the magnetic field is enhanced by using loops, as the area confined by such a loop determines the induced currents in the loop wire, or vice versa. Increasing this area will lead to a higher coupling to the cavity or resonator, as a higher flux of the magnetic field is collected. In such a case the cavity is said to be inductively coupled, as depicted in figure 3.17 by  $L_C$  in section 3.3.1. In order to couple effectively to the magnetic field of a  $TE_{011}$  mode, coupling loops should be used, as it will be the case for this thesis.

Any of the previously described coupling cases will have influences onto the measured or loaded quality factor, which is determined by the external Q-factor. Thus, from equation 3.36 it is known that the reciprocal loaded quality factor is the sum of the reciprocal intrinsic and external quality factors, neglecting here  $1/Q_x$ . In order to determine the external quality factor, the intrinsic quality factor should be known. An approach to determine the intrinsic Q-factor is given by D. Kajfez et al. [KCAGK99] as

$$Q_i = Q_L(1 + 2\kappa). \quad (3.43)$$

In equation 3.43,  $\kappa$  is the coupling coefficient. If the coupling is on both sides the same,  $\kappa$  is multiplied by 2.

Furthermore,  $2\kappa$  is determined by  $|S_{21e}| / (1 - |S_{21e}|)$ , where  $|S_{21e}|$  is the real valued magnitude at resonance. This only holds if influences like noise, crosstalk, delay of uncalibrated lines etc. could be neglected or are known. In case of different coupling coefficients on both sides, rather the procedure explained by K. Leong and J. Mazierska [LM02] should be used.

As the transmission lines in a cryostat are attenuated at different temperature stages, measurements of e.g.  $S_{11}$  at cryogenic temperatures would need amplifiers on the way

back to port 1, as the signal would be damped by the attenuators again. Such an amplifier was not used for the measurements of this thesis and thus only the  $S_{21}$  data was measured for  $\kappa > 1$ . In order to still determine the internal quality factors without using  $S_{11}$  data, the subsequent described procedure is used.

In case of a under-coupled cavity, i.e.  $\kappa \ll 1$ , the loaded Q-factor equals approximately the intrinsic Q-factor like also deducible from equation 3.43. From measurements of  $Q_L$  at room temperature and cryogenic temperatures with an under-coupled cavity, a factor  $f_{Q_i}$  could be determined. This factor is the ratio of  $Q_i/Q_L$  and describes just the Q-factor increase at low temperatures. The external quality factor  $Q_e$  is determined at room temperature for an over-coupled cavity and does not change at cryogenic temperatures. Using this set of values, the internal Q-factor for an over-coupled cavity at low temperatures can be written as:

$$\frac{1}{Q_{i,ct}} = \left( \frac{1}{Q_{L,ct}} - \frac{1}{Q_{e,rt}} \right) (f_{Q_i})^{-1}. \quad (3.44)$$

In this equation  $Q_{L,ct}$  is the loaded quality factor at cryogenic temperatures (ct) and  $Q_{e,rt}$  is the external quality factor determined at room temperature (rt).

### 3.4. Cavity Quantum Electrodynamics

Cavity quantum electrodynamics (cavity QED) studies the interaction of light and matter at the quantum level. A metaphorical description is just the presence of a atom with two quantum levels, coupled to a single electromagnetic mode of a cavity. If the cavity consists out of two mirrors, the photon bounces between both, indicated by a single longitudinal mode. Placing now a two level atom, or in general, a two level system (TLS) into this path, this leads to a resonance effect of absorption and emission. In such a case the photon energy has to match the energy difference of the TLS. Typically this rate of interaction is characterized by the letter  $g$  in literature (see e.g. [Fox06]) or in articles (e.g. [SG08]).

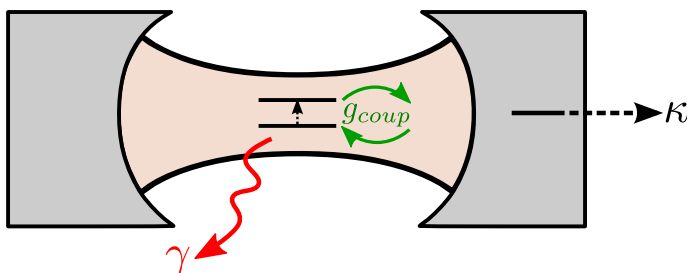


Figure 3.25.: A cavity constructed out of two mirrors (gray), separated by a certain distance. Due to the mirrors, photons (light red) are able to bounce back and forth. A typical photon loss mechanism is e.g. the absorption at the cavity walls or transmission out of the cavity, described by cavity loss rate  $\kappa$ . If a two level system is present in the cavity, the photon is absorbed and re-emitted at rates represented by  $g_{coup}$ . If the re-emission happens into other, non-resonant modes, this leads to further losses described at rates of  $\gamma$ .

In order to avoid confusion with the g-factor ( $g$ ) as used in previous sections, for this thesis the subscript *coup* is used. This factor denotes the coupling rate between the photon and atom. More generally,  $g_{coup}$  is the vacuum Rabi frequency [SG08] or the coupling

constant in the Jaynes-Cummings model [WM08]. Initially, the Rabi model considers the resonant interaction between an atom and a classical field of high intensity, while the Jaynes-Cummings model considers the same phenomenon for quantized light fields with small photon numbers [Fox06].

Besides this interaction or coupling rate, undesired loss processes are also present. For example, the lifetime of the photon in the cavity is determined by the rate  $\kappa$ , whereas the emission of the photon into other, non TLS resonant modes happens at the rate  $\gamma$ . If such processes are at rates higher than the light-atom coupling rate ( $g_{coup} \ll (\kappa, \gamma)$ ), this indicates the regime of weak coupling. For  $g_{coup} \gg (\kappa, \gamma)$  the regime of strong coupling is reached. Usually the regime of strong coupling is preferred, as several cycles of absorption and emission exist before the photon is lost, as needed for reversible exchanged of quantum information [SG08]. The presence of a resonator cavity enhances the probability of coherent oscillations as needed for such reversible processes, whereas spontaneous emission is usually an irreversible process. In a measuring experiment, strong coupling is indicated by the frequency splitting of the main resonance mode as schematically depicted in figure 3.26:

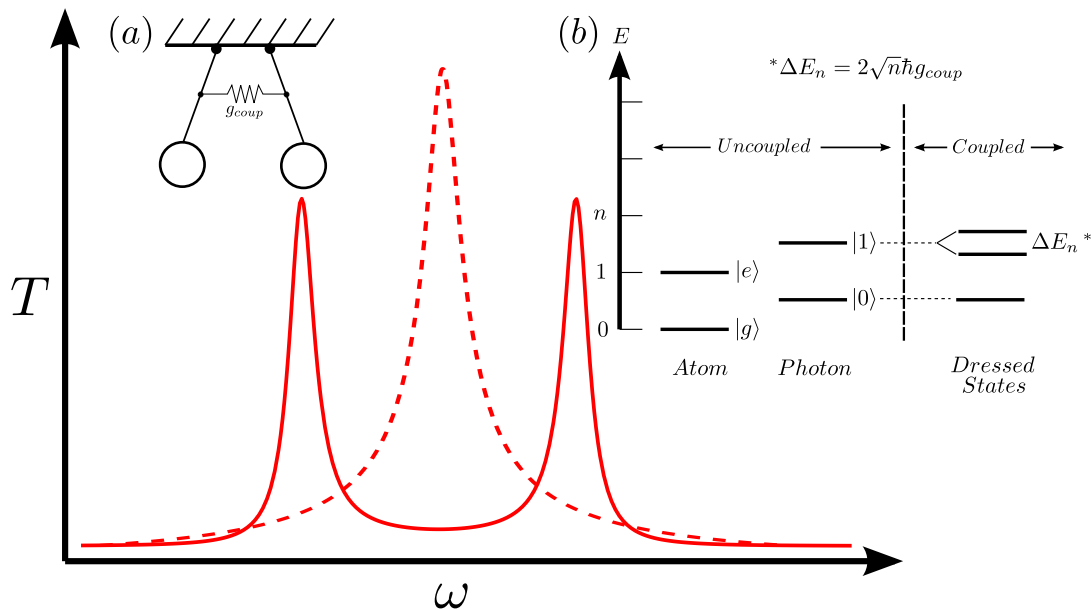


Figure 3.26.: Transmission spectra of an unperturbed or uncoupled resonator (red, dashed). In case of a perturbation indicated as e.g. a coupling of a cavity and a TLS, two resonances (red, solid spectra) are observed (mode splitting). (a) Two masses coupled by a spring would also show a kind of mode splitting (analog example). (b) Jaynes-Cummings representation of a coupled system. The coupling between the atom and a photon or photons leads to the so called dressed states with separation  $\Delta E_n^*$ . (b) taken from [Fox06].

A full quantum mechanical treatment of such a splitting is that of Jaynes and Cummings, using a single quantized mode of radiation field. A bare state of an uncoupled resonator system is considered with the atom in the ground state and no photon in the cavity. This state has an energy of  $(1/2)\hbar\omega$  due to the zero-point energy of the vacuum field. The first excited state is at energy  $(3/2)\hbar\omega$  and corresponds to the states with either the atom in the excited state and no photon in the cavity, or the atom in the ground state and a photon present in the cavity [Fox06]. In the interaction picture the degeneracy is split (vacuum Rabi splitting) by  $2\sqrt{n}\hbar g_{coup}$  ( $n$  = number of photons), now described as dressed states [WM08] (inset (b) of figure 3.26). Due to this splitting two transitions are allowed. Thus, two resonances are observed in the spectrum. An explanation could also be given by the properties of two coupled classical oscillators as depicted in inset (a) of figure 3.26.

As the energy difference of the splitting according to the Jaynes-Cummings model is given by  $\Delta E = \hbar g_{coup}$ , this equals  $g\mu_B B$  (using 3.8). Treating here the interaction with the vacuum magnetic field  $B_{vac}$ , this gives:

$$2 \cdot \int \frac{1}{2\mu_0} B_{vac}^2 dV = \frac{1}{2} \hbar \omega, \quad (3.45)$$

where the energy density of the magnetic field with  $\mu_0$  as the permeability and two times the polarization is integrated over a volume<sup>10</sup>  $V$ . Finally, this is equivalent to the zero point energy. From this equation,  $B_{vac}$  is found to be  $(\mu_0 \hbar \omega / 2V)^{1/2}$ . Now,  $g_{coup}$  is found to be

$$g_{coup} = \frac{g\mu_B}{\hbar} \sqrt{\frac{\mu_0 \hbar \omega}{2V}}. \quad (3.46)$$

Thus, the coupling rate is enhanced by high values of the g-factor, angular frequency  $\omega$  and small volumes  $V$ . More frequently equation 3.46 is given as

$$g_{coup} = \sqrt{\frac{|\vec{\epsilon} \cdot \vec{\mu}_0|^2 \omega}{2\hbar \epsilon_0 V}}, \quad (3.47)$$

with  $\vec{\epsilon}$  as the polarization vector,  $\vec{\mu}_0$  as the transition dipole moment and  $\epsilon_0$  as the permittivity [Kim08]. Instead of using a transition dipole moment in equation 3.46, the representation of equation 3.8 ( $g\mu_B B$ ) was used (see section 3.1.1 for more details). The polarization was set to 2, i.e. the two independent polarizations of the field.

From equation 3.47 it is seen, that the coupling is enhanced by high values of the dipole moment. Electric dipole moments lie typically in the range of atom, molecule or even on Rydberg atom sizes, whereas magnetic moments are typically in the range of the Bohr magneton  $\mu_B$  for the electron spin. For the nuclear spin this is even some order of magnitudes lower.

Relatively small volumes  $V$  are typically achieved in circuit QED, where for example one-dimensional transmission line resonators, or lumped-element resonators are used. Circuit QED is typically associated with microwave photons coupling to superconducting quantum bits or qubits, which act like artificial atoms. Such a qubit (isolated Josephson junction) is typically placed near an antinode of a voltage standing wave and thus coupling to the electric field of e.g. a transmission line. An excitation corresponds to the tunneling of a bound electron pair (Cooper pairs) through the junction, which is comparable to a very large dipole moment (four orders of magnitude greater than that of an electronic transition of a real atom) [SG08].

As such structures can be made using ordinary microelectronic fabrication techniques as already widely used in today's fabrication, this opens new possibilities in engineering small cavity volumes and large dipole moments in order to easily achieve the strong coupling regime.

Besides small volumes and large dipole moments, the coupling can be also enhanced by the number of atoms  $N$  [WM08]. In such a case, equation 3.46 and 3.47 are multiplied by  $\sqrt{N}$ . This is observed due to the collective behavior of a system of  $N$  two-level atoms, which couple to a single mode of the electromagnetic field in a resonator [VMRT03].

<sup>10</sup> Usually the cavity mode volume is used as  $V = \int \sin^2 |U(r)|^2 d^3r$ , with  $U(r)$  being the cavity standing wave mode function [WM08]

Such a description is given by the Tavis-Cummings-Hamiltonian [SRA<sup>+</sup>12]:

$$H_{TC} = \omega a^\dagger a + \frac{1}{2} \sum_{j=1}^N \omega_j \sigma_j^z + \sum_{j=1}^N \left( \mathbf{g}_j \sigma_j^+ a + \text{H.c.} \right), \quad (3.48)$$

where  $\omega$  is the angular frequency of the electromagnetic field,  $\omega_j$  is the level splitting of individual two-level atoms,  $\sigma$ 's are the Pauli matrices and  $a, a^\dagger$  are the annihilation and creation operators of the field, using  $\hbar = 1$ .

The first two terms describe the unperturbed energies of the cavity, where the third term describes the coupling to the cavity with individual strengths  $\mathbf{g}_j$ . The ensemble couples to a mode with the collective coupling strength  $\Omega = \sqrt{\sum_{j=1}^N |\mathbf{g}_j|^2}$ , which for identical  $\mathbf{g}_j$  gives  $\Omega = g_{coup} \sqrt{N}$  [SRA<sup>+</sup>12].

We will complete this section with an estimation of  $g_{coup}$  according to a waveguide resonator filled with a Er:YSO crystal, where our cavity has a diameter of 30 mm and a height of  $\approx 20$  mm, resulting in a volume of  $V = 1.435 \cdot 10^{-5} \text{ m}^3$ . The crystal possesses dimension as found in figure 3.13. The density of the Er:YSO crystal is  $4.44 \text{ g cm}^{-3}$  (www.scientificmaterials.com), for which the calculated number of spins is  $N \approx 2.46 \cdot 10^{16}$ , if using a dilution of 50 ppm erbium. For the coupling of a single spin we used equation 3.46 as:

$$g_{coup} = \frac{g\mu_B}{\hbar_0} \sqrt{\frac{\hbar\omega}{2V\epsilon_0}}. \quad (3.49)$$

Using values of  $c_0 = 3 \cdot 10^8 \text{ m/s}$  as the speed of light in vacuum and the permittivity  $\epsilon_0 = 8.854 \cdot 10^{-12} \text{ F/m}$ , this results in  $g_{coup} \approx 10 \text{ mHz}$ . Further we assumed for the frequency  $f \approx 5.5 \text{ GHz}$  ( $\omega = 2\pi f$ ) and used the g-factor as  $g = 2$ .

The situation changes if multiplying equation 3.49 with  $\sqrt{N}$ , where furthermore we assume a large g-factor in Er:YSO as  $g \approx 14$ . In such a case the coupling strength changes to  $g_{coup} \approx 12 \text{ MHz}$ . This example shows that if using already a 50 ppm doped erbium crystal, the coupling strengths is enhanced by approximately 8 orders of magnitude. Additionally, if using e.g. a 200 ppm crystal, the coupling strength amounts to  $\approx 24 \text{ MHz}$ .



# 4. Characterization and Measurement of Er:YSO filled Waveguide Resonators

---

## 4.1. Experimental Setup

This section will shortly introduce the experimental ESR spectroscopy setup. For the measurements as presented in this thesis, we used a vector network analyzer (VNA) from Agilent (PNA-X N5241A) as the microwave source. The resonator cavity was connected via coaxial cables to the VNA for room temperature measurements. In case of measurements at cryogenic temperatures, a dilution refrigerator system from BlueFors was used. The VNA was then connected via coaxial cables to a cryostat flange. Inside the cryostat, stainless steel transmission lines have been used, where at several temperature stages additional attenuators are used in order to achieve reasonable signal to noise (S/N) ratios.

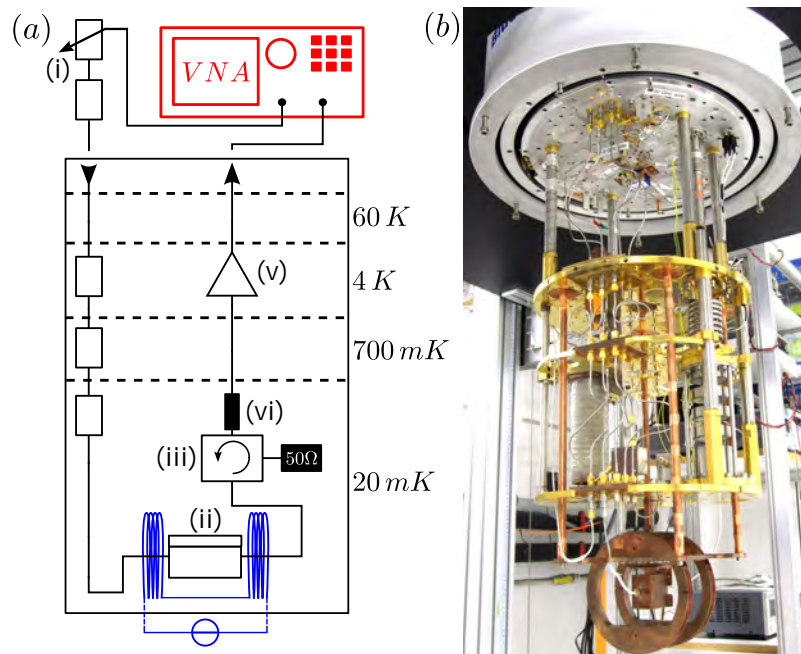


Figure 4.1.: (a) Schematic experimental setup for low temperature measurements. Temperature stages are found on 60 K, 4 K, 700 mK (still) and 20 mK (mixing chamber). Attenuators (small black boxes) are used for S/N adjustments. (i) Adjustable attenuator, (ii) resonator cavity, (iii) circulator, (vi) 3 to 7 GHz bandpass filter, (v) 4 to 20 GHz HEMT. In red color: VNA from Agilent. In blue color: the Helmholtz-Coil connected to a current source. (b) Real picture of the cryostat without temperature shielding.

Figure 4.1 (a) shows schematically the experimental setup as used for low temperature measurements. The real cryostat itself is shown in figure 4.1 (b) without temperature

shielding and vacuum can. As seen from figure 4.1 (a), we used an additional variable attenuator in front of the VNA in order to vary the applied power down to the single photon regime. At the 20 mK stage, the resonator was placed inside a Helmholtz coil (HC), providing static magnetic fields up to  $\approx 280$  mT. A high electron mobility transistor (HEMT) is used at the 4 K stage, amplifying microwaves in the range between  $\approx 4$ -20 GHz. We used additionally a circulator in front of the HEMT, which sends the microwaves from port 1 to port 3. Port 1 of the circulator was used as input and port 2 as output. The reason for the usage of a circulator is the fact, that reflected signals entering port 2 would take the way to port 3, where a  $50 \Omega$  terminating resistor<sup>1</sup> is used to avoid reflections. Furthermore, a band pass filter between the circulator and the amplifier is used, transmitting frequencies from  $\approx 3$ -8 GHz, in order to amplify only the frequency band of interest. Figure 4.2 demonstrates the case where the resonator cavity is placed inside the Helmholtz coil:

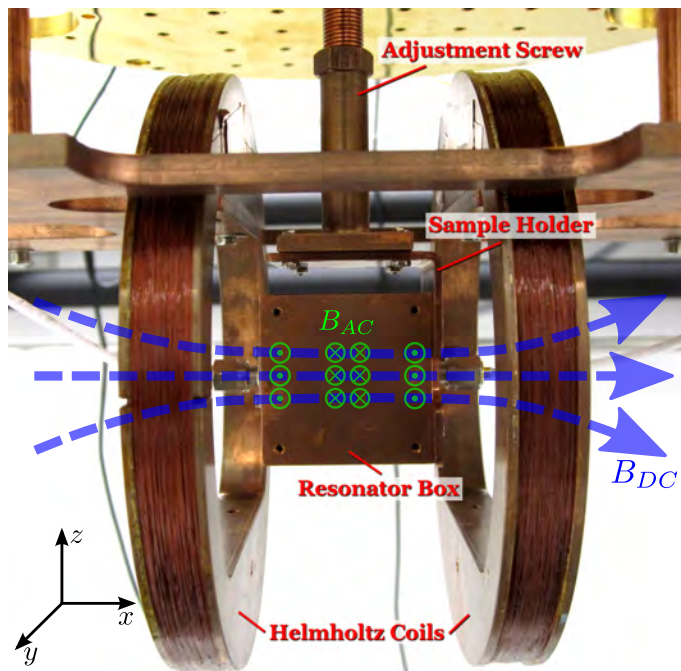


Figure 4.2.: Helmholtz coil with sample holder (copper) and resonator box. In order to place the resonator into the volume of highest density of magnetic fields (schematically indicated by blue arrows [ $B_{DC}$ ]), the position of the z-component is fine adjusted by a top adjustment screw. The x and y positions are predefined by the sample holder. The oscillating magnetic field ( $B_{AC}$ ) of the resonator is schematically indicated by green symbols, where the cross symbol represents the magnetic field pointing into the paper plane and the dot symbol pointing out of plane. The condition  $B_{DC} \perp B_{AC}$  is presented.

In order to align the cavity to the center of highest and most homogeneous magnetic fields (center between both coils), an adjusting screw for the z-axis component (see figure 4.2) was used. The x and y components are already fixed by the cryostat's still stage. The HC itself was mounted at the still stage too, such engineered that the adjusting screw (mounted to the mixing chamber stage) lies in the center of the HC. On the other side, the x and y components are fine adjustable via a cavity sample holder, which was designed in order to support two kinds of cavity resonators.

<sup>1</sup> Typical transmission lines or coaxial cables are such designed to have an input impedance of  $50 \Omega$

## 4.2. Waveguide Resonator Version 1

The first version of a 3D cavity waveguide resonator was designed by Prof. Dr. Pavel Bushev according to a paper published by J. G. Hartnett et al. [HTS<sup>+</sup>05]. The approach was to use initially the published data for a first version design as discussed next.

### 4.2.1. Characteristics and Determination of the Resonant Frequencies

In principal, a waveguide resonator consists out of a copper cube, where the waveguide structure is milled in. Additionally a dielectric material as sapphire is used to scale down the resonant frequencies (see e.g. section 3.3). The final shape and the corresponding dimensions of the first waveguide resonator are presented in figure 4.3.

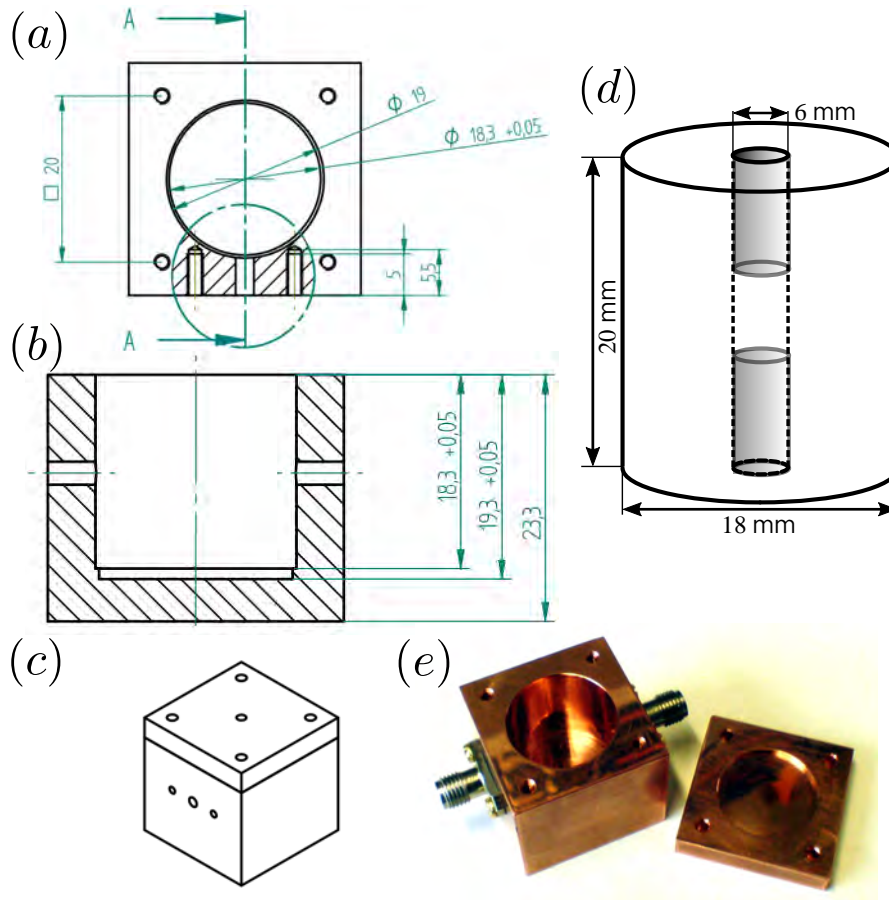


Figure 4.3.: Waveguide resonator version 1 with shop drawings in mm dimensions. (a) Top view, (b) side view, (c) complete box (closed case). (d) Schematic drawing of the sapphire crystal with dimensions and the tefflon plugs (light gray). (e) Real picture of waveguide resonator version 1 with coaxial cable connectors (opened case without sapphire crystal).

The resulting copper box consists out of two parts. The bottom part [figure 4.3, (a,b)] is the box with the waveguide hole, where the upper part is the box cap. The cap is screwed together with the bottom part, forming the desired cylindrical cavity [figure 4.3 (c)]. The bottom part of the copper box additionally owns holes at the side walls, serving as entrance holes for the coaxial cable connectors, in order to couple microwaves into and out of the cavity.

The sapphire crystal is such designed to fit nearly the whole cylindrical cavity volume. Approximately 1 mm space was taken into account between the cylindrical wall and the sapphire crystal in order to avoid stress onto the crystal due to a different thermal expansion coefficient as compared to copper.

Additionally, the sapphire crystal is not a full cylinder, rather owing a tube shape as presented in figure 4.3 (b).

Such opening is needed to place the sample of interest into the center of the cylindrical cavity, where two teflon plugs are used as the sample holder for the erbium doped crystals.

In order to characterize the resonator including the sapphire crystal and the teflon plugs, a transmission spectrum using the VNA was measured:

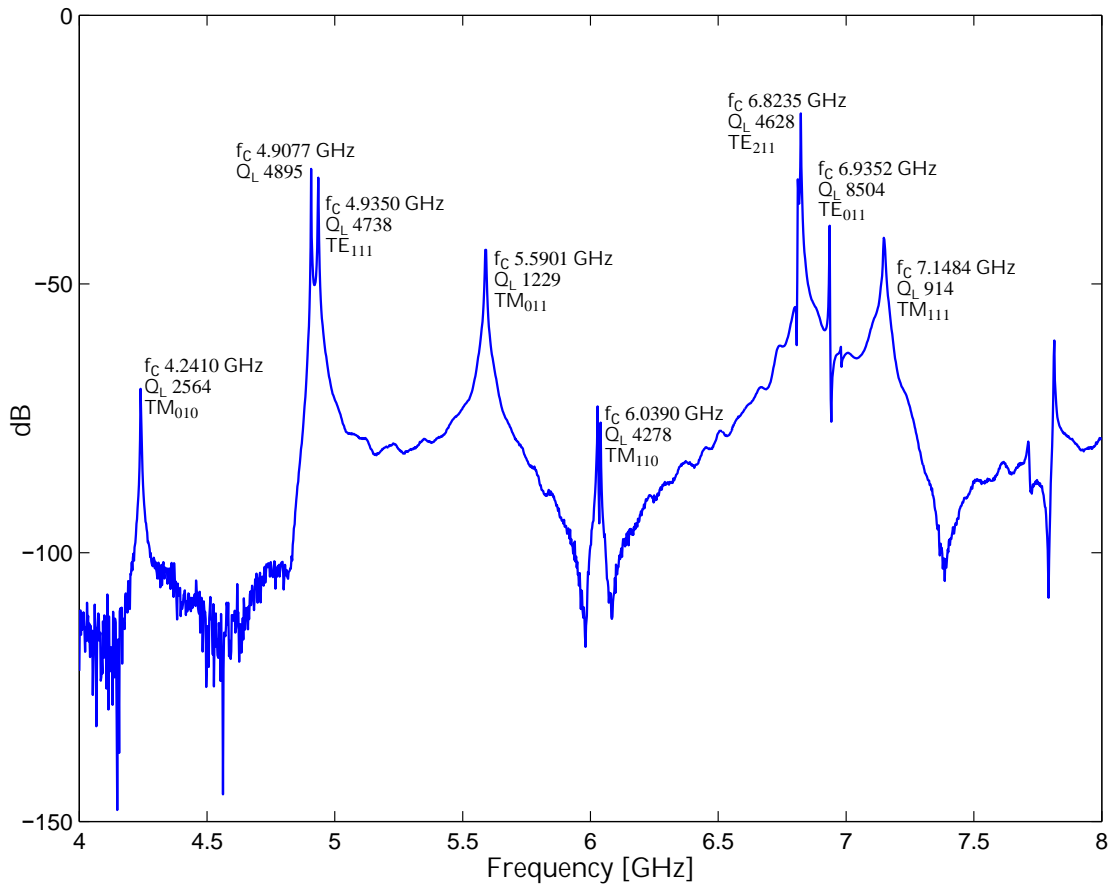


Figure 4.4.: Transmission spectrum of waveguide resonator version 1 measured in decibel (dB) versus frequency from 4 to 8 GHz. The individual resonant frequencies  $f_c$  are extracted using a Lorentz-Function fit, whereas the loaded quality factors  $Q_L$  are calculated according to  $f_c/\Delta f$ . The transverse electric (TE) and transverse magnetic (TM) modes were determined from CST simulations.

Figure 4.4 presents the transmission spectrum of waveguide resonator version 1, measured between 4 and 8 GHz. The center frequency  $f_c$  and the loaded quality factor  $Q_L$  of every transmission peak was determined by separated individual transmission peak measurements.

The scattering matrix data was evaluated using MatLab and OriginLab, fitting the subsequent Lorentz function to the power spectrum ( $|S_{21}|^2$ ):

$$\mathcal{L}(f) = a + \left(\frac{2A}{\pi}\right) \frac{\Delta f}{4(f - f_c)^2 + (\Delta f)^2}. \quad (4.1)$$

The parameters found in equation 4.1 are the offset  $a$ , area  $A$ ,  $\Delta f$  as the full width at half maximum (FWHM) and the center frequency  $f_c$ . More precisely,  $Q_L$  was determined using equation 3.35, where the intrinsic or internal quality factor is  $\approx Q_L$  due to low external coupling (check section 3.3.3 for more details).

In order to localize the  $TE_{011}$  resonant mode, the cavity was modeled with a 3D electromagnetic wave simulation software from CST (Computer Simulation Technology, Microwave Studio).

The center frequency values extracted from CST simulations are summarized together with the center frequency values from the VNA measurements in table 4.1:

Mode No.	$f_c$ CST simulation [GHz]	$f_c$ VNA measurement [GHz]	relative error [%]
01	4.2384	4.2410	+0.06
02	4.8957	4.9077	+0.25
03	4.9016	4.9350	+0.68
04	5.6284	5.5901	-0.68
05	6.0209	6.0278	+0.11
06	6.0237	6.0390	+0.25
07	6.8054	6.8100	+0.07
08	6.8369	6.8235	-0.20
09	6.8677	—	—
10	6.8679	—	—
11	6.9480	6.9352	-0.18

Table 4.1.: Extracted center frequency ( $f_c$ ) values from simulation and measurement of waveguide resonator version 1. The mode number is chosen in ascending order compared to increasing frequency for the simulation case.

Up to this point, table 4.1 only indicates that the measured resonant frequencies coincide very accurately with the simulation, achieving relative errors below 1 %. Furthermore, it is observed that some frequency modes found from simulations have been not measured. Reasons could be degenerate modes or insensitive coupling to such modes.

CST Microwave Studio provides besides the calculated resonant frequencies also the field distribution of the electric and magnetic field of each calculated mode. By analyzing these distributions for every resonant frequency, the  $TE_{011}$  mode was successfully found to resonate at 6.948 GHz (table 4.1, mode number 11). This mode corresponds to the 9<sup>th</sup> transmission peak in figure 4.4.

The field distribution of a  $TE_{011}$  mode as present inside the cavity is shown in figure 4.5 on the next page.

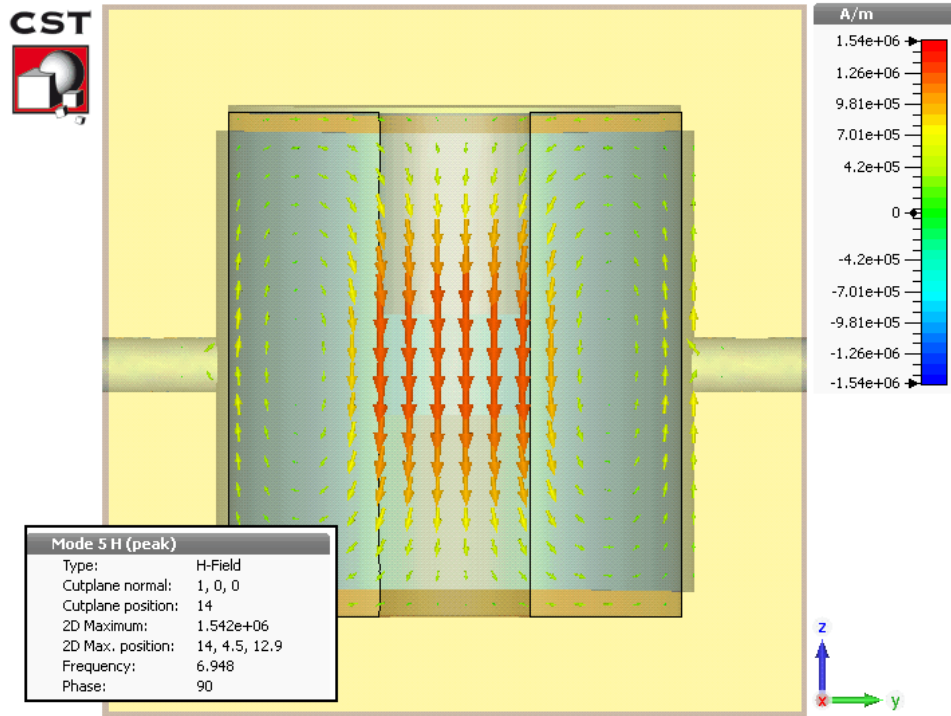


Figure 4.5.: CST Microwave Studio simulation of waveguide resonator version 1 with sapphire crystal and the tefflon plugs, taking into account the anisotropy of the permittivity of sapphire. The  $TE_{011}$  mode is identified by the field distribution of the magnetic field, resonating at 6.948 GHz (see left inset). The field strength is represented by a color bar on the right hand side.

Figure 4.5 shows a cut through the copper box simulation model, filled with sapphire and the tefflon plugs. The model should imitate 1:1 the real structures. The magnetic field distribution is indicated by colored arrows, representing the field strength (see color bar). The magnetic field reaches highest values at the center of the cavity as needed for the experiments. In this case, the arrows are pointing from the top to the bottom for a phase of  $90^\circ$  (see left inset of figure 4.5), whereas for  $270^\circ$  they would point into the opposite direction, indicating the oscillatory behavior of the magnetic field. The  $TE_{011}$  mode behavior can be compared to figure 3.21 of section 3.3.2. The observed side holes of the cavity in figure 4.5 are the entrance holes for the coaxial cable connectors, which could be left empty for the simulation. Finally, the correct frequency of the desired mode is determined by experiment, as discussed in the next section.

#### 4.2.2. ESR Spectroscopy of 200 ppm Doped Er:YSO at mK Temperatures

For ESR spectroscopy at mK temperatures the copper box cavity along with the sample (erbium doped YSO crystal) were installed into the cryostat and probed with a VNA. Thus, if the correct resonating mode is present and if the oscillating magnetic field of such a mode is perpendicular to the applied static magnetic field, transitions should be observed as discussed in chapter 3.1. Moreover, the orientation of the erbium doped crystal according to the static magnetic field should be set correctly. For this purpose we used the diagrams published by Sun et al. [SBTC08] as presented in figure 4.6.

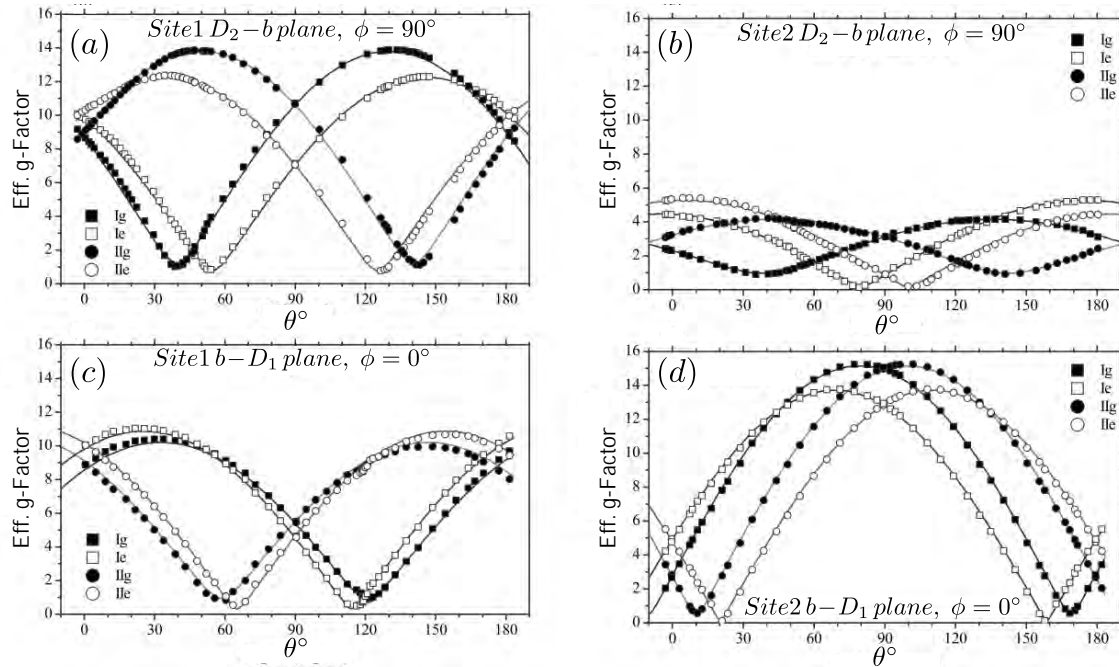


Figure 4.6.: Effective g-factors as function of angle  $\theta$  and the magnetic inequivalent ground (g) and excited (e) states. (a) Site 1 of plane  $D_2$ -b, (b) site 2 of plane  $D_2$ -b, (c) site 1 of plane  $b$ - $D_1$ , (d) site 2 of plane  $b$ - $D_1$ . All graphs taken from [SBTC08].

Figure 4.6 shows the effective g-factors on the vertical axis as a function of the crystal orientation with respect to an applied static magnetic field, indicated by angle  $\theta$ . Figure 4.6 (a) and (c) are representing site 1 for the planes  $D_2$ -b and  $b$ - $D_1$ , respectively. Figure 4.6 (b) and (d) are used for site 2. Due to magnetic inequivalence, four curves are plotted for each figure (a)-(d). On mK temperatures effectively the lowest energy level is populated and transitions appear thus only at microwave frequencies for the ground state, indicated by black squares (IIg) and circles (Ig). Therefore, at least four transitions should be observed according to site 1 and 2.

For the first measurement we decided to take an angle of  $\approx 10^\circ$   $\theta$  for the  $D_2$ -b plane. In order to resolve all 4 transitions, angles close to  $0^\circ$ ,  $90^\circ$  and obviously  $180^\circ$  should be avoided, as in these regions the g-factors merge. According to the g-factor equation 3.9, the lowest g-value observed would be  $\approx 2$ , if expecting the  $TE_{011}$  mode resonating at  $\approx 7$  GHz. Furthermore, lower g-factors in case of the static magnetic field should lead to higher g-factors for the oscillating magnetic field, as described by Probst et al. [PRW<sup>+</sup>13]. In order to achieve high coupling rates, high g-factors of the oscillating field are desired, as discussed in section 3.4.

For measurements we increased and measured the current through the Helmholtz coil, which is proportional to the magnetic field present at the resonator. For every incremental increase of the magnetic field, the complete transmission signal of the resonator is recorded using the VNA. The resulting ESR spectrum is thus the applied static magnetic field versus the transmission signal of the resonator (frequency). At values of the magnetic field matching the magnetic resonance condition, transitions are induced, indicated by a change of the resonators Q-factor and a dispersive change of the resonant frequency (compare e.g. figure 3.19 of section 3.3.1). In order to see such changes at the ESR spectra, the amplitude of the transmission signal is color coded. ESR spectra as observed in experiments are presented in figure 4.7 on the next page.

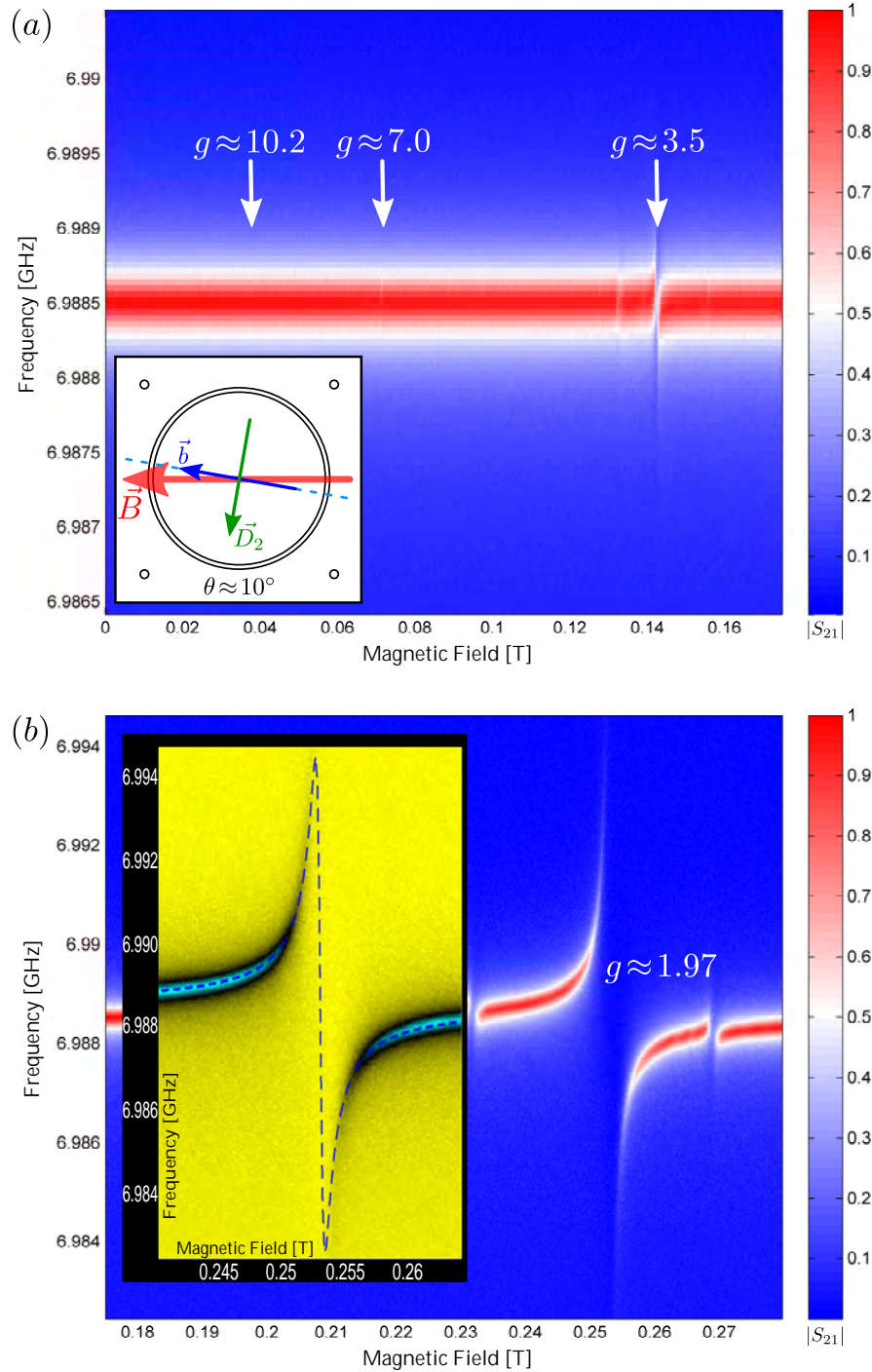


Figure 4.7.: ESR spectra measured as the applied static magnetic field from the Helmholtz coil versus the transmission signal of the resonator (frequency and color coded amplitude). (a) Measured transitions between 0 and 175 mT, where one transition with  $g$ -factor of  $\approx 3.5$  is clearly observed. Two weak transitions around the main one are hyperfine transitions. The other two transitions indicated by arrows are rather harder to determine immediately. The white inset (a) presents the copper cavity from top view, showing schematically the orientation of the static magnetic field  $\vec{B}$  (red) with respect to the crystal coordinates  $\vec{b}$  and  $\vec{D}_2$  (blue and green). The crystal is rotated by 10 degree with respect to the magnetic field axis. (b) Measured transitions between 175 mT and 280 mT. The final transition with  $g$ -factor of  $\approx 1.97$  is clearly observed. The transitions distributed around the main one are hyperfine transitions. The yellow inset is the color-inverted main transition with fitting (dashed curve) according to equation 4.2.

Figure 4.7 (a) and (b) show the transmission signal of the resonator along the vertical axis, where the largest amplitude ( $|S_{21}|$ ) of the transmission is indicated in red, dropping to the sides in an almost Lorentzian fashion. The lowest amplitude is described in colors of blue, where the normalized amplitude is represented by the color bar on the right side.

The doping concentration of the used Er:YSO crystal was 200 ppm. We probed several resonances around 7 GHz where only the resonance at 6.9885 GHz showed transitions as presented in the figure 4.7. The resonance frequency of 6.9885 GHz is quite close to the expected resonance frequency of 6.948 GHz obtained from simulations. The difference of  $\approx 41$  MHz is explained by considering the temperature dependent change of the dielectric permittivity ( $\epsilon_r$ ) of the sapphire material. If using the temperature dependent  $\epsilon_r$  equation of R. C. Taber and C. A. Flory published 1995 [TF85], an  $\epsilon_r$  value of 11.58 (parallel to the crystal axis) is calculated for a temperature of 293.15 K. At 30 mK this value amounts to 11.35. As the frequency scales proportional to  $1/\sqrt{\epsilon_r}$  (see e.g. equation 3.41), there has to be an increase of  $\approx 3$  %. Furthermore, if taking the anisotropy into account, i.e.  $\epsilon_r$  perpendicular to the crystal axis, a change of roughly 6 % is possible, which seems to be here the case.

The g-factors found in figure 4.7 (a) and (b) are extracted by using equation 3.9. All measured g-factor values are also found in figure 4.6 (a) and (b) for an angle  $\theta$  of  $\approx 10$  degree. The smaller transitions observed around the main transition are hyperfine transitions. In order to determine the coupling strength  $g_{coup}$  and spin linewidth  $\Gamma$ , we used the subsequent equation which is describing the observed dispersive shift [Poo67]:

$$\omega = \omega_0 + \frac{g_{coup}^2(\omega_0 - \gamma_{gyr}B)}{(\omega_0 - \gamma_{gyr}B)^2 + \Gamma^2}. \quad (4.2)$$

The yellow colored inset (color inverted picture of the transition) in figure 4.7 (b) shows the fit (dashed line) to the data using equation 4.2. From the fit we found the values of  $g_{coup}$  to be  $11.0 \pm 0.1$  MHz and that of  $\Gamma = 10.4 \pm 0.3$  MHz. Parameter  $B$  in equation 4.2 is the magnetic field and  $\gamma_{gyr}$  is the gyromagnetic ratio.

Unfortunately no strong coupling (no anti-crossing) was observed during the measurements. In order to enhance  $g_{coup}$ , higher values of the oscillating (AC) g-factor are needed, which on the other hand require lower DC g-factors as measured for the static magnetic field. For the measurements as presented in figure 4.7, the lowest g-factor was reached for a value of  $\approx 1.97$ . From publications of Sun et al. [SBTC08] and Probst et al. [PRW<sup>+</sup>13], lower g-factors down to  $\approx 1.4$  could be reached. In order to measure lower g-factors in our experiments, even a new Helmholtz coil is needed, providing higher magnetic fields, or a new cavity with lower resonating TE<sub>011</sub> mode is required. Consequently we decided to design a new waveguide resonator as discussed in the next section.

### 4.3. Waveguide Resonator Version 2

Recapitulating section 4.2 shortly, the required TE<sub>011</sub> mode was successfully determined via simulations. Additionally, measurements with a 200 ppm Er:YSO crystal using this mode showed transitions on certain magnetic fields, as anticipated. It was not possible to reach the strong coupling regime using the waveguide resonator version 1 in combination with the available Helmholtz coil. In order to reach lower values of the g-factor, a new cavity with lower resonating TE<sub>011</sub> mode is required, which is deducible e.g. from equation 3.9 of section 3.1.

### 4.3.1. Design and Characterization

For the new waveguide resonator version 2 we decided to use the same approach as for version 1. In order to shift down the resonant  $TE_{011}$  mode to lower frequencies, the cavity dimensions have to be increased. Other possibilities would be for example the usage of a higher valued dielectric material. We decide to stay with the same sapphire dielectric as used for version 1 as such a dielectric material possesses an adequate loss tangent at cryogenic temperatures [KDT<sup>+</sup>99]. As using exactly the same sapphire crystal for version 2, the diameter length of the cavity is consequently fixed. Thus, only the radius  $a$  has to be adjusted. In this case it is helpful to use a so called mode chart:

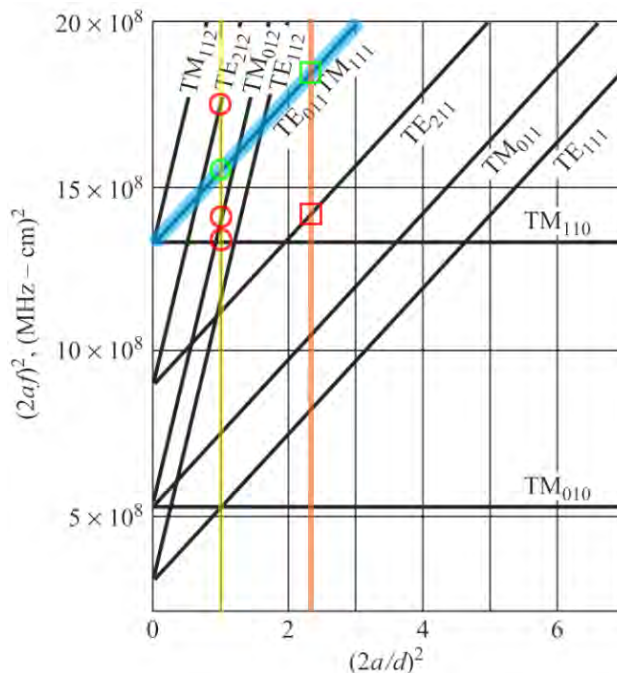


Figure 4.8.: Typical mode chart for a cylindrical cavity resonator presenting the mode distribution for certain ratios of the radius  $a$  and diameter length  $d$ . The vertical axis represents the frequency progression. The ratio according to waveguide resonator version 1 is mark in yellow, whereas orange is used for version 2. The  $TE_{011}$  mode is marked in light blue. Intersection points for version 1 and 2 among the  $TE_{011}$  mode are presented via a green circle and a green square, respectively. Neighboring modes are indicated with red circles and a red square. Figure taken from [Poz11]

From figure 4.8 the mode distribution according to the cylindrical cavity dimensions  $(2a/d)^2$  is deducible. Such a chart represents the case of an air filled cavity and can be used in our case as a first approach to determine a ratio of the radius  $a$  and diameter length  $d$ . In case of a dielectric filled cavity, only the values presented on the vertical axis in terms of  $(2af)^2$  would change, whereas the mode distribution according to the horizontal axis would stay the same.

As we are faced with a tube shaped dielectric sapphire material with space between the cavity walls and the dielectric, our cavity is rather a mixture of partially filled with air (or vacuum) and  $\epsilon_r$  material. Therefore, we use such a chart only as an approach to estimate the radius and length.

However, as the squared ratio of  $2a/d$  for the waveguide resonator version 1 was  $\approx 1$ , several other modes are found in the vicinity of the  $TE_{011}$  mode, indicated via red circles in figure 4.8. The green circle indicates the  $TE_{011}$  mode, degenerate with mode  $TM_{111}$

(both marked in light blue). A degeneracy of both mentioned modes is not necessarily given for shapes like used in our case and is rather determined from simulations. The ratio of  $\approx 1$  is marked in yellow color. From the chart we find three modes close to the  $TE_{011}$ , being here the  $TM_{110}$ ,  $TM_{012}$  and  $TE_{212}$  mode.

If comparing the measurement of the mode distribution of resonator version 1 at room temperature (figure 4.4), three distinct resonant modes are found around the  $TE_{011}$  mode, which resonates at  $\approx 6.94$  GHz. The spacing between this mode and the next lower mode is  $\approx 120$  MHz, whereas for the next higher one we calculate  $\approx 210$  MHz. Such neighboring modes could disturb the preferred mode and also the emission of the resonant photon into these other modes is maybe more likely. Thus, in order to increase the mode spacing, it is preferred to follow the light blue line in figure 4.8 to higher ratios of  $2(a/d)^2$ . In such a case the spacing for the  $TE_{011}$  mode with respect to neighboring modes increases simultaneously.

The ratio of  $2(a/d)^2$  for version 2, which is marked in orange in figure 4.8, shows the  $TE_{011}$  mode at position marked with a green square. The next lower mode is marked via a red square, whereas the next higher mode is not observable in figure 4.8. In our case, the exact ratio of  $2(a/d)^2$  is additionally determined from figure 4.9, representing a quality factor chart:

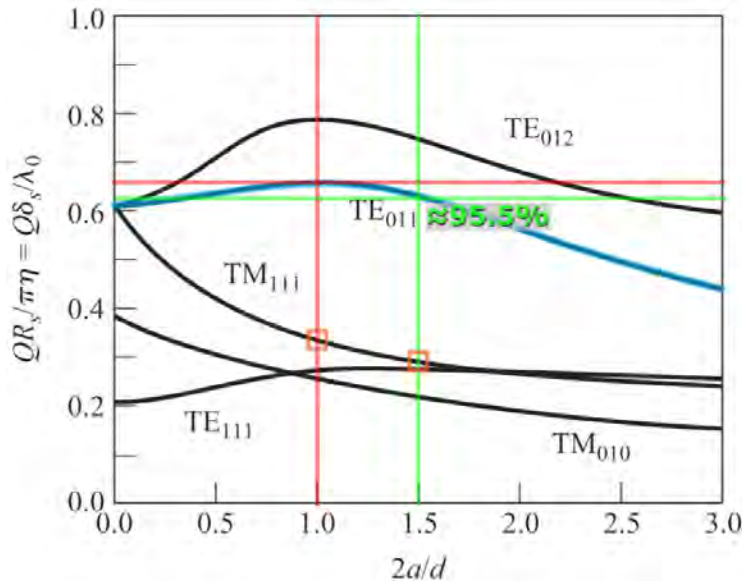


Figure 4.9.: Typical Q-factor chart for a cylindrical cavity resonator presenting the normalized quality factors for certain resonant modes according to the cavities dimensions in ratios of  $2a/d$  with the radius  $a$  and diameter length  $d$ . The prefactors of Q are the surface resistivity  $R_S$  and the wave impedance  $\eta$  or the skin depth  $\delta_S$  and wave length  $\lambda_0$ . The ratio and normalized Q-factor of waveguide resonator version 1 is marked with red lines, whereas for waveguide resonator version 2 green lines are used. Intersections of the degenerate  $TM_{111}$  mode are marked in orange squares. Figure taken from [Poz11]

The radius and length are represented at the horizontal axis in figure 4.9, whereas a normalized, pure geometrical quality factor is found on the vertical axis. The prefactors of Q are the surface resistivity  $R_S$  and the wave impedance  $\eta$  or the skin depth  $\delta_S$  and wave length  $\lambda_0$ .

The so called Q-Chart shows the mode depended quality factor according to ratios of the cavity dimension. In this case the ratio of  $2a/d$  for waveguide resonator version 1 is marked in red (vertical), whereas the highest reachable value of the normalized Q for the  $TE_{011}$

mode is also marked in red (horizontal). This also indicates that for dimensional ratios of  $\approx 1$  the highest Q-value is reached. In case of the degenerate  $\text{TM}_{111}$  mode, rather lower values are found, marked via orange squares.

In order to get reasonable quality factors for waveguide resonator version 2, we decide to take a ratio of 1.5, which would be just  $\approx 4.5\%$  less as compared to version 1, i.e. reaching  $\approx 95.5\%$  of the previous value. For a ratio of 1.5, the ratio according to figure 4.8 would be 2.25. As the diameter length  $d$  is fixed, the radius  $a = (3/4)d$  or just 75% of the length.

Using this value for the radius, a new resonator model was designed with CST Microwave Studio in order to exactly determine the  $\text{TE}_{011}$  mode and to check if a wider neighboring mode spacing is present, as expected. Due to the fixed value of the diameter, definitely an increase of the radius  $a$  will lead to a lower resonating  $\text{TE}_{011}$  mode, expecting the resonance below 6 GHz.

From simulations of waveguide resonator version 2, the  $\text{TE}_{011}$  mode was identified to resonate at  $\approx 5.56$  GHz, where the next lower mode resonates at  $\approx 4.68$  GHz and the next higher one at  $\approx 6.23$  GHz. Thus obtaining now a spacing of  $\approx 880$  MHz and  $\approx 660$  MHz to the next neighboring modes. Therefore, the mode spacing was successfully increased by a factor of  $\approx 4.7$  on average, whereas the main resonance of the  $\text{TE}_{011}$  mode was decreased by  $\approx 1.5$  GHz. The field distribution of the magnetic and electric field of the new waveguide resonator version 2 are presented in figure 4.10:

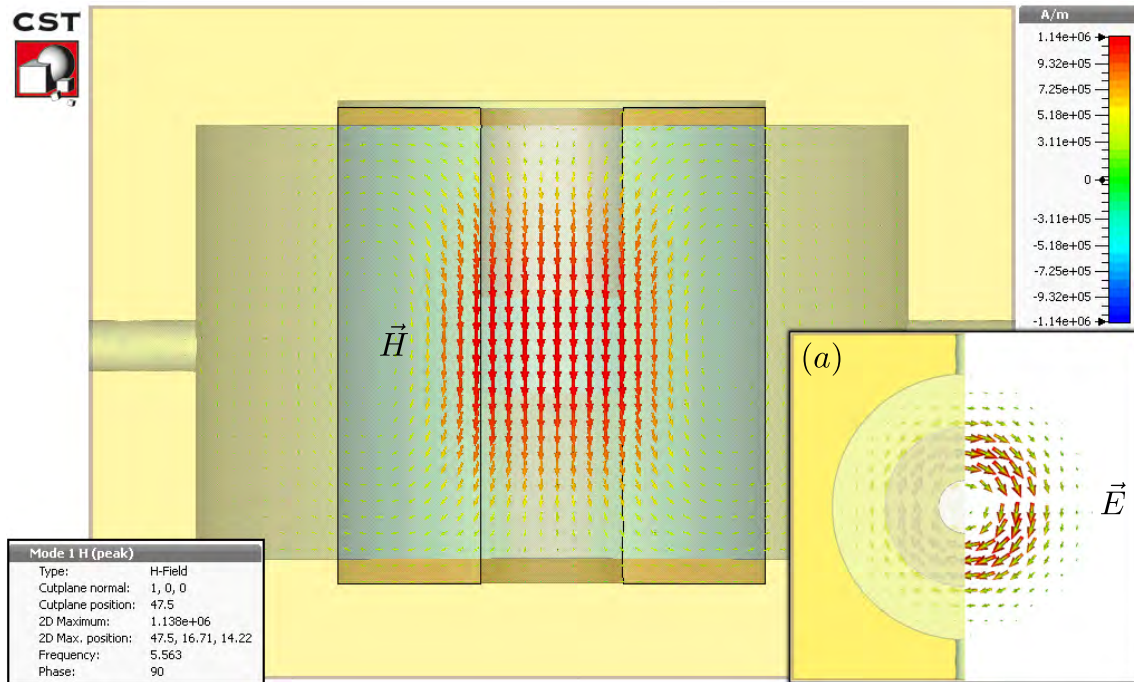


Figure 4.10.: CST Microwave Studio simulation of waveguide resonator version 2 with dielectric sapphire material and teflon plugs. The figure shows a cut through the copper box model where the magnetic field direction and strength of the  $\text{TE}_{011}$  mode are observable, indicated by arrows. The color bar on the right hand side represents the field strength of the magnetic field  $\vec{H}$ . The inset on the left shows a resonant frequency of 5.563 GHz, whereas inset (a) presents the top view of the resonator, showing the electric field  $\vec{E}$ . Again only the half of the copper box is displayed in order to see the field distribution.

The  $\text{TE}_{011}$  behavior of the magnetic field is clearly seen from figure 4.10. The length of the sapphire crystal was kept the same, whereas the larger radius is clearly noticeable if comparing with version 1.

Furthermore, the top and bottom part of the cavity possesses notches in order to keep the sapphire crystal in position if rotating the complete resonator box by 90 degrees. Such notches should not disturb the  $TE_{011}$  mode shape, as the current oscillations for this mode only appear to the axial ( $z$ ) and azimuthal ( $\phi$ ) direction.

It is seen from the left inset of figure 4.10 that this mode is resonating at 5.563 GHz. If furthermore comparing the color intensity representing the field strength at the center of the cavity, values between  $9.3 \cdot 10^5$  A/m and  $1.1 \cdot 10^6$  A/m are observed. Comparing this values with version 1, the loss of magnetic field strength in the teflon free region is rather small as similar values between  $9.8 \cdot 10^5$  A/m and  $1.3 \cdot 10^6$  A/m are found.

We expected even higher losses due to the increased volume, which seems not to be the case. This effect is explained by the electrical field distribution of the  $TE_{011}$  mode, found as inset (a) in figure 4.10 (top view). The electrical fields are mainly confined in the dielectric sapphire material which also leads to high magnetic fields in its vicinity or the center of the cavity according to the  $TE_{011}$  mode behavior.

We used the waveguide resonator model from the simulation as blueprint for the physically real version. This time oxygen free copper was used as material, in order to have a better electrical conductivity ( $\sigma$ ) and thus a higher Q-factor.

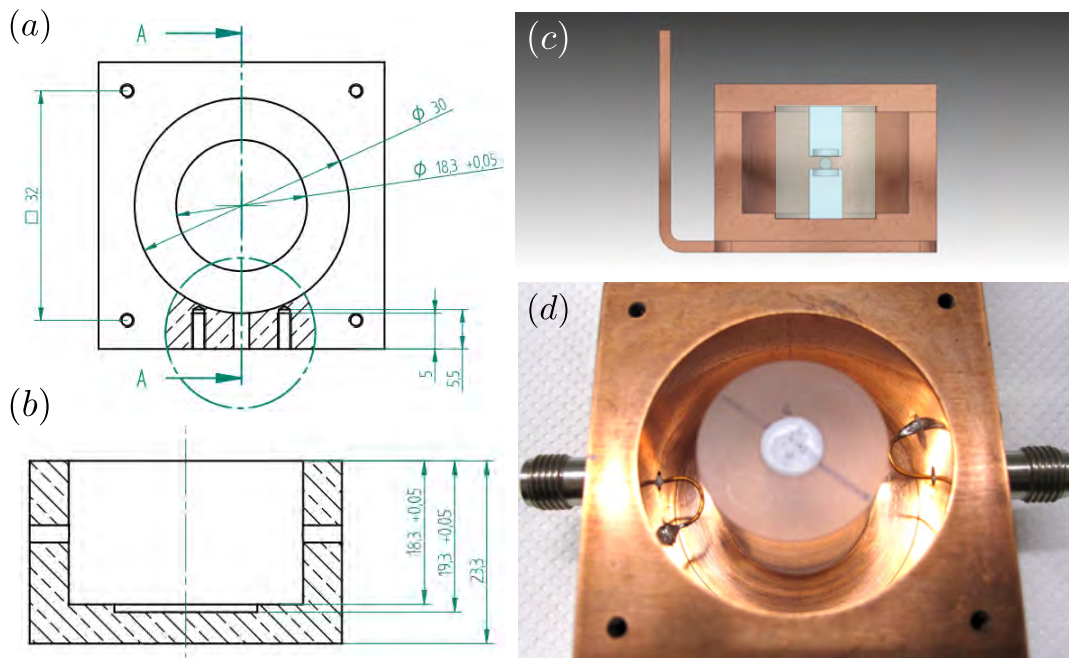


Figure 4.11.: Waveguide resonator version 2. Shop drawings with dimensions in mm: (a) top view, (b) side view. (c) Side cut of the resonator box (closed case), mounted onto the sample holder with view at the sapphire crystal and the teflon plugs. (d) Real picture of the resonator (opened case) with sapphire crystal inside. At the side the two coaxial cable connectors are visible, which are highly coupled to the resonator indicated via the big coupling loops grounded to the cavity walls (inside of the cavity).

Blueprint images of the top view (a) and the lateral view (b) are presented in figure 4.11 for the sake of completeness (shop drawings with dimensions in mm). Figure 4.11 (c) shows an image of the waveguide resonator version 2 mounted onto the sample holder as a cut through the side, where the positions of the sapphire crystal and the teflon plugs are visible. The real image of the resonator is shown in figure 4.11 (d).

In order to proof the simulated values from CST Microwave Studio simulations, a transmission spectrum was measured between 4 and 8 GHz. We used the same coaxial cable

connectors with identical coupling as for measurements using waveguide resonator version 1. We obtained the following transmission spectrum for waveguide resonator version 2:

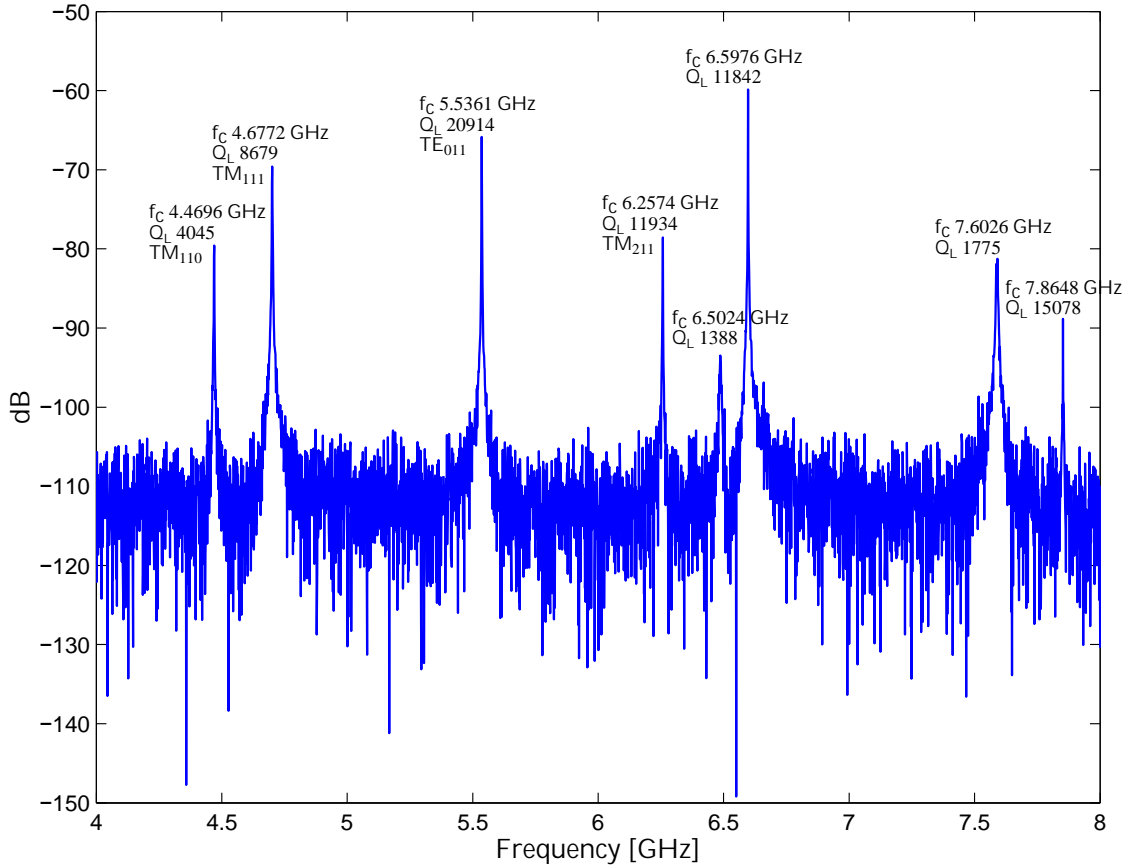


Figure 4.12.: Transmission spectrum of waveguide resonator version 2 measured in decibel (dB) over frequency from 4 to 8 GHz. The individual resonant frequencies  $f_c$  are extracted using a Lorentz-Function fit, whereas the loaded quality factors  $Q_L$  are calculated according to  $f_c/\Delta f$ , using again the Lorentz fit values. The transverse electric (TE) and transverse magnetic (TM) modes between 4 and 6.3 GHz were determined from CST simulations.

In figure 4.12 the individual transmission peaks are presented with its center resonant frequencies  $f_c$  and the loaded quality factors  $Q_L$ , extracted from individual transmission peak measurements and fits as it was done for version 1.

The wide mode spacing between the TE<sub>011</sub> mode located at 5.5361 GHz and the neighboring modes is clearly observed.

It is also interesting to mention that most of the resonances possess high quality factors, which is mainly due to the usage of the oxygen free copper. Especially the quality factor of the TE<sub>011</sub> mode at 5.5361 GHz was measured with a value of 20914.

A similar result is also calculated theoretically if using a conductivity  $\sigma$  of  $5.96 \cdot 10^7$  S/m at room temperature, being  $Q_i \approx 20775$ . For the sake of completeness, the measured resonances are again compared with the simulated values and are summarized in table 4.2 on the next page.

Mode No.	$f_c$ CST simulation [GHz]	$f_c$ VNA measurement [GHz]	relative error [%]
01	2.8384	2.8386	+0.01
02	4.4486	—	—
03	4.4490	4.4696	+0.46
04	4.6785	4.6729	-0.12
05	4.6788	4.6772	-0.03
06	5.5626	5.5361	-0.48
07	6.2253	—	—
08	6.2260	6.2574	+0.50
09	6.5162	6.4870	-0.45
10	6.5508	6.5024	-0.74
11	6.5512	—	—
12	6.6221	6.5976	-0.37
13	6.6226	—	—
14	7.2872	—	—
15	7.6120	7.6026	-0.12
16	7.6192	—	—
17	7.7756	—	—
18	7.7765	7.8648	+1.12

Table 4.2.: Extracted center frequencies from simulation and measurement of waveguide resonator version 2. The mode number is chosen in ascending order compared to increasing frequency for the simulation case. Values not observed from measurement, but present in simulations are indicated via '—'. These are sometimes just close spaced resonances, maybe not resolvable or degenerate in measurement.

From table 4.2 we see that the simulated frequency results are comparable to the measurements within a relative error below or close to 1 %. Values not found for measurements are mostly due to degenerate frequencies or are not resolvable with the used measurement setup. As the simulations fit reasonable to the measurements at room temperature, we will use the resonance frequency at 5.5361 GHz (TE<sub>011</sub> mode) to probe erbium doped crystals at mK temperatures.

#### 4.3.2. ESR Spectroscopy of 200 ppm Doped Er:YSO at mK Temperatures

From previous considerations discussed in the last sections of this chapter, we decide to probe again the same crystal as used for the measurements with waveguide resonator version 1 (concentration 200 ppm, orientation  $\theta \approx 10^\circ$ ), in order to compare the results observed with resonator version 1 and version 2. As expected, again we observed four transitions with nearly same g-factors as it should be the case for  $\theta = 10^\circ$ , but this time the transitions are shifted towards lower magnetic field values. This is not surprising as the resonance frequency of the TE<sub>011</sub> mode was reduced from  $\approx 7$  GHz to  $\approx 5.5$  GHz for version 2. Probing the crystal also on other resonances showed no transitions. Transitions have been only observed for the 5.5 GHz resonance, clarifying this resonance as the expected TE<sub>011</sub> mode.

Furthermore, the quality factor of this resonance was determined with a value of  $\approx 72300$  at  $\approx 25$  mK ( $Q_L \approx Q_i$  for low external coupling). The center frequency was determined with  $f_c = 5.5784$  GHz and a bandwidth of  $\Delta f \approx 77$  kHz. Fitting equation 4.2 to the 3<sup>rd</sup> observed transition, a coupling strength of  $g_{coup} = 2.0 \pm 0.1$  MHz and  $\Gamma$  with  $10.6 \pm 0.2$  MHz were extracted (figure 4.13).

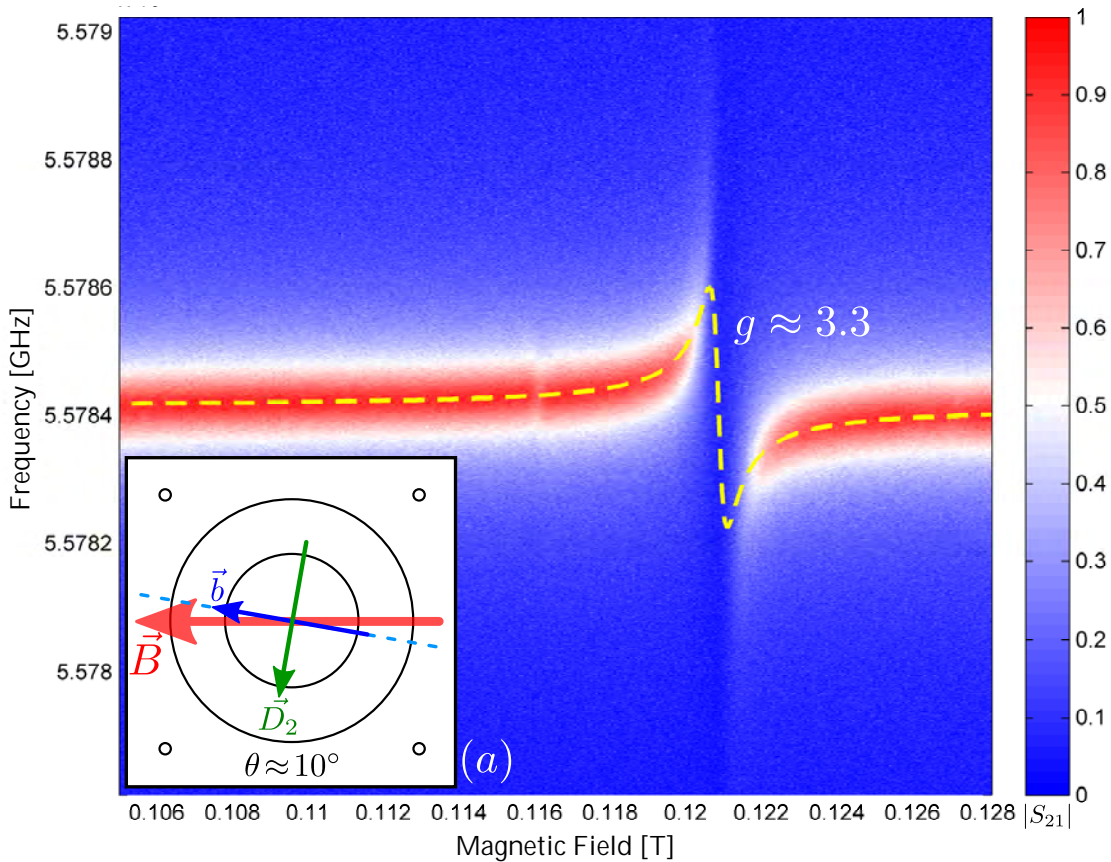


Figure 4.13.: ESR spectrum of the first measurement using waveguide resonator version 2 with 200 ppm Er:YSO crystal. The 3<sup>rd</sup> transition with a g-factor of  $\approx 3.3$  is observed with a yellow, dashed fit according to equation 4.2. (a) Top view of the copper cavity to schematically show the arrangement of the static magnetic field  $\vec{B}$  (red) with respect to the crystal axes  $\vec{b}$  (blue) and  $\vec{D}_2$  (green).  $\vec{b}$  is rotated by 10 degree with respect to  $\vec{B}$ .

Comparing now the coupling strength  $g_{coup}$  of resonator version 1 and version 2, the coupling strength dropped from  $\approx 11$  MHz to  $\approx 2$  MHz for version 2. The value for the spin linewidth  $\Gamma$  did not change significantly and was measured for both to be  $\approx 10.6$  MHz on average. We assume that such a drop of the coupling strength was mainly given by the relatively high quality factor of resonator version 2, which was measured with  $\approx 72300$  at  $\approx 25$  mK. In comparison, the quality factor of resonator version 1 was determined with a value of  $\approx 20500$ , i.e.  $\approx 3.5$  times lower.

#### 4.3.3. ESR Spectroscopy of 50 ppm Doped Er:YSO at mK Temperatures

We assume that the resulting linewidth or bandwidth of waveguide resonator version 2 is too narrow ( $\approx 76$  kHz) and therefore getting only resonant with a fraction of the available spins of the complete spin ensemble.

From other measurements like e.g. Probst et al. [PRW<sup>+</sup>13] it was shown, that rather a lower quality factor and thus a broader resonator linewidth lead to better coupling values, as the distribution of available spins ranges somewhere between 5 MHz and 30 MHz for Er:YSO.

Due to high magnetic anisotropy of the erbium doped crystal, most of the precessing magnetic moments are distributed around the overall Larmor frequency and are thus broadened in frequency. If comparing the linewidth of both resonators, which was found to be  $\approx 340$  kHz for version 1, nearly a factor of  $\approx 4.5$  makes the difference. The same factor is also approximately found for both measured coupling strengths. Therefore, we assume that a higher external cavity coupling would enhance the coupling strength to the spin ensemble.

To check this assumption, we decide to increase the external coupling to the waveguide resonator version 2 as schematically presented in section 3.3.3 about two-port networks and external coupling [figure 3.24 (b)]. Empirically we varied the area enclosed by the probing loops in order to achieve a low quality factor and thus a broader linewidth  $\Delta f$ .

The final version of a higher external coupled resonator is shown in figure 4.14 in combination with the transmitted resonance and a Lorentz fit:

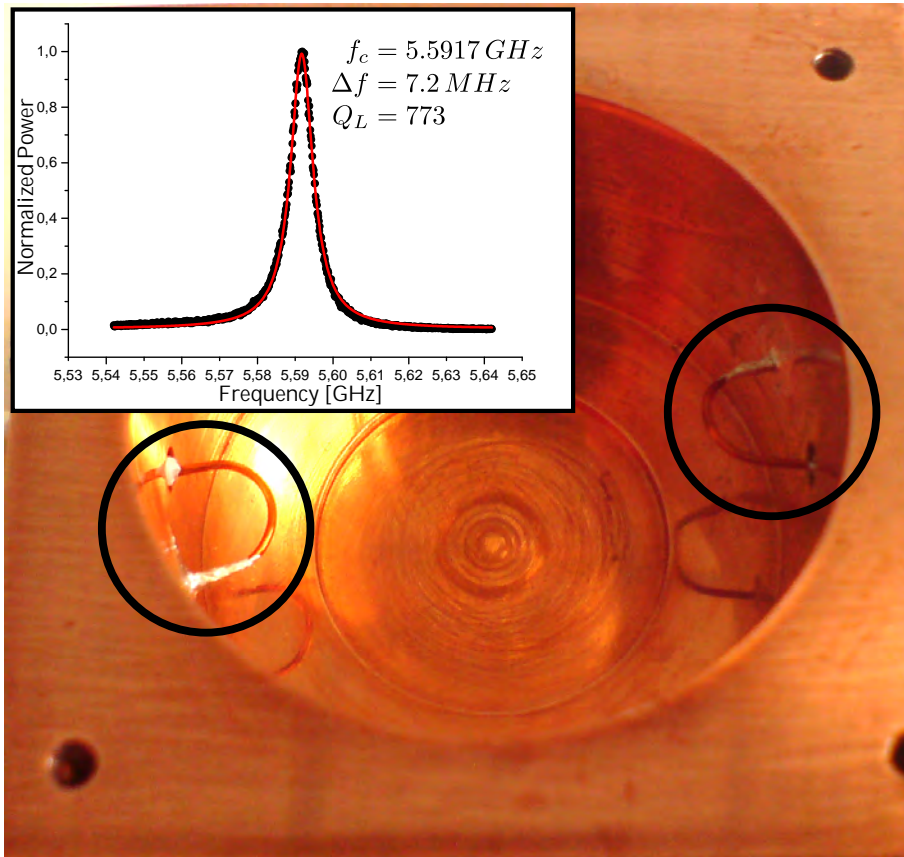


Figure 4.14.: Waveguide resonator version 2 with coupling loops (indicated by black circles), grounded to the cavity walls via silver. The area enclosed by such loops determines the coupling strength. Due to higher coupling, the loaded quality factor could be reduced from  $\approx 20900$  to 773, and thus also the bandwidth of the resonance. The inset presents the measured transmission signal of the TE<sub>011</sub> resonance (black), fitted to a Lorentzian function (red). The bandwidth of 7.2 MHz was determined from the fit measured at cryogenic temperatures.

Figure 4.14 shows the waveguide resonator version 2 without cap and the sapphire crystal in order to see the coupling loops made out of copper. The external coupling to the cavity is enhanced by increasing the area enclosed by such loops. The loops form a circuit with the coaxial cable connectors, grounded via silver to the cavity wall as observed in figure 4.14.

Measurements at cryogenic temperatures showed a significant drop of the loaded quality factor, determined with a value of 773 from a Lorentz fit (see inset of figure 4.14) and thus now possessing a bandwidth of 7.2 MHz. The internal quality factor was determined from equation 3.43.

The coupling coefficient of  $2\kappa$  was determined at room temperature to be  $\approx 3.3$  by using short and equal coaxial cables of same length connected from the VNA directly to the resonator cavity. Thus, the attenuation and other disturbing effects regarding the cables can be neglected. Furthermore, an electrical delay is used to compensate for phase differences.

The external coupling properties ( $Q_e$ ) are purely determined by its geometry, which does not change significantly (due to symmetry consideration) at cryogenic temperatures. From  $Q_L$  at cryogenic temperatures and  $Q_e \approx 1030$  at room temperature measurements,  $Q_i$  was determined to be  $\approx 10700$  using equation 3.44.

For this calculation the factor  $f_{Q_i}$  of  $\approx 3.46$  was determined from the low coupling measurements of  $Q_L \approx Q_i$  at room and cryogenic temperatures. Such factor is the ratio of  $Q_L$  at a cryogenic temperature and room temperature, compensating for the larger values of  $\sigma$  at low temperatures.

Low temperature measurements with the higher externally coupled cavity were performed using a lower doped Er:YSO crystal with equal crystal axes, containing 50 ppm erbium. A higher diluted crystal should in principle reduce the spin linewidth  $\Gamma$ , as influences of neighboring local magnetic fields are reduced and thus leading to less inhomogeneous broadening effects.

In order to get lower g-factors for the static magnetic field, we also decided to use this time a higher value of the rotation angle  $\theta$ , i.e.  $>10^\circ$ . Using again the Sun et al. graphs [figure 4.6 (a) and (b)], we started with  $\theta \approx 20^\circ$  in order to observe the last transition close to the border of our magnetic field scanning range ( $\approx 280$  mT).

Furthermore, it is important to mention that the next presented measurements using a 50 ppm Er:YSO crystal have been operated with a loop to cavity wall grounding using just ordinary solder tin.

This case is different from the previously mentioned silver grounding as presented in figure 4.14. Such tin could in principle cause some distortions to the applied magnetic fields at low temperatures induced by superconductive currents and thus leading to inhomogeneities.

However, such effects could not be observed or determined directly at measurements. In principle it is always recommended to use silver for such purposes instead of solder tin, which may could possess components getting superconductive at low temperatures and thus could lead to unwanted effects.

Figure 4.15 on the next page shows the first measurement of the 50 ppm Er:YSO crystal at cryogenic temperatures ( $\approx 25$  mK), using a higher externally coupled cavity.

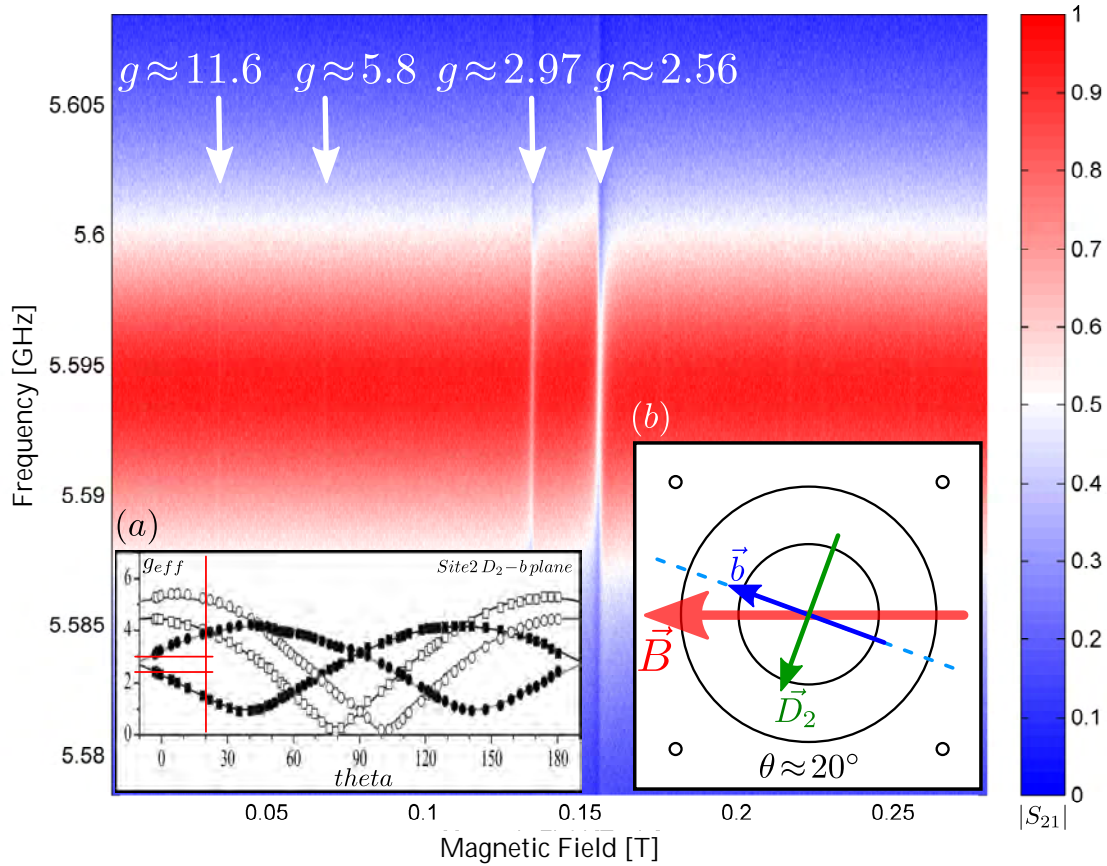


Figure 4.15.: ESR spectrum of the first measurement using a 50 ppm Er:YSO crystal with higher externally coupled resonator. The first two transmissions are rather hard to determine from figure, but are indicated via white arrows with its calculated g-factors. The third and fourth transition are clearly observed, where its calculated g-factors do not fit the effective g-factors graph of inset (a) for an angle  $\theta$  of  $\approx 20^\circ$  (indicated by red, thin lines). (b) Crystal orientation of  $20^\circ$  with respect to the applied magnetic field. Inset (a) taken from [SBTC08].

As previously mentioned, the crystal orientation was chosen for this measurement to be  $\theta \approx 20^\circ$ , where we expected to find two transitions with g-factors of  $\approx 3.9$  and  $\approx 1.5$  using again the effective g-factor graphs from Sun et al. [SBTC08].

For this measurement it seems not to be the case as presented in figure 4.15. Inset (a) presents the calculated g-factors of the 3<sup>rd</sup> and 4<sup>th</sup> transition using red, thin lines as markers. It is seen, that the intersection points do not match the black dotted curve, which could be an indicator for an misalignment of the crystal with respect to the magnetic field, or a deviation of the crystal axes from its expected positions due to an improper cut of the crystal.

Usually there are always some slight misalignments which are in the most cases negligible, but in this case also slight variations of  $\theta$  would not fit the graphs. Furthermore, again equation 4.2 was fit to the last transition in order to extract  $g_{coup}$  and  $\Gamma$ , which in this case was determined with  $8.9 \pm 0.0$  MHz and  $23.9 \pm 0.3$  MHz, respectively.

If comparing the  $g_{coup}$  result of the previous presented measurement for a weak externally coupled cavity using a 200 ppm erbium doped crystal, a higher coupling strength is achieved.

As the coupling strength is usually enhanced by a higher doping concentration, i.e.  $g_{coup} \propto \sqrt{N}$  [AKN<sup>+</sup>11], where N is the number of spins, even a reduction of the concentration as in our case by approximately a factor of two leads to a higher coupling rate, presumably due to higher external coupling.

In order to check if the crystal axes are different as expected, further measurements have been done on other crystal orientations. These measurements are summarized in table 4.3, also including the previously discussed measurement:

50 ppm Er:YSO (ESR spectroscopy results)							
Measurement		Transitions ( $\approx$ g-factor)				MHz	
No.	$\approx \theta^\circ$	1 <sup>st</sup>	2 <sup>nd</sup>	3 <sup>rd</sup>	4 <sup>th</sup>	$\approx g_{coup}$	$\approx \Gamma$
1	20	11.6	5.8	2.97	2.56	9	24
2	15	11.0	5.8	2.89	2.69	5	24
3	30	13.2	2.8	2.48	2.25	13.5	20
4	37	?	2.7	2.14	1.77	8	20

Table 4.3.: ESR measurements of a 50 ppm doped Er:YSO crystal for different orientations of  $\theta$  according to the D<sub>2</sub>-b plane with extracted DC g-factors. Furthermore, the coupling strength  $g_{coup}$  and the spin linewidth  $\Gamma$  of the most distinct transition have been extracted, presented in frequency values.

As it is observable from table 4.3, for the second measurement we reduced the angle  $\theta$  by 5°, where the most distinct observed transitions just changed slightly.

For example, transition three moved just a little bit to higher magnetic fields (decrease of the g-factor), whereas the fourth transition moved to lower magnetic fields (increase of the g-factor).

In principle, no big changes have been observed for the first two measurements. The situation changed rather for higher rotations of  $\theta$ , as it was the case for measurement number 3 and 4.

It is seen from table 4.3 that the 2<sup>nd</sup> transition of the third measurement moved distinct to higher magnetic fields, whereas the fourth measurement already showed a low g-factor value of 1.77. The 1<sup>st</sup> transition of measurement number 4 could not be obtained clearly, therefore not presenting its g-factor.

The reason for the variations of the coupling strength  $g_{coup}$  could not be determined clearly, but in principle the coupling strength amounts to be on average  $\approx 9$  MHz and thus definitely higher than for the measurement with lower external coupling. The value of  $\Gamma$  seems to get smaller for higher magnetic fields.

Further effects are observable directly from the measurement spectra, as presented in figure 4.16 and figure 4.17 on the next page.

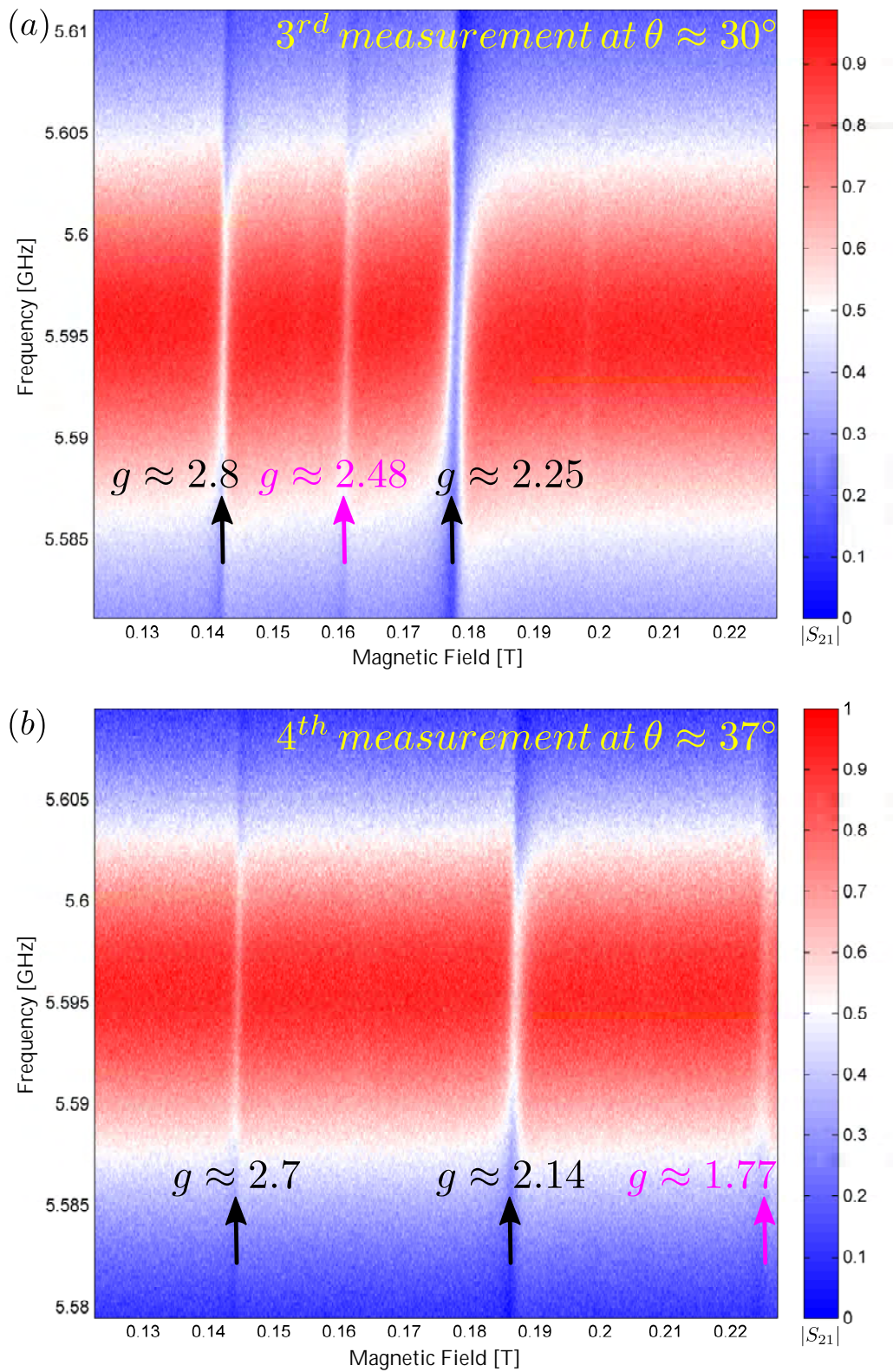


Figure 4.16.: ESR spectrum for a 50 ppm Er:YSO crystal. (a) 3<sup>rd</sup> measurement at  $\theta \approx 30^\circ$  between 120 and 230 mT, presenting the last three transitions. (b) 4<sup>th</sup> measurement at  $\theta \approx 37^\circ$  between 120 and 230 mT, again presenting the last three transitions. The transition marked in purple is still weaker than the other two, even for higher magnetic fields.

Figure 4.16 (a) shows the measurement results for a crystal orientation of  $\theta \approx 30^\circ$ , whereas (b) was measured for an angle of  $\theta \approx 37^\circ$ . Two distinct effects are observed for the transition marked with a purple arrow in both plots (a) and (b). The transition in figure 4.16 (a) is still weaker than the two other ones (marked by black arrows). If changing  $\theta$  by  $\approx 7^\circ$ , the transitions marked by black arrows do not change its positions significantly. Alternatively, the transition marked in purple changes quite distinct, which is also observable from the g-factor. Furthermore, the transition strength does not change appreciable for higher magnetic fields, whereas the other two transitions are still stronger in transition as it was the case for the measurement (a) of figure 4.16. In addition, there is another difference between figure 4.16 (a) and (b), which is the overall transition strength being in general weaker for (b). This observed effect could not be explained or determined exactly.

Another interesting effect was observed at a measurement for the same orientation of  $\theta \approx 37^\circ$ , where two measurements have been taken with a break of 3 days in between, presented in the figure 4.17:

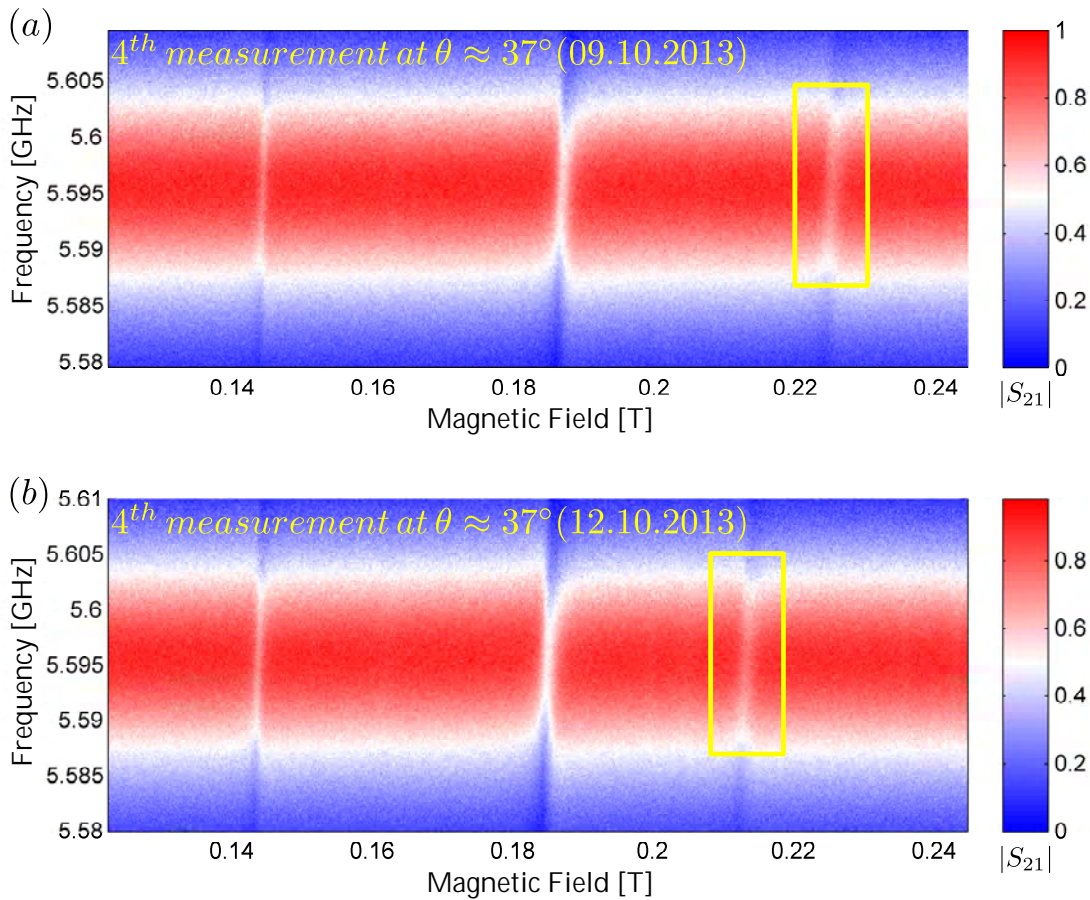


Figure 4.17.: ESR spectra of the 4<sup>th</sup> measurement using a 50 ppm Er:YSO crystal at  $\theta \approx 37^\circ$  between 120 and 245 mT, observing the last three transitions. (a) Spectrum taken on 9<sup>th</sup> of October. (b) Spectrum taken on 13<sup>th</sup> of October, after a measurement break of three days. The highest observed transition (see yellow squares) changed its position after the measurement break, which is a temperature effect. In comparison, the other two transitions did not change its position significantly.

On the 8<sup>th</sup> of October the cryostat reached  $\approx 25$  mK, where the first measurement was taken one day after [9<sup>th</sup> of October, figure 4.17 (a)]. In order to check the cavity and the sample according its temperature behavior, we stopped the measurements for 3 days to avoid temperature influences from outside and to let the system completely relax down. Surprisingly, the measurement from 12<sup>th</sup> of October showed a change of the transitions

in position, i.e. the position according to the magnetic field [figure 4.17 (b)]. Especially the change in position was distinct for the last transition, indicated by a yellow rectangle in figure 4.17 (a) and (b). This observation showed us, that there are some temperature effects, which is most probably caused by the teflon plugs. As the teflon plugs serve as the crystal sample holder, we think, that the teflon plugs rather contract more slowly than the crystal. Thus, leading to slight misalignment of the crystal itself with respect to the applied magnetic field. Such alignments would be noticeable as transition shifts, which are definitely observed in figure 4.17. With the data of the last measurements and the 50 ppm Er:YSO, we used a self-modified version of the simulation software EasySpin (www.easyspin.org, [SS06]) in order to determine the correct orientation of the crystal axes. We feed the software with the corresponding g-tensors for site 1 and site 2 taken from Guillot-Noël et al. [GNBG<sup>+</sup>06]. The next step was to let the program vary the corresponding angles  $\theta$  and  $\phi$  until certain g-factors have been found in a defined magnetic field range matching approximately our measured g-factors. In detail, we adjust the angles manually to match the factors more accurately. Finally, we extracted  $\phi = 78^\circ$ , which is different from our expected value of  $\phi = 90^\circ$ . Simulations matching our measurements with corresponding  $\theta$  values are found in figure 4.18:

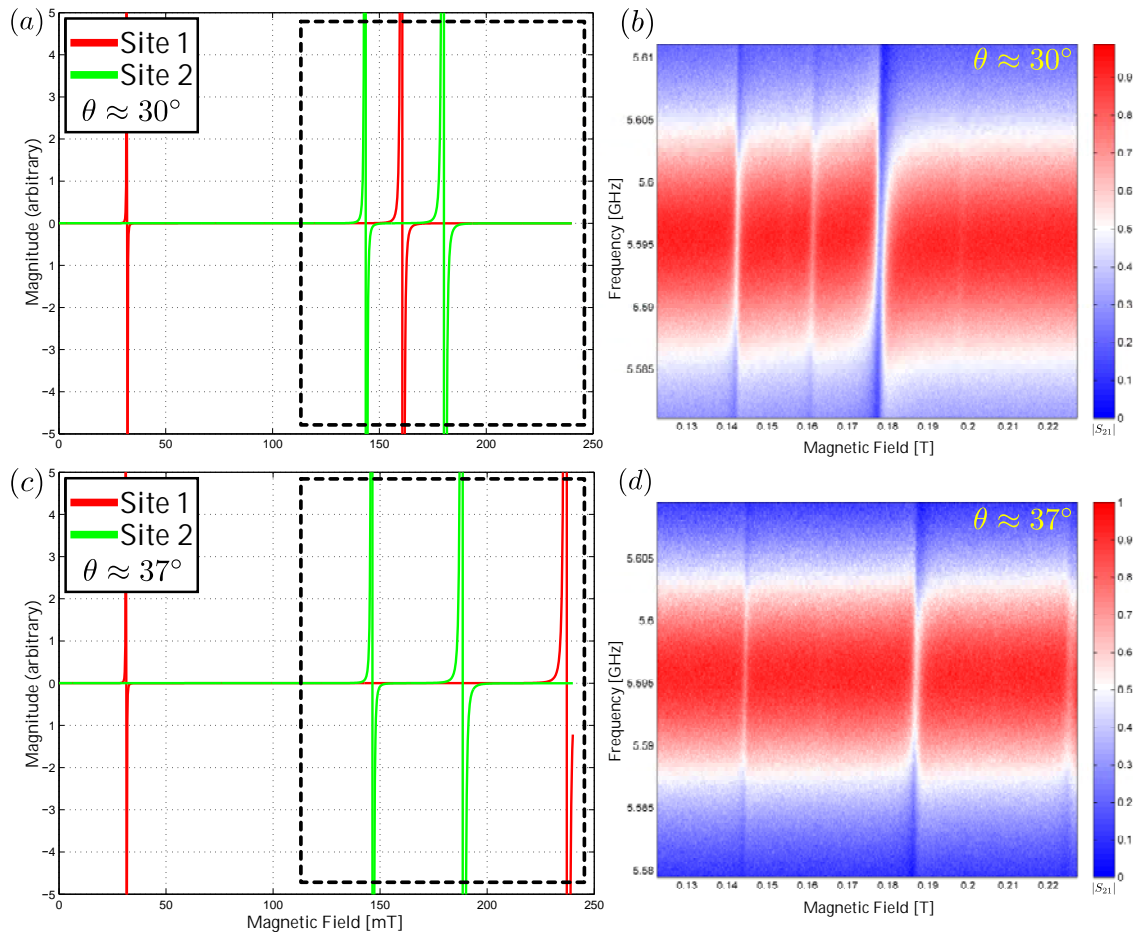


Figure 4.18.: Simulation results compared to measured ESR spectra. (a) and (c) are EasySpin simulations for  $\phi = 78^\circ$ , where (a) is for  $\theta \approx 30^\circ$  and (c) for  $\theta \approx 37^\circ$ , using magnetic field versus the magnitude of the transitions in arbitrary units (not to scale). Transitions in red correspond to site 1, whereas the green ones correspond to site 2. The black dashed box of part (a) and (c) show the section equivalent to the measurements of (b) and (d), respectively. (a) and (c) show all 4 transitions.

Figure 4.18 (a) and (c) are simulations using the EasySpin [SS06] software. Figure 4.18 (a) shows the case for  $\theta \approx 30^\circ$ , which is matching our measurement results as confronted in (b).

The simulation is plotted as the magnetic field versus the magnitude of the transitions in arbitrary units. The magnitude of the simulation is not correlated to the real measurement amplitude and is set manually for the software simulations.

The black dashed box in (a) shows the region of the measurement (b), where the similar case is found for figure 4.18 (c) and (d). If comparing the simulation (a) with the measurement (b), or (c) and (d), it is seen that the weak transitions corresponds to the magnetically inequivalent site 1 (red curve for simulation), whereas the green transitions correspond to site 2. Such green transitions in the simulation correspond to the distinct transitions as observed in measurement.

Furthermore, it is seen from the simulation and the measurement that one of the site 1 transitions rather change its position stronger for relatively small changes of the angle  $\theta$ . This does not seem to be the case for site 2.

On the other hand, the second transition of site 1, found at relatively low magnetic fields [figure 4.18 (a) and (c)], even does not change its position significantly. In order to explain the relatively weak transitions observed for site 1, we plotted the DC and AC g-factors respectively for site 1 and 2 in the same manner as it is found for the graphs of Sun et al. [SBTC08], using the data from simulation.

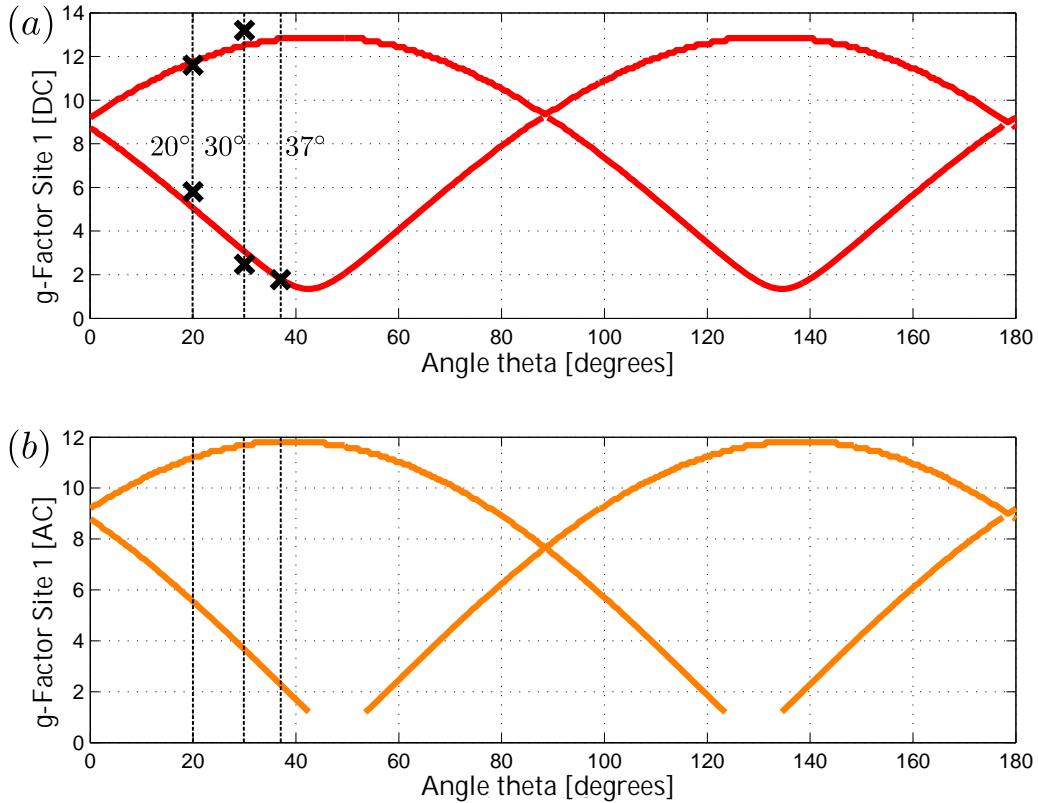


Figure 4.19.: Extracted g-factors from EasySpin simulations for  $\phi = 78^\circ$  regarding site 1. (a) g-factors for the static magnetic field (DC). Black crosses mark the measured g-factor values (see e.g. table 4.3). (b) g-factors for the oscillating magnetic field as present in the resonator cavity. Both plots show that the DC g-factor scales simultaneously with the AC g-factor for same values of  $\theta$ .

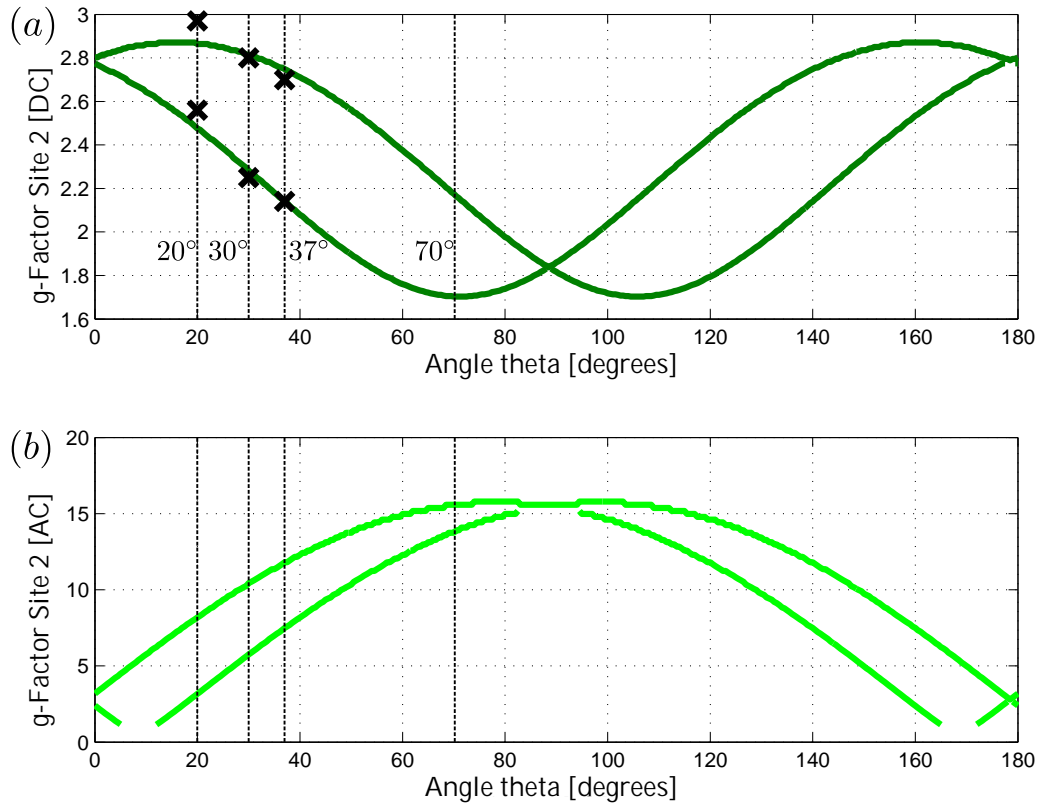


Figure 4.20.: Extracted g-factors from EasySpin simulations for  $\phi = 78^\circ$  regarding site 2. (a) g-factors for the static magnetic field (DC). Black crosses mark the measured g-factor values (compare e.g. table 4.3). (b) g-factors for the oscillating magnetic field as present in the resonator cavity. Both plots show that for same values of  $\theta$  lower DC g-factors correspond to higher AC g-factors.

Our explanation regarding the weak observed transitions is found for the g-factors describing the oscillating (AC) magnetic field as present inside the resonator cavity. From the discussions found in chapter 3.4, the coupling is enhanced for high values of the AC g-factor. Hence, comparing the AC g-factors of site 1 [figure 4.19 (b)] with that of site 2 [figure 4.20 (b)], we seen that the AC g-factor of site 1 nearly scale simultaneously with the DC g-factor. In the case of site 2 the situation changes, as for lower values of the DC g-factor higher values of the AC g-factors are found. Thus, to reach a high value of an AC g-factor, we decided to rotate the crystal to  $70^\circ$  of  $\theta$ , as marked in figure 4.20 (a) and (b) by a dotted line at  $\theta = 70^\circ$ .

Furthermore, we decided to use  $70^\circ$  in order to be able to resolve all 4 transitions. For angles higher than  $70^\circ$  the transitions start to merge. We expect to achieve for a DC g-factor of  $\approx 1.7$  an AC g-factor of  $\approx 14$  or more, as it would be needed to get into the strong coupling regime. The other dotted lines found in figure 4.19 and 4.20 are the  $\theta$  positions regarding the experimental measurements for  $20^\circ, 30^\circ$  and  $37^\circ$ . The black crosses in part (a) of both figures are the extracted g-factors from measurement, as it is also found in table 4.3.

### 4.3.3.1. Strong Coupling

Rotating the crystal to an angle of  $\theta \approx 70^\circ$ , we furthermore adjusted the teflon plugs, in order to avoid stress onto the crystal due to thermal contraction effects as it was observed in figure 4.17. Additionally, this time we grounded the coupling loops to the cavity walls using silver, as already discussed previously (see e.g. figure 4.14).

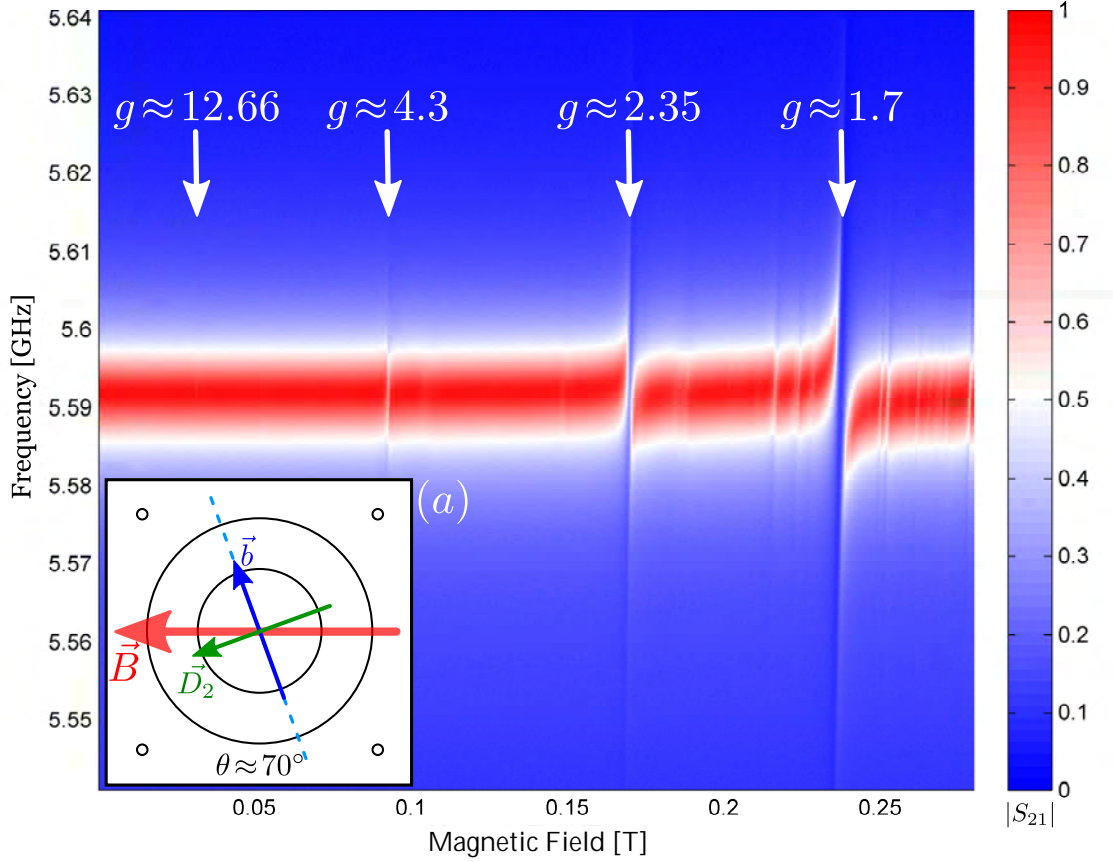


Figure 4.21.: ESR spectroscopy of Er:YSO for a crystal orientation of  $\theta \approx 70^\circ$  [inset (a)]. The main transitions are indicated by white arrows with its calculated DC g-factors. Weaker and smaller transitions around the distinct transitions are likely hyperfine transitions. The last, main transition with a g-factor of  $\approx 1.7$  indicates strong coupling.

As expected, at mK temperatures we observed the transitions at its predicted positions according to figure 4.19 and 4.20 for  $\phi \approx 77^\circ \pm 1^\circ$ , determined by the corresponding DC g-factors. Additionally, smaller and weaker transitions distributed around the main transition are the hyperfine transitions according to the  $^{167}\text{Er}^{3+}$  isotopes. The complete spectrum as presented in figure 4.21 was measured at approximately 38 photons, determined by equation 4.3:

$$N = \frac{P\tau}{hf_c}. \quad (4.3)$$

$N$  is the number of photons,  $P$  is the power,  $h$  is the Planck constant and  $f_c$  the resonators center frequency. The lifetime of a photon inside the cavity is determined by  $1/\Delta f$ , which is  $\tau$  in equation 4.3. The power was determined from the VNA and the attenuation towards the waveguide resonator, expecting thus a power of  $\approx 1$  fW at the resonator.

Finally, the last distinct transition with  $g$ -factor of  $\approx 1.7$  showed strong coupling behavior. In order to proof this, we used the transmission signal of the resonator at the anti-crossing point and normalized it to the initial resonator transmission signal without disturbance.

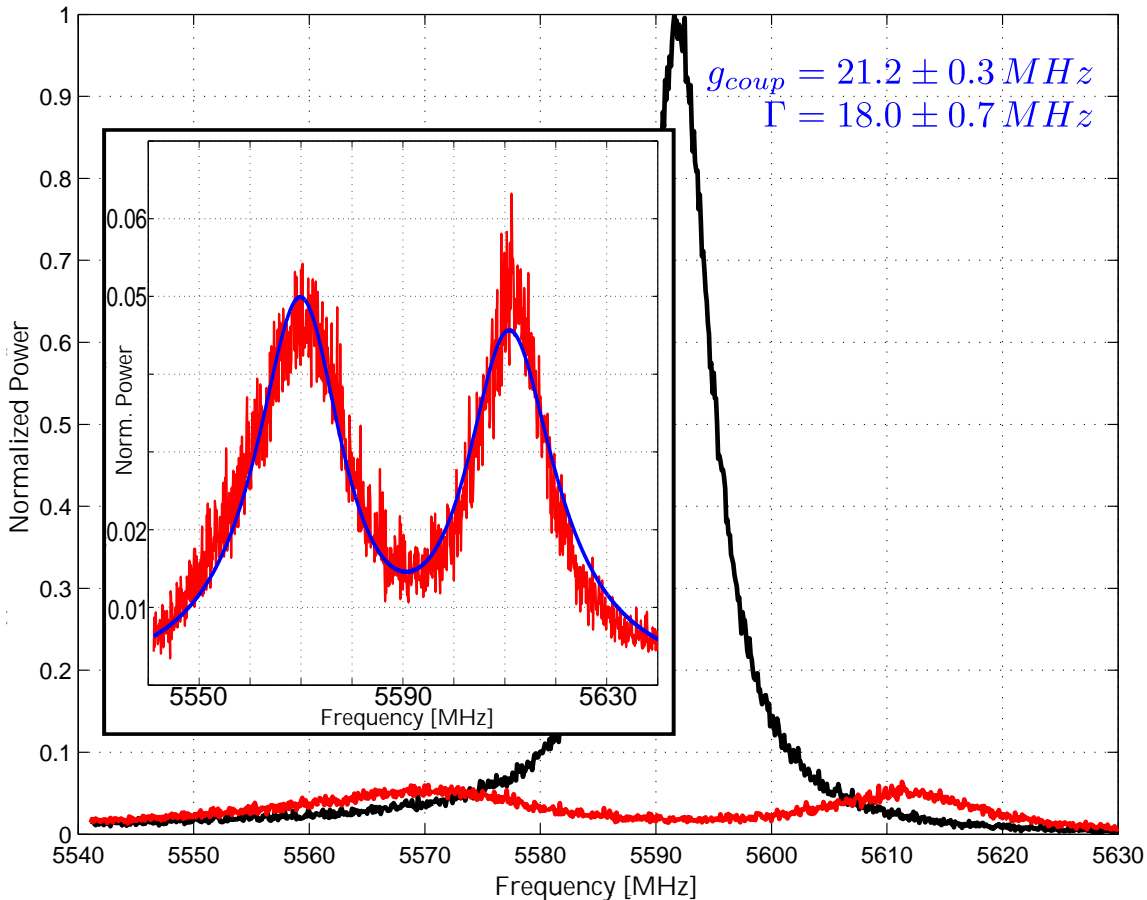


Figure 4.22.: Mode splitting (red) of the  $g \approx 1.7$  transition as observed in figure 4.21. The data was normalized with respect to the undisturbed resonator signal (black). From fit (see inset (a), blue line) the coupling strength  $g_{coup}$  was determined with a rate of  $21.2 \pm 0.3$  MHz, whereas the spin linewidth was determined with a rate of  $\Gamma = 18.0 \pm 0.7$  MHz, using values at HWHM.

The extracted mode splitting presented in figure 4.22 (red) in comparison to the undisturbed resonator (black) was fitted according to equation 4.4, as similarly published by Schuster et al. [SSG<sup>+</sup>10]:

$$|S_{21}|^2 = \left| y_0 + \frac{\kappa_L A}{i(f - f_r) - \kappa_L + \frac{g_{coup}^2}{i(f - f_e) - \Gamma}} \right|^2. \quad (4.4)$$

Here,  $y_0$  is used for offset- and  $A$  for amplitude corrections, where  $f_r$  is the center frequency of the resonator and  $f_e$  is the resonance frequency of the ensemble. The parameter  $g_{coup}$  is the coupling strength,  $\Gamma$  is the spin linewidth at HWHM,  $i$  serves as the imaginary number and  $\kappa_L$  is the loaded resonator linewidth at HWHM. In comparison with the previous measurements, the coupling strength increased, whereas the spin linewidth  $\Gamma$  did not change significantly. A mode splitting was only observed for the previously mentioned transition, where in comparison the second distinct transition of figure 4.21 was determined with  $g_{coup} = 12.5 \pm 0.5$  MHz and  $\Gamma = 22.1 \pm 1.3$  MHz.

### 4.3.3.2. Power Dependence of the Strongly Coupled Transition

In order to study the power dependence of the strongly coupled transition, we probed the mode splitting on different powers and thus on different number of photons, as displayed in figure 4.23.

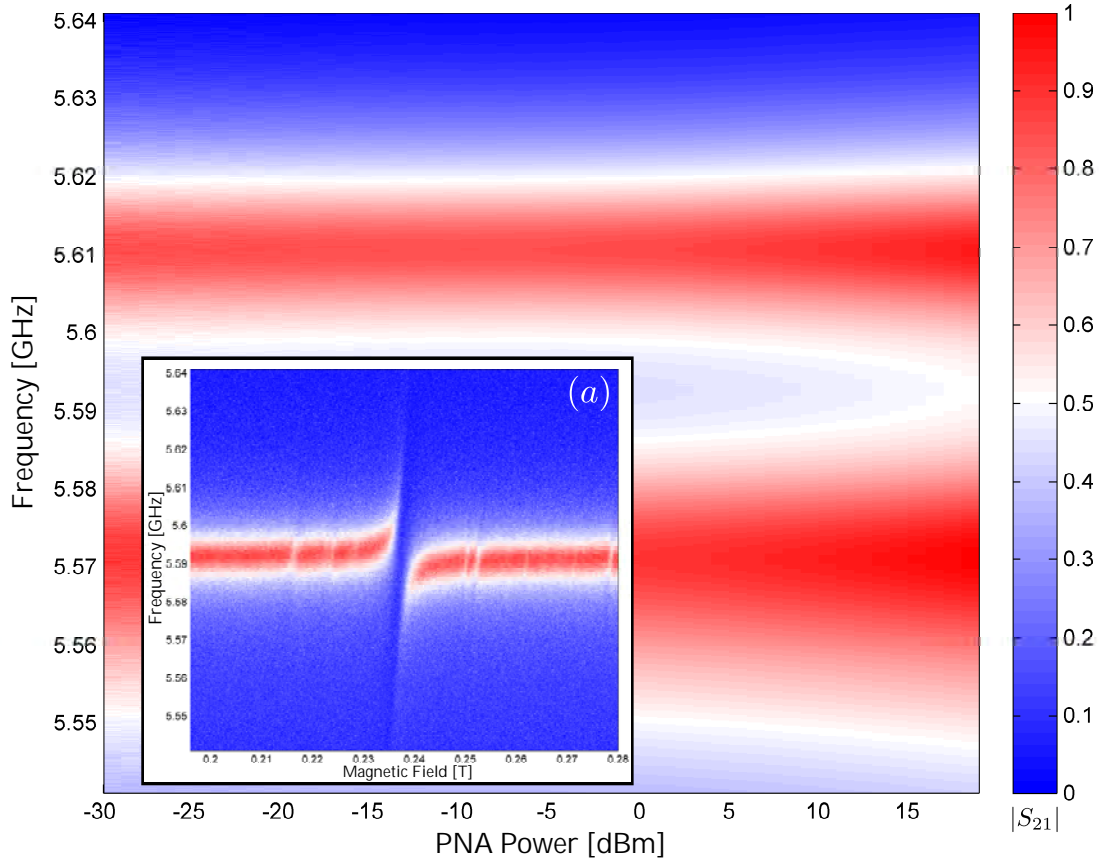


Figure 4.23.: Mode splitting according to different applied powers. The power was varied directly at the VNA, showing the values on the horizontal line in dBm. Taking into account the attenuation, this figure represents the photons present inside the resonator, which ranges from  $\approx 375$  to  $37.5 \cdot 10^6$ . (a) Approximately single photon regime measurement of the strongly coupled transition.

Different VNA powers, as shown in figure 4.23 on the horizontal axis, correspond to  $\approx 375$ - $37.5 \cdot 10^6$  photons if taking the additional attenuators into account. As it is seen from figure 4.23, no significant change of the mode splitting is observed. Except for VNA powers close to 20 dBm, the two transmission peaks (red) of the mode splitting start slightly to broaden. As the used VNA was limited to 20 dBm, only measurements up to  $\approx 37.5 \cdot 10^6$  photons were possible.

Inset (a) of figure 4.23 represents the approximately single photon regime measurement. In order to get into the single photon regime we used -50 dB for the adjustable attenuator on applying -5 dBm (including the attenuation inside the cryostat, plus cables).

### 4.3.3.3. Coupling Strength Versus Temperature

Another experiment which was carried out according to the mode splitting is the behavior of the coupling strength  $g_{coup}$  with respect to increasing temperature:

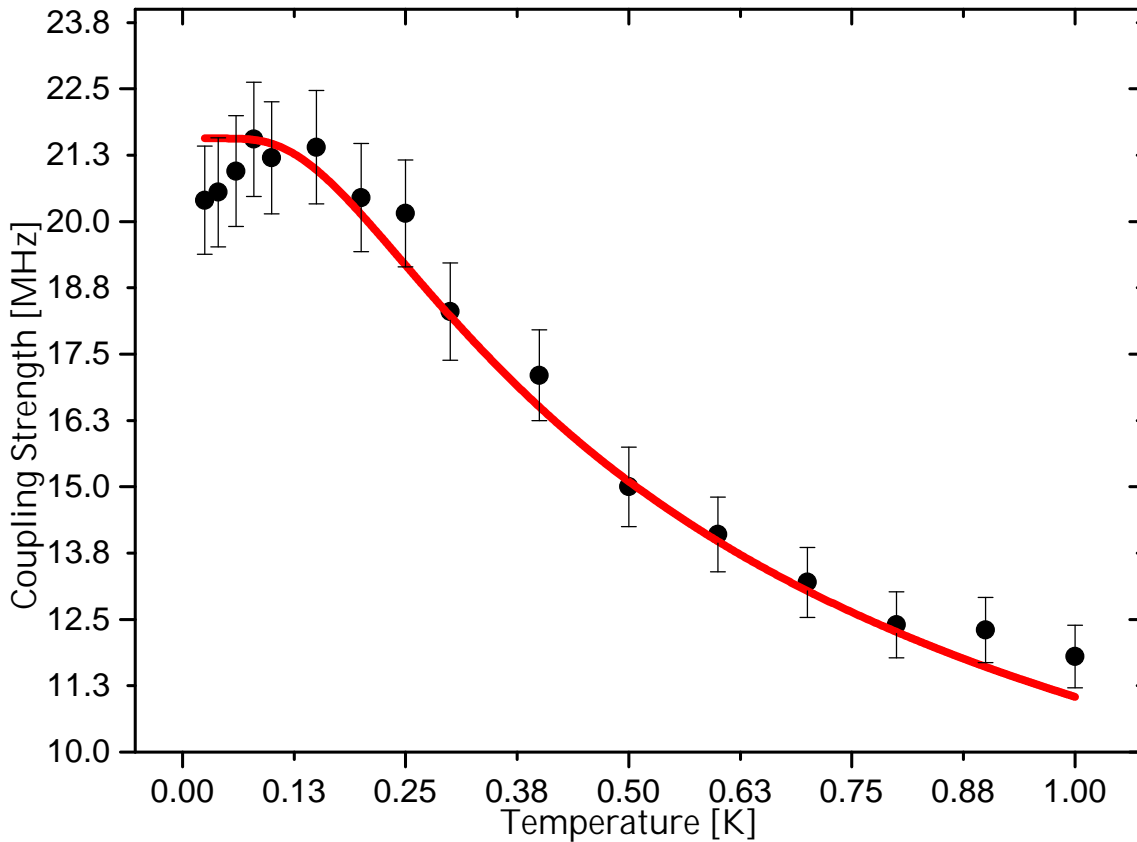


Figure 4.24.: Measurement (black points) of the coupling strength  $g_{coup}$  in MHz as a function of the temperature in Kelvin. Fit (red) according to equation 4.6 using only  $g_{coup}(0)$  as fit parameter, resulting in  $21.6 \pm 0.2$  MHz.

For figure 4.24 we increased the temperature at the mixing chamber, while waiting for approximately 30 minutes before starting the measurement of the strongly coupled transition. The time delay after temperature increase and measurement is necessary, as the temperature increase displayed by the temperature sensor is not implicitly the same at the sample. From the measured data sets we extracted again the coupling strength  $g_{coup}$  using equation 4.4.

The coupling strengths is first rising to higher values in the temperature region between 0 and  $\approx 100$  mK, but then dropping with the hyperbolic tangent square root behavior as described by equation 4.6.

In this case we are not sure if we just observe measurement errors, or if this could be a general behavior of a 3D waveguide resonator cavity coupled to Er:YSO. Maybe additional measurements using other erbium doped crystals in combination with 3D waveguide resonators will confirm or refute such a behavior for temperature regions between 0 and  $\approx 100$  mK.

As a usual procedure, we tried to fit the formula 4.5 to the data presented in figure 4.24. This was also done by several other groups for temperature dependent coupling strengths, as e.g. [BFR<sup>+</sup>11, SRA<sup>+</sup>12, RdS<sup>+</sup>13].

$$g_{coup}(T) = g_{coup,S} \sqrt{N \tanh\left(\frac{hf_0}{2k_B T}\right)} = g_{coup}(0) \sqrt{\tanh\left(\frac{hf}{2k_B T}\right)}. \quad (4.5)$$

The parameter  $g_{coup,S}$  in equation 4.5 is the coupling strength for a single spin, whereas in combination with the collective number of spins  $N$  the coupling at zero temperature [ $g_{coup}(0)$ ] is defined.

In order to fit this theory to our data, we used only  $g_{coup}(0)$  as fit parameter, whereas the other parameters like  $h$  (Planck constant),  $f_0$  (resonance frequency) and the Boltzmann constant  $k_B$  are known. However, fitting procedures using equation 4.5 did not lead to satisfactory fitting results.

Alternatively we introduced an additional fit parameter to the argument of the hyperbolic tangent function of equation 4.5, which led to a factor of  $\approx 0.5$ . Thus we used equation 4.6 to fit our data:

$$g_{coup}(T) = g_{coup}(0) \sqrt{\tanh\left(\frac{hf}{k_B T}\right)}. \quad (4.6)$$

Finally, we achieved a way better fitting result using this equation as it was the case for equation 4.5. A similar case was also recently observed by S. Probst using a transmission line resonator (copper), probing a 50 ppm Er:YSO crystal [Pro13]. The difference between equation 4.5 and 4.6 is the value of 1/2 in the argument of the hyperbolic tangent expression. Thus, a factor of 2 in the hyperbolic tangent argument changes the situation for the ordinary derived theoretical equation. Up to now we can not explain the origin of such a factor of 2.

The derivation according to equation 4.5 is explained by e.g. Feynman [FLS64] using  $N_1 \sim N \frac{\exp(x)}{\exp(x)+\exp(-x)}$  as the population of the lower energy level and  $N_2 \sim N \frac{\exp(-x)}{\exp(x)+\exp(-x)}$  as the population of the upper energy level. The argument of the exponent is  $x = \mu B/k_B T$  according to the Boltzmann statistics and  $N = N_1 + N_2$ . The population difference of both levels is then found as:

$$N_1 - N_2 = N \frac{e^x - e^{-x}}{e^x + e^{-x}} = N \tanh(x), \quad (4.7)$$

where  $hf = 2\mu B$  if defining the  $z$ -component of the magnetic moment as  $\Delta E = \pm\mu_z B$ . Same derivation is also found from Kittel [Kit96], or see chapter 3.1, section 3.1.1 of this thesis.

In contrast to the simple derivation explaining equation 4.5, which just covers the uncoupled spins, one might need to consider the full system consisting of the resonator and the spin ensemble. However, plotting both equations against each other, it is clearly seen that equation 4.6 drops less with temperature as compared to equation 4.5. Such a difference between both equations is presented graphically in figure 4.25 (a) on the next page.

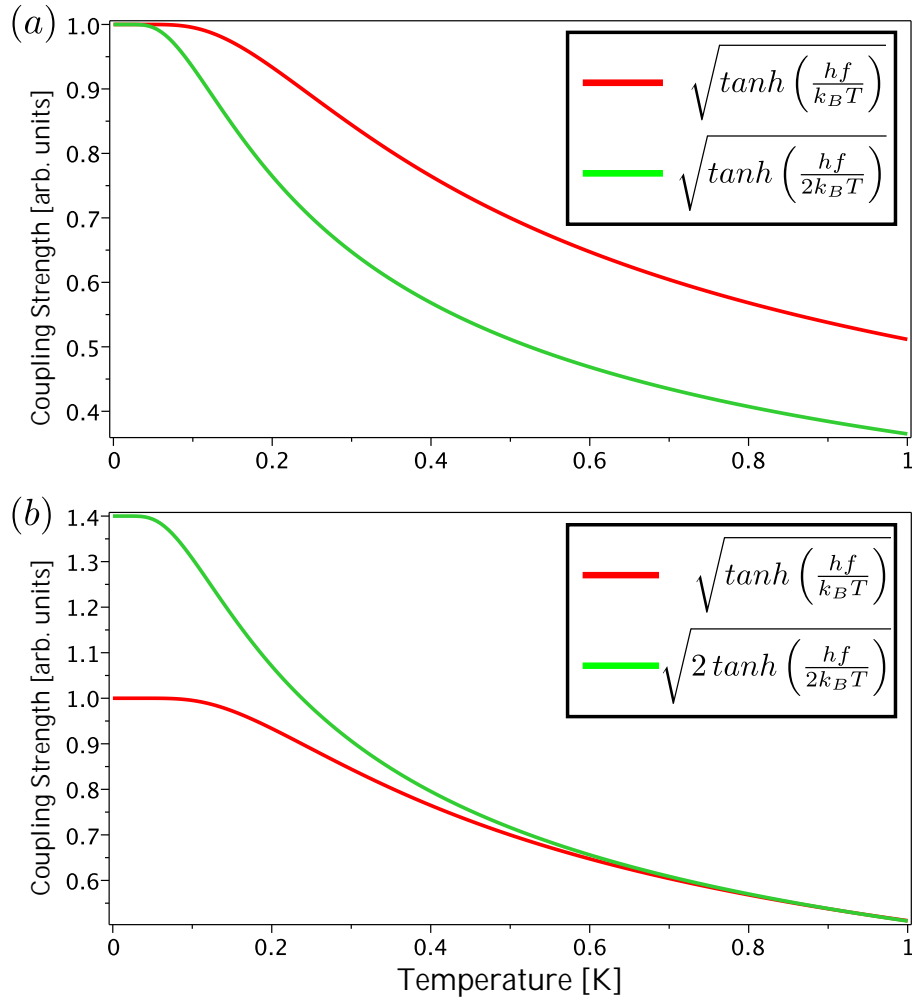


Figure 4.25.: Comparison of two cases of the square root of the hyperbolic tangent function representing the coupling strength (arbitrary units) as a function of the temperature in Kelvin. (a) Red curve: hyperbolic tangent function with argument  $1/T$ . Green curve: hyperbolic tangent function with argument  $1/2T$ . The coupling strength for the green curve drops more rapidly for  $T \approx 100$  mK. (b) Similar case as for (a), expect that a prefactor of 2 was used for the green curve in order to show the approach of both curves for  $g_{coup}$  for higher values of the temperature ( $\approx 400$  mK).

Figure 4.25 (a) shows the case for both equations 4.5 and 4.6, where a value for  $f$  was chosen according to waveguide resonator version 2 with 5.59 GHz.

The green curve clearly shows that the coupling strength  $g_{coup}$  drops more rapidly starting from  $\approx 100$  mK compared to the red curve.

For figure 4.25 (b), green curve, a different value for  $g_{coup}(0)$  or  $\sqrt{N} = \sqrt{2}$  was used to show that both curves are approaching same values of  $(\Delta g_{coup}/\Delta T)$  for higher values of the temperature.



## 5. Measurements using Superconductive Lumped-Element Resonators

---

### 5.1. Experimental Setup

The experimental setup regarding the measurements using superconducting lumped element resonators is in principle similar to the experimental setup as presented in chapter 4.1. Instead of using a Helmholtz coil to apply static magnetic fields, we used a solenoid coil. With such an arrangement inside the cryostat we were able to perform two experiments at one cool down procedure.

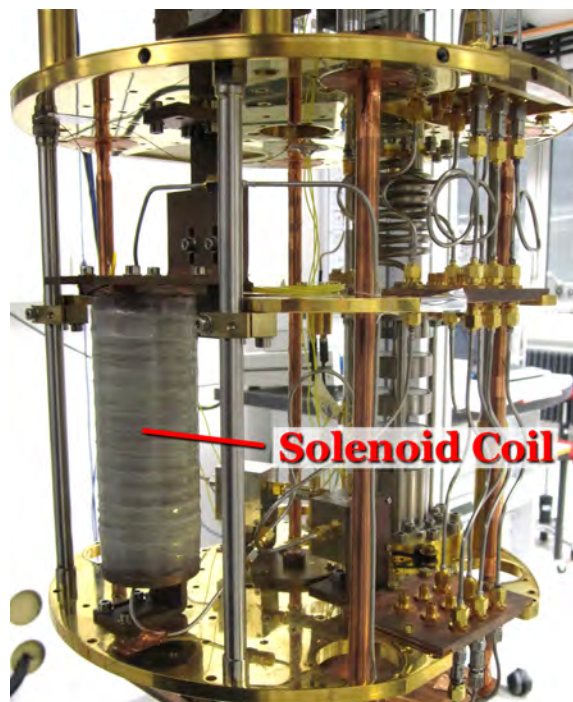


Figure 5.1.: Picture of the BlueFors cryostat without temperature shielding, showing the solenoid coil connected to the 700 mK stage (still, golden plate at the top of the figure).

The solenoid coil provides 0 to 400 mT and is connected to the 700 mK stage (still), which is seen at the top of figure 5.1. As the solenoid coil is positioned above the Helmholtz coil, we did not operate the Helmholtz coil while running the solenoid coil. The sample holder with the resonator is inserted into the solenoid coil, where the sample holder is mounted to the  $\approx 20$  mK stage (mixing chamber), which is the golden plate at the bottom of figure 5.1. The used amplifier for signal amplification after the resonator and circulator is able to amplify a frequency range of 4 to 8 GHz, which is sufficient for LEKID resonator usage. The word LEKID is usually used as a brand name for the resonators and means exactly

Lumped Element Kinetic Inductance Detectors [DMN<sup>+</sup>08, WHK<sup>+</sup>11]. In our case, we rather speak of resonators than detectors, but still calling the devices LEKID resonators.

Such resonators are made of small structures which look like lumped elements, as it is typically used in circuit designs. The resonance frequency is defined by the capacitive ( $C$ ) and inductive ( $L$ ) parts, as indicated in figure 5.2.

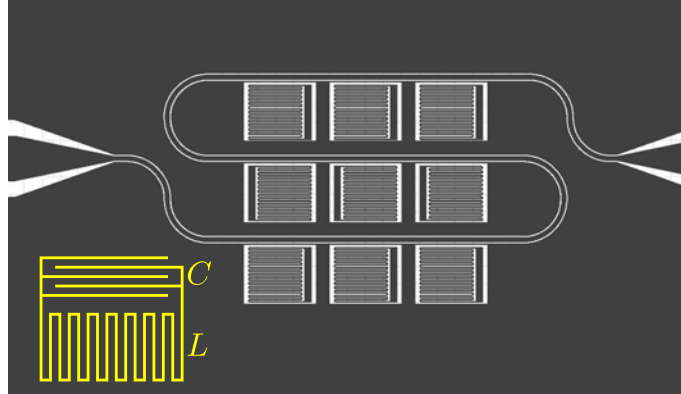


Figure 5.2.: Superconducting lumped element resonators (9 resonators) with feed line (transmission line). The lumped element structure is emphasized schematically in yellow, showing the capacitive ( $C$ ) and the inductive ( $L$ ) part.

The inductive part is achieved by a meandered line (see figure 5.2,  $L$ ), whereas the capacitive part are stripes or 'fingers' separated by a certain distance forming a lumped capacitor (figure 5.2,  $C$ ). The resonance frequency is then described by both parts as  $\omega_0 = 1/\sqrt{LC}$ , whereas superconductivity is beneficial to reach high quality factors.

## 5.2. ESR Spectroscopy of 200 ppm Doped Er:YAlO using a 9 LEKID Resonator

For microwave spectroscopy of a 200 ppm erbium doped yttrium orthoaluminate (Er:YAlO), the crystal was placed on top of a 9 LEKID resonator chip. The superconductive chip is placed inside a copper box as shown in figure 5.3:

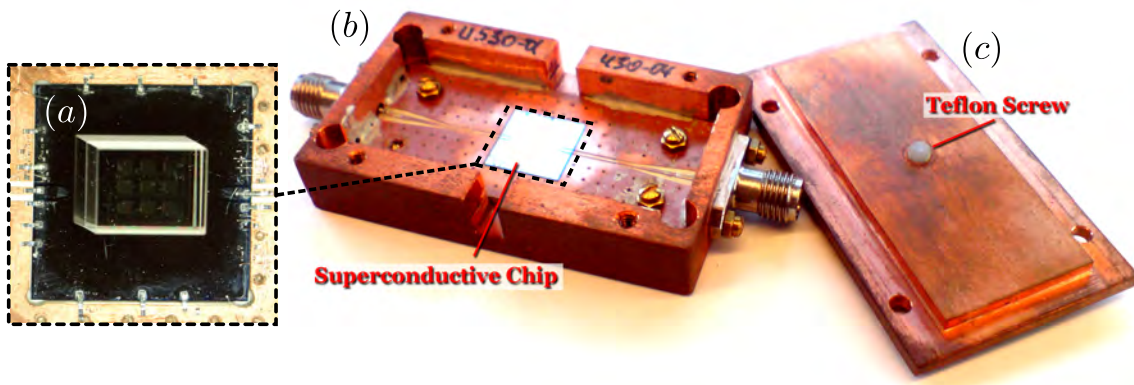


Figure 5.3.: (a) 200 ppm Er:YAlO crystal on top of a 9 LEKID resonator chip. (b) Copper box with coaxial cable connectors containing the superconducting chip. (c) Copper box cap with a teflon screw in the center, using it to fix the position of the crystal inside the copper box and the superconducting chip.

The crystal itself is separated by an air gap to the LEKID resonators, where the gap distance should be as small as possible for effective coupling. Such a gap distance is adjusted by observing Newton fringes. The fringes originate from the reflections of both interfaces leading to interference effects, where the gap distance is proportional to the observed fringes. In order to fix the final position of the crystal on top of the superconducting chip [figure 5.3, (a)], we use a teflon screw integrated in the center of the copper box cap [figure 5.3 (c)]. Finally, the complete copper box is mounted onto a sample holder, which is interjected into the solenoid coil. The 9 resonators on the superconducting chip are resonating between  $\approx 3.6$  and  $\approx 4.2$  GHz, where the frequency spacing between neighboring resonances is sometimes very narrow as e.g. observed from figure 5.4:

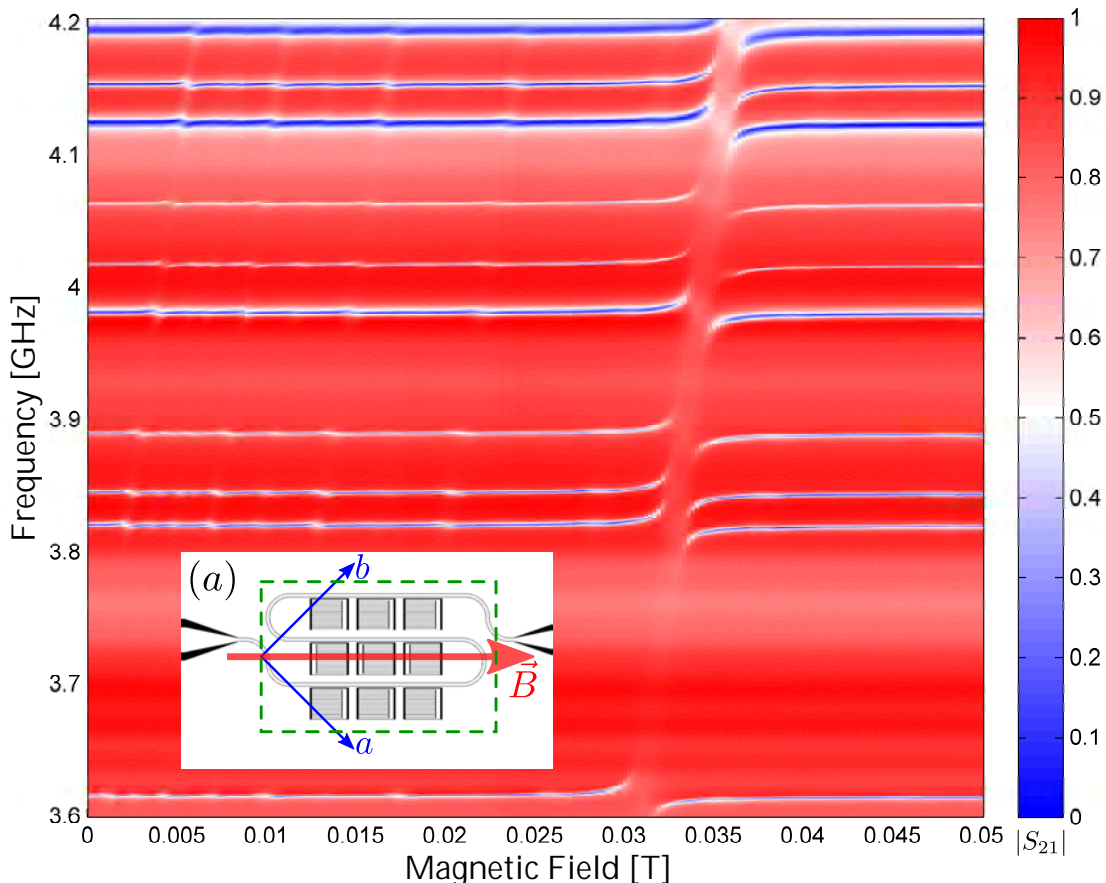


Figure 5.4.: ESR spectrum of a 200 ppm Er:YAlO crystal using a 9 LEKID superconducting resonator chip, where 9 resonances are observed due to the LEKIDs and one resonance is most likely a chip resonance. Transitions have been only observed for the displayed range of 0 to 50 mT. The main transition is clearly observed for each resonator between  $\approx 30$  mT and  $\approx 35$  mT. The crystal orientation with respect to the applied static magnetic field is presented in inset (a), where the crystal is indicated via a green dashed rectangle. The crystal axes are found in blue.

Figure 5.4 shows a measurement range from 0 to 50 mT for the applied static magnetic field from the solenoid coil. We also scanned for higher magnetic fields, but did not observe anything new above 50 mT. The main transition is found for a g-factor of ( $\approx 8.37$ ), which was extracted by fitting equation 4.2 to some of the observed transitions not highly disturbed by transition in the vicinity and taking the average. Furthermore, a coupling strength of  $\langle g_{coup} \rangle \approx 34$  MHz and a spin linewidth of  $\langle \Gamma \rangle \approx 33$  MHz have been extracted. Additionally, hyperfine transitions according to the  $^{167}\text{Er}^{3+}$  isotope are weakly observed between 0 and 30 mT. The crystal orientation with respect to the applied static magnetic field and its crystal axes  $a$  and  $b$  is schematically displayed in inset (a) of figure 5.4.

In order to observe also other transitions and to understand how the crystal behaves with respect to the applied static magnetic field, we decided to go for a second measurement with a different crystal orientation.

### 5.3. ESR Spectroscopy of 200 ppm Doped Er:YAlO using a 3 LEKID Resonator

To avoid influences of closely spaced resonances onto the transition spectrum, we decided to use a 3 LEKID superconducting chip for the second run. Additionally we rotated the crystal by  $45^\circ$  with respect to the applied static magnetic field as presented in inset (a) of figure 5.5:

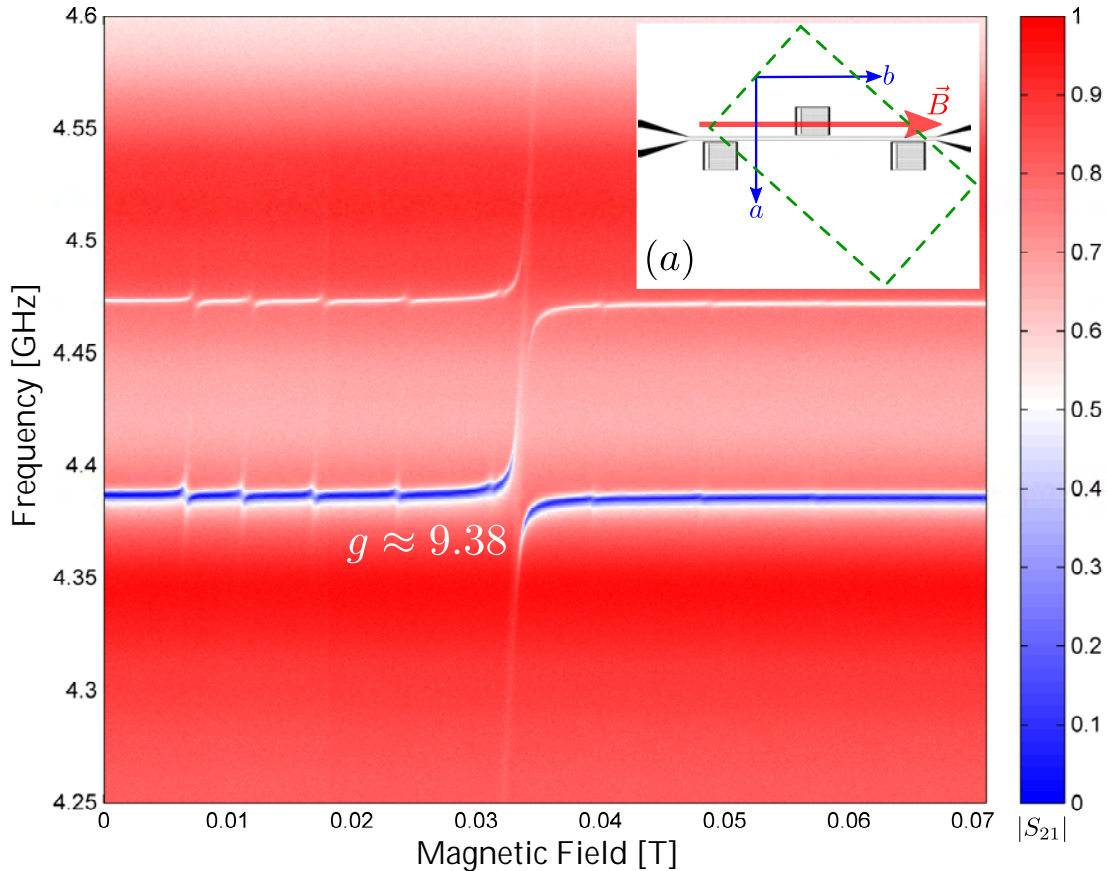


Figure 5.5.: ESR spectrum of a 200 ppm Er:YAlO crystal using a 3 LEKID superconducting resonator chip. Two transitions between  $\approx 30$  mT and  $\approx 35$  mT are clearly observed, corresponding to the two completely crystal covered LEKID resonators as schematically presented in (a). The crystal is indicated via a green dashed box, with corresponding crystal axes in blue. Additional hyperfine transitions are distributed around the main transition.

Inset (a) of figure 5.5 indicates that the crystal (green, dashed box) only occupies two of the lumped element resonators completely, whereas the third one is partially covered. Thus, only two transitions are clearly observed corresponding to the occupied resonators oscillating at  $\approx 4.39$  GHz and  $\approx 4.47$  GHz, respectively. The third resonator is not shown in figure 5.5 as no transitions were observed.

In order to prove if strong coupling is present between the 4.39 GHz resonator and the spin ensemble, the transmission signal at the anti-crossing has to be analyzed. For this

purpose additional corrections to the transmitted  $|S_{21}|$  signal have been necessary. First of all we subtracted the background signal from the mode split signal, as well as for the undisturbed resonator. The undisturbed resonator signal was used for data normalization, whereas the mode split signal showed a third dip between the main two dips of the mode splitting. Such third dip originates from the feed line of the LEKID chip architecture and should be removed from the transmission signal in order to clearly identify the mode splitting. Fitting three Lorentzian curves to each dip using OriginLab, the corresponding Lorentz fit values are used to get rid of the absorption line contributions. Finally, the pure mode splitting is observed:

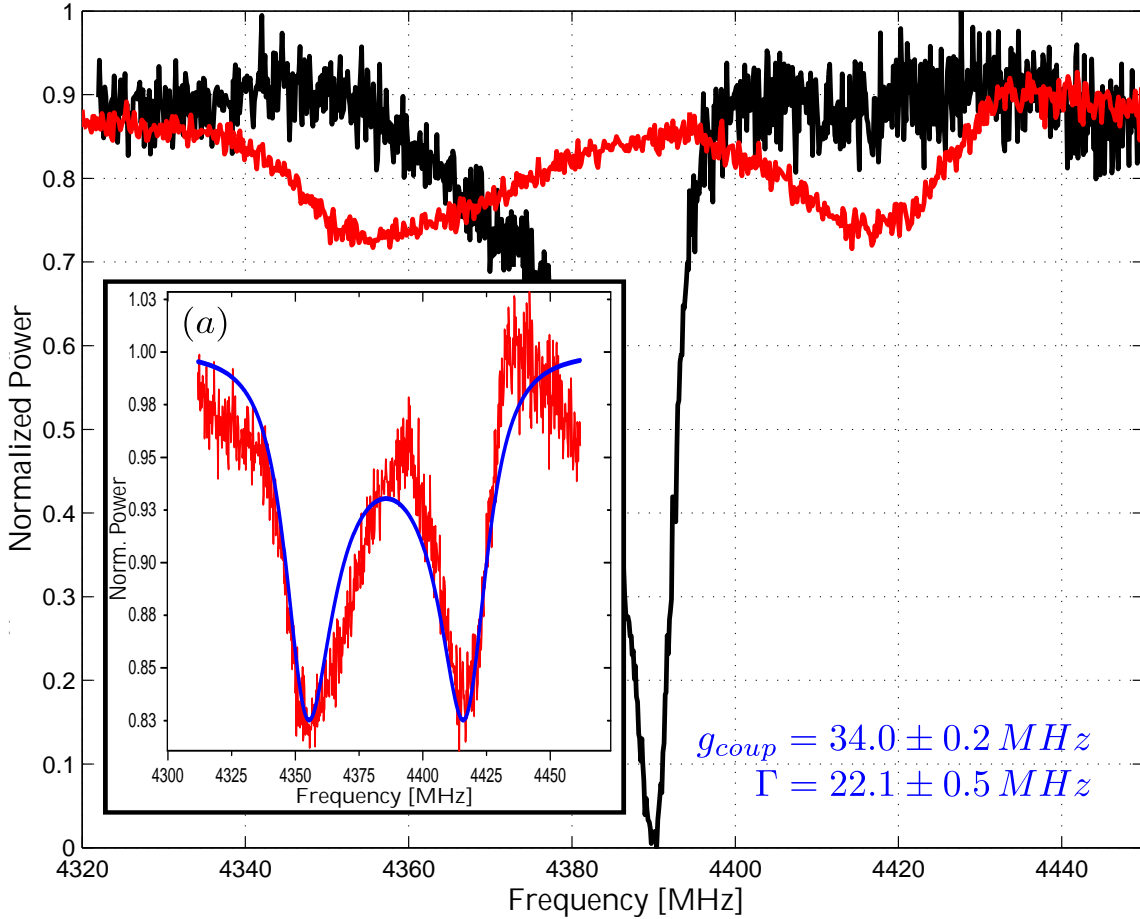


Figure 5.6.: Mode splitting (red) of the resonance at  $\approx 4.39$  GHz (black) showing strong coupling. Inset (a) shows the pure mode splitting with fit (blue) according to equation 5.1. Extracted fit values for the coupling strength are  $g_{coup} = 34.0 \pm 0.2$  MHz and  $22.1 \pm 0.5$  MHz for the spin linewidth  $\Gamma$ .

To determine the coupling strength  $g_{coup}$  and the spin linewidth  $\Gamma$  from the mode split power transmission signal (figure 5.6, red curve), we used the subsequent equation for fitting procedures:

$$|S_{21}|^2 = \frac{(\kappa\Gamma - g_{coup}^2 + (\omega - \omega_0)^2)^2 + (\omega - \omega_0)^2 (\kappa - \Gamma)^2}{(\kappa\Gamma + g_{coup}^2 - (\omega - \omega_0)^2)^2 + (\omega - \omega_0)^2 (\kappa + \Gamma)^2}. \quad (5.1)$$

The resonators decay rate is described by  $\kappa$ ,  $\omega_0$  is the center angular frequency,  $\Gamma$  is the spin linewidth and  $g_{coup}$  is the coupling strength (values at HWHM). Equation 5.1 represents a simplified version of the initially published equation by Afzelius et al. [ASJ<sup>+</sup>13]. We assumed that the homogeneous linewidth is  $\ll \Gamma$  and that  $g^2 N = g_{coup}$  for simplicity.

From the fit using equation 5.1 we extracted a coupling strength of  $g_{coup} = 34.0 \pm 0.2$  MHz and a spin linewidth of  $\Gamma = 22.1 \pm 0.5$  MHz. In comparison to equation 4.4, we achieved better fits to the strongly coupled transition using equation 5.1.

### 5.3.1. Coupling Strength Versus Temperature

We used the same procedure as previously described in section 5.3 to extract the coupling strength values for temperature dependent measurements as presented in figure 5.7:

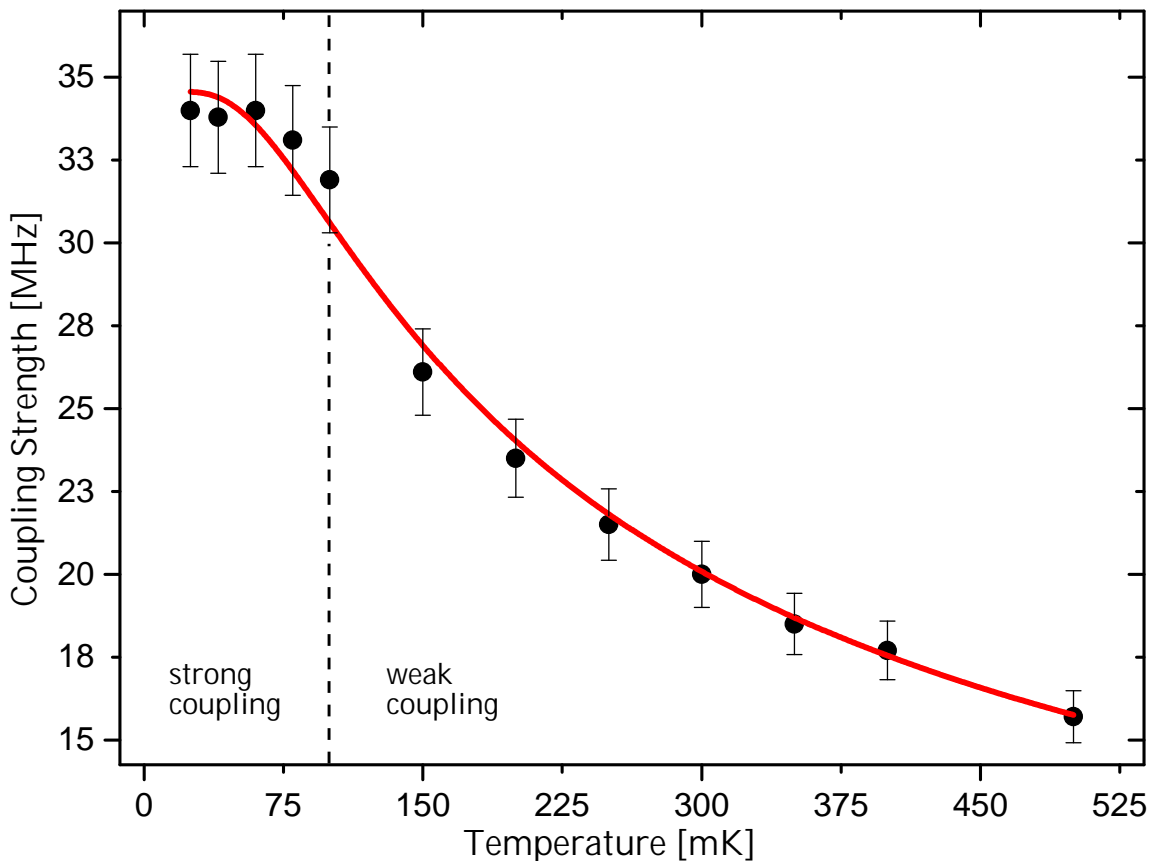


Figure 5.7.: The dependance of the coupling strength  $g_{coup}$  given in frequency values as a function of the temperature (mK). The black points are extracted  $g_{coup}$  values from appropriate fits using the measured data. The red curve was fitted according to equation 4.5 using only  $g_{coup}(0)$  as fit parameter.

The temperate measurement was realized in the same way as it was done for Er:YSO, coupled to a waveguide resonator (chapter 4.3.2). Strong coupling was observed up to a temperature of  $\approx 100$  mK for which we used equation 5.1 to fit and extract the  $g_{coup}$  values. Above 100 mK we used equation 4.2. Best fits for the extracted data are found for equation 4.5, i.e.  $g_{coup}(T) = g_{coup}(0) \sqrt{\tanh(hf/2k_B T)}$ . Only  $g_{coup}(0)$  was used as a fit parameter resulting in  $34.6 \pm 0.2$  MHz, whereas all other parameters are constants, except of the resonators resonance frequency (4.39 GHz).

From discussions found in chapter 4.3, section 4.3.2, the situation found in figure 5.7 describes a more rapid dropping of the coupling strength with respect to the temperature. Therefore, the choice of equation 4.5 is more appropriate. In case of Er:YSO coupled to a waveguide resonator we observed strong coupling up to  $\approx 700$  mK, where the data was more accurately described via equation 4.6.

### 5.3.2. Crystal Impurity ( $\text{Ce}^{3+}$ )

For measurements above 70 mT, two additional transitions have been observed as presented in figure 5.8:

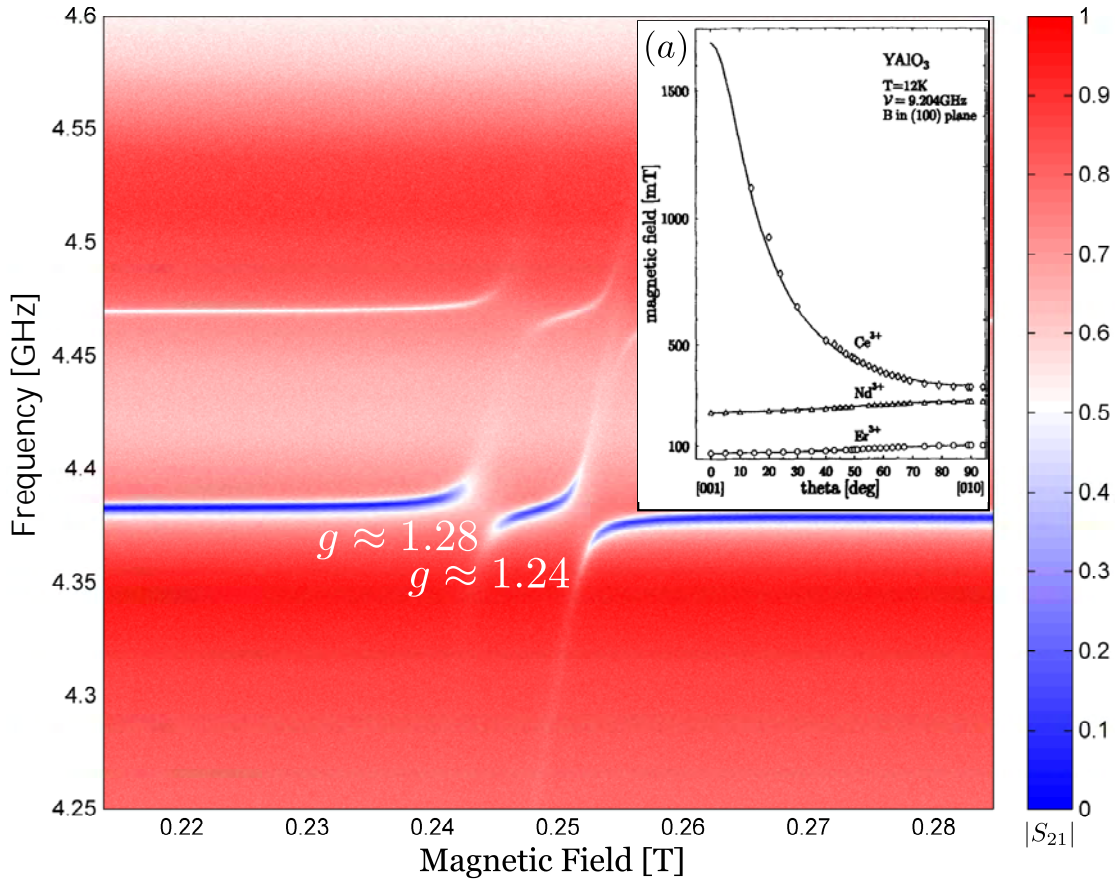


Figure 5.8.: Additional transitions far above 70 mT with g-factors 1.28 and 1.24 found at  $\approx 245$  mT and  $\approx 253$  mT, respectively. As two closely spaced main transitions are observed, indicating no hyperfine transitions, they could be associated with cerium  $\text{Ce}^{3+}$  as reported by Asatryan et al. [ARM97]. Furthermore, from the reported g-tensors for erbium and cerium [ARM97], such g-factors are only found for  $\text{Ce}^{3+}$ . Inset (a): g-factors for erbium ( $\text{Er}^{3+}$ ), neodymium ( $\text{Nd}^{3+}$ ) and cerium ( $\text{Ce}^{3+}$ ) as function of rotation angle  $\theta$  according to the applied static magnetic field for a resonator frequency of 9.204 GHz. Direction [001] corresponds to crystal axis  $b$  and [010] to  $a$ . g-factor values of  $\text{Ce}^{3+}$  depend also onto a deviation angle  $\alpha = 31.8^\circ$  from [100] direction. Inset (a) taken from [ARM97].

According to the published paper from Asatryan et al. [ARM97], the observed transitions with g-factors of  $g \approx 1.28$  and  $g \approx 1.24$  are most probably due to cerium ( $\text{Ce}^{3+}$ ) impurities. In the paper the g-tensor for  $\text{Ce}^{3+}$  was reported as  $g_x = 3.162$ ,  $g_y = 0.402$  and  $g_z = 0.395$  with an deviation angle of  $\alpha = 31.8^\circ$  of the magnetic axis  $x$  according to the crystallographic axis  $a$  or [100].

From inset (a) of figure 5.8, a g-factor of  $\approx 9.39$  is calculated for  $\text{Er}^{3+}$  at position  $\theta = 0^\circ$  if interpreting the plot correctly with a magnetic field of 70 mT and frequency 9.204 GHz. Such position<sup>1</sup> ([001]) corresponds to our crystal axis  $b$  (see e.g. figure 5.5), where we measured a g-factor of  $\approx 9.38$  for erbium. At  $\theta \approx 45^\circ$ , a g-factor of  $\approx 8.22$  is

<sup>1</sup> Pbnm space group representation: [100] =  $a$ , [010] =  $b$ , [001] =  $c$ . For interpretation of the [ARM97] data, the Pnma space group representation is equivalent to [100] =  $c$ , [010] =  $a$ , [001] =  $b$ . See Pbnm, Pnma space group discussion at [BSBS09].

calculated if adopting a magnetic field of 80 mT from inset (a). In our case we found for the same orientation a g-factor of  $\approx 8.37$ .

A g-factor of  $\approx 1.3$  is found for  $\text{Ce}^{3+}$  from inset (a) at  $\theta \approx 40^\circ$  corresponding to  $\approx 500$  mT if using the data from Asatryan et al. In our case this would correspond to  $\approx 250$  mT, as the probing frequency is approximately the half as used by Asatryan et al. [ARM97]. If taking the previously mentioned deviation angle of  $\alpha = 31.8^\circ$  into account, this could coincide with our crystal orientation as found in figure 5.5 (a).

Furthermore, Asatryan et al. reported in their paper that typically two main magnetically non-equivalent lines of  $\text{Ce}^{3+}$  exist without hyperfine structures due to zero nuclear spin isotopes [ARM97], as it is also observed in our case of figure 5.8. Further transition as e.g. according to  $\text{Nd}^{3+}$  (neodymium) have not been observed, which was different for Asatryan et al. (inset (a), figure 5.8). Usually such a transition would be identified by its hyperfine transitions due to odd isotopes  $^{143}\text{Nd}$  and  $^{145}\text{Nd}$  [ARM97] at higher magnetic fields.

According to this facts, we are sure to observe Cerium impurities at  $\approx 245$  mT, which also tolerates the g-tensor values reported by Asatryan et al. [ARM97].

## 6. Summary

---

Telecom C-band optical communication combined with modern superconducting quantum processing units are maybe the backbones of future quantum communication and quantum information processing. This requires coherent quantum converters interfacing optical and microwave frequencies. Erbium doped crystals have both transitions in the optical as well as in the microwave domain. Rare earth doped crystals serve as a quantum memory, whereas a resonator cavity is used as a bus between the crystal and the processing units. In order to coherently extract or provide quantum information, strong coupling is required between both devices and long coherence times are desired. Such times are determined by the environment of the spin ensemble.

The focus of this thesis lies on the investigation of a first version waveguide resonators, possessing a homogeneous oscillation magnetic field at approximately 7 GHz. The modes of the cavity have been calculated via numeric simulations. The resonator along with the erbium doped crystal was placed inside a cryostat, where temperatures around 25 mK have been reached. We used Electron Spin Resonance (ESR) spectroscopy to probe the electronic spin transitions. Strong coupling was not observed for version 1 of the waveguide resonator. This is why a new waveguide resonator (version 2) for additional ESR measurements was designed.

Compared to version 1, we reduced the resonance frequency of the  $TE_{011}$  mode to 5.5 GHz in order to access larger scanning ranges. Additionally, the frequency range to neighboring resonant modes was increased. The resonators loaded quality factor was reduced to match the spin linewidth of the spin ensemble. Using a 50 ppm erbium doped YSO crystal, several ESR measurements have been necessary in order to figure out the magnetic anisotropy of the crystal. With the measurement data it was possible to determine the proper crystal orientation using a self modified version of the simulation software EasySpin. Knowing the proper orientation, strong coupling of the waveguide resonator to the spin ensemble could be demonstrated.

Apart from the measurements with waveguide resonators, additional ESR spectroscopy using a 200 ppm erbium doped yttrium orthoaluminate crystal (Er:YAlO) was performed in combination with superconducting lumped element resonators. For this crystal we observed strong coupling for relatively small values of the static magnetic field. Additionally, at large static magnetic fields a cerium impurity was determined.



## 7. Conclusions and Outlook

---

The goal of this thesis was to show strong coupling between a waveguide resonator and an erbium spin ensemble. This was demonstrated using a highly over-coupled waveguide resonator filled with a 50 ppm erbium doped yttrium orthosilicate crystal (Er:YSO). The magnetic g-factors were determined from measurements combined with simulations. From the simulated data a crystal orientation of  $\theta \approx 70^\circ$  was determined for the  $D_2$ -b plane. Such an orientation possesses a large AC g-factor, which resulted in strong coupling with a coupling of approximately 21 MHz. The measurements were performed in the single photon regime as well as for photon numbers exceeding one million. Complementary, an inhomogeneous spin linewidth of approximately 18 MHz was observed. For instance, Probst et al. reported an even smaller linewidth for superconducting lumped element resonators coupled to an erbium spin ensemble [PRW<sup>+</sup>13].

The reason for larger values of the inhomogeneous spin linewidth could originate from the fact, that the complete volume of the crystal is penetrated by the magnetic field. Thus, the probability of crystal defects [TAC<sup>+</sup>10] contributing to the inhomogeneous spin linewidth rises proportional to the probed crystal volume. Furthermore, the local magnetic field may be disturbed by the rather large coupling coils.

In addition, strong coupling was demonstrated for erbium doped yttrium orthoaluminate crystal (Er:YAlO) coupled to a superconducting lumped element resonator. In case of Er:YAlO, temperature dependent measurements of the coupling strength showed that the coupling drops faster with increasing temperature as compared to the case of Er:YSO coupled to a waveguide resonator. In the latter case, strong coupling was observed up to a temperature of approximately 700 mK, whereas for Er:YAlO strong coupling was observed only up to approximately 100 mK.

Nevertheless, Er:YAlO could be a promising quantum memory candidate, because strong coupling was achieved using relatively low magnetic fields of about 33 mT. In case of Er:YSO, much larger magnetic fields are needed to enter the strong coupling regime ( $\approx 240$  mT). The fits yield a coupling strength of approximately 34.6 MHz and an inhomogeneous spin linewidth of 22 MHz using a superconducting lumped element resonator. Interestingly, an additional cerium impurity was observed.

The setup can be further extended by providing optical access through additional holes in the resonator. Thus, the demonstrated experiment is the first step towards a coherent quantum converter. Supplementary, the ESR experiments with Er:YAlO demonstrate the big potential of this crystal host, because smaller magnetic fields are needed.



# Bibliography

- [AB70] A. Abragam and B. Bleaney, *Electron Paramagnetic Resonance of Transition Ions*. Clarendon Press, Oxford, 1970.
- [AKN<sup>+</sup>11] R. Amsüss, C. Koller, T. Nöbauer, S. Putz, S. Rotter, K. Sandner, S. Schneider, M. Schramböck, G. Steinhauser, H. Ritsch, J. Schmiedmayer, and J. Majer, “Cavity qed with magnetically coupled collective spin states,” *Physical Review Letters*, 2011. [Online]. Available: <http://link.aps.org/doi/10.1103/PhysRevLett.107.060502>
- [ARM97] H. R. Asatryan, J. Rosa, and J. A. Mareš, “EPR studies of Er<sup>3+</sup>, Nd<sup>3+</sup> and Ce<sup>3+</sup> in YAlO<sub>3</sub> single crystals,” *Solid State Communications*, 1997. [Online]. Available: [http://dx.doi.org/10.1016/S0038-1098\(97\)00258-5](http://dx.doi.org/10.1016/S0038-1098(97)00258-5)
- [ASJ<sup>+</sup>13] M. Afzelius, N. Sangouard, G. Johansson, M. U. Staudt, and C. M. Wilson, “Proposal for a coherent quantum memory for propagating microwave photons,” *New Journal of Physics*, 2013. [Online]. Available: <http://dx.doi.org/10.1088/1367-2630/15/6/065008>
- [BFR<sup>+</sup>11] P. A. Bushev, A. K. Feofanov, H. Rotzinger, I. Protopopov, J. H. Cole, C. M. Wilson, G. Fischer, A. Lukashenko, and A. V. Ustinov, “Ultralow-power spectroscopy of a rare-earth spin ensemble using a superconducting resonator,” *Physical Review B*, 2011. [Online]. Available: <http://link.aps.org/doi/10.1103/PhysRevB.84.060501>
- [Boy08] R. W. Boyd, *Nonlinear Optics, 3rd Edition*. Academic Press, 2008.
- [BSBS09] M. G. Brik, I. Sildos, M. Berkowski, and A. Suchocki, “Spectroscopic and crystal field studies of YAlO<sub>3</sub> single crystals doped with Mn ions,” *Journal of Physics: Condensed Matter*, 2009. [Online]. Available: <http://dx.doi.org/10.1088/0953-8984/21/2/025404>
- [BSTC06] T. Böttger, Y. Sun, C. W. Thiel, and R. L. Cone, “Spectroscopy and dynamics of Er<sup>3+</sup>:Y<sub>2</sub>SiO<sub>5</sub> at 1.5  $\mu\text{m}$ ,” *Physical Review B*, 2006. [Online]. Available: <http://link.aps.org/doi/10.1103/PhysRevB.74.075107>
- [Col01] R. E. Collin, *Foundations for Microwave Engineering, 2nd Edition*. John Wiley & Sons, Inc. / IEEE Press Series on EM Theory, 2001.
- [CW08] J. Clarke and F. Wilhelm, “Superconducting quantum bits,” *Nature*, 2008. [Online]. Available: <http://dx.doi.org/10.1038/nature07128>
- [CW09] J. Colton and L. Wienkes, “Resonant microwave cavity for 8.5-12 ghz optically detected electron spin resonance with simultaneous nuclear magnetic resonance,” *Review of Scientific Instruments*, 2009. [Online]. Available: <http://dx.doi.org/10.1063/1.3095683>

- [DMN<sup>+</sup>08] S. Doyle, P. Mauskopf, J. Naylon, A. Porch, and C. Duncombe, “Lumped element kinetic inductance detectors,” *Journal of Low Temperature Physics*, Springer, 2008. [Online]. Available: <http://link.springer.com/article/10.1007%2Fs10909-007-9685-2>
- [DVA<sup>+</sup>08] M. D. Dramićanin, B. Viana, c. Andrić, V. Djoković, and A. S. Luyt, “Synthesis of  $\text{Y}_2\text{SiO}_5:\text{Eu}^{3+}$  nanoparticles from a hydrothermally prepared silica sol,” *Journal of Alloys and Compounds*, 2008. [Online]. Available: <http://dx.doi.org/10.1016/j.jallcom.2007.09.135>
- [Eic13] M. Eichhorn, *Laserphysik*. Springer Spektrum, 2013.
- [FLS64] R. Feynman, R. Leighton, and M. Sands, *Lectures on Physics Volume 2*. Addison-Wesley Publishing Company, INC., 1964.
- [Fox06] M. Fox, *Quantum Optics, An Introduction*. Oxford University Press, 2006.
- [GNBG<sup>+</sup>06] O. Guillot-Noël, E. Baldit, P. Goldner, P. Monnier, Y. L. Du, and K. Bencheikh, “Hyperfine interaction of  $\text{Er}^{3+}$  ions in  $\text{Y}_2\text{SiO}_5$ : An electron paramagnetic resonance spectroscopy study,” *Physical Review B*, 2006. [Online]. Available: <http://link.aps.org/doi/10.1103/PhysRevB.74.214409>
- [GT07] N. Gisin and R. Thew, “Quantum communication,” *Nature Photonics*, 2007. [Online]. Available: <http://dx.doi.org/10.1038/nphoton.2007.22>
- [Hil09] D. A. Hill, *Electromagnetic Fields in Cavities: Deterministic and Statistical Theories*. John Wiley & Sons, Inc. / IEEE Press Series on EM Theory, 2009.
- [HTS<sup>+</sup>05] J. G. Hartnett, M. E. Tobar, P. L. Stanwix, T. Morikawa, D. Cros, and O. Piquet, “Designs of a microwave te<sub>011</sub> mode cavity for a space borne h-maser,” *Transactions on ultrasonics, ferroelectrics and frequency control, IEEE*, 2005. [Online]. Available: <http://dx.doi.org/10.1109/TUFFC.2005.1561619>
- [Ima09] A. Imamoglu, “Cavity qed based on collective magnetic dipole coupling: Spin ensembles as hybrid two-level systems,” *Physical Review Letters*, 2009. [Online]. Available: <http://dx.doi.org/10.1103/PhysRevLett.102.083602>
- [KCAGK99] D. Kajfez, S. Chebolu, M. R. Abdul-Gaffor, and A. A. Kishk, “Uncertainty analysis of the transmission-type measurement of q-factor,” *Transactions on microwave theory and techniques, IEEE*, 1999. [Online]. Available: <http://dx.doi.org/10.1109/22.750244>
- [KDT<sup>+</sup>99] J. Krupka, K. Derzakowski, M. Tobar, J. Hartnett, and R. G. Geyer, “Complex permittivity of some ultralow loss dielectric crystals at cryogenic temperatures,” *Measurement Science and Technology*, 1999. [Online]. Available: <http://dx.doi.org/10.1088/0957-0233/10/5/308>
- [Kim08] H. Kimble, “The quantum internet,” *Nature*, 2008. [Online]. Available: <http://dx.doi.org/10.1038/nphoton.2007.22>
- [Kit96] C. Kittel, *Introduction to Solid State Physics, 7<sup>th</sup> Edition*. John Wiley & Sons, New York, 1996.
- [KKS<sup>+</sup>12] M. Kinoshita, H. Kinouchi, M. Shaiful Bin Abdul Karim, K. Wakino, and T. Kitazawa, “A method of evaluating high-permittivity and lossy materials using a cylindrical cavity based on hybrid electromagnetic theory,” *Japanese Journal of Applied Physics*, 2012. [Online]. Available: <http://jjap.jsap.jp/link?JJAP/51/09LF03/>

- [LLC85] C. S. Lee, S. W. Lee, and S. L. Chuang, "Plot of modal field distribution in rectangular and circular waveguides," *Microwave Theory and Techniques, IEEE*, 1985. [Online]. Available: <http://dx.doi.org/10.1109/TMTT.1985.1132998>
- [LM02] K. Leong and J. Mazierska, "Precise measurements of the q factor of dielectric resonators in the transmission mode - accounting for noise, crosstalk, delay of uncalibrated lines, coupling loss and coupling reactance," *Transactions on microwave theory and techniques, IEEE*, 2002. [Online]. Available: <http://dx.doi.org/10.1109/TMTT.2002.802324>
- [Ort68] J. Orton, *Electron Spin Resonance: An Introduction to Transition Group Ions in Crystals*. London ILIFFE Books LTD, 1968.
- [Pob07] F. Pobell, *Matter and Methods at Low Temperatures, 3rd Edition*. Springer, 2007.
- [Poo67] C. Poole, *Electron Spin Resonance*. John Wiley and Sons, 1967.
- [Poz11] D. M. Pozar, *Microwave Engineering, 4th Edition*. John Wiley & Sons, Inc., 2011.
- [Pro13] S. Probst, "Erbium doped crystal coupled to a copper transmission line resonator," private communication, November 2013.
- [PRW<sup>+</sup>13] S. Probst, H. Rotzinger, S. Wünsch, P. Jung, M. Jerger, M. Siegel, A. V. Ustinov, and P. A. Bushev, "Anisotropic rare-earth spin ensemble strongly coupled to a superconducting resonator," *Physical Review Letters*, 2013. [Online]. Available: <http://link.aps.org/doi/10.1103/PhysRevLett.110.157001>
- [RdS<sup>+</sup>13] V. Ranjan, G. de Lange, R. Schutjens, T. Debelhoir, J. P. Groen, D. Szombati, D. J. Thoen, T. M. Klapwijk, R. Hanson, and L. DiCarlo, "Probing dynamics of an electron-spin ensemble via a superconducting resonator," *Physical Review Letters*, 2013. [Online]. Available: <http://link.aps.org/doi/10.1103/PhysRevLett.110.067004>
- [SBTC08] Y. Sun, T. Böttger, C. Thiel, and R. L. Cone, "Magnetic g tensor for the  $^4I_{15/2}$  and  $^4I_{13/2}$  states of  $\text{Er}^{3+}:\text{Y}_2\text{SiO}_5$ ," *Physical Review B*, 2008. [Online]. Available: <http://link.aps.org/doi/10.1103/PhysRevB.77.085124>
- [SG08] R. J. Schoelkopf and S. M. Girvin, "Wiring up quantum systems," *Nature*, 2008. [Online]. Available: <http://www.nature.com/nature/journal/v451/n7179/pdf/451664a.pdf>
- [SMM05] R. Serway, C. Moses, and C. Moyer, *Modern Physics 3rd Edition*. Brooks/Cole - Thomson Learning, 2005.
- [SRA<sup>+</sup>12] K. Sandner, H. Ritsch, R. Amsüss, C. Koller, T. Nöbauer, S. Putz, J. Schmiedmayer, and J. Majer, "Strong magnetic coupling of an inhomogeneous nitrogen-vacancy ensemble to a cavity," *Physical Review A*, 2012. [Online]. Available: <http://link.aps.org/doi/10.1103/PhysRevA.85.053806>
- [SS06] S. Stoll and A. Schweiger, "EasySpin, a comprehensive software package for spectral simulation and analysis in epr," *Journal of Magnetic Resonance*, 2006. [Online]. Available: <http://dx.doi.org/10.1016/j.jmr.2005.08.013>

- [SSG<sup>+</sup>10] D. I. Schuster, A. P. Sears, E. Ginossar, L. DiCarlo, L. Frunzio, J. J. L. Morton, H. Wu, G. A. D. Briggs, B. B. Buckley, D. D. Awschalom, and R. J. Schoelkopf, “High-cooperativity coupling of electron-spin ensembles to superconducting cavities,” *Physical Review Letters*, 2010. [Online]. Available: <http://link.aps.org/doi/10.1103/PhysRevLett.105.140501>
- [TAC<sup>+</sup>10] W. Tittel, M. Afzelius, T. Chanelière, R. L. Cone, S. Kröll, S. A. Moiseev, and M. Sellars, “Photon-echo quantum memory in solid state systems,” *Laser & Photonics Reviews*, 2010. [Online]. Available: <http://onlinelibrary.wiley.com/doi/10.1002/lpor.200810056/pdf>
- [TF85] R. C. Taber and C. A. Flory, “Microwave oscillators incorporating cryogenic sapphire dielectric resonators,” *Transactions on ultrasonics, ferroelectrics and frequency control, IEEE*, 1985. [Online]. Available: <http://dx.doi.org/10.1109/58.368306>
- [VMRT03] I. P. Vadeiko, G. P. Miroshnichenko, A. V. Rybin, and J. Timonen, “Algebraic approach to the Tavis-Cummings problem,” *Physical Review A*, 2003. [Online]. Available: <http://link.aps.org/doi/10.1103/PhysRevA.67.053808>
- [WHK<sup>+</sup>11] S. Wünsch, G. Hammer, T. Kappler, F. Geuppert, and M. Siegel, “Investigation and optimization of leaky coupling structures and multi-pixel arrays at 4.2 K,” *Transactions on Applied Superconductivity, IEEE*, 2011. [Online]. Available: <http://dx.doi.org/10.1109/TASC.2010.2090445>
- [WM08] D. F. Walls and G. J. Milburn, *Quantum Optics, Second Edition*. Springer, 2008.
- [ZL08] K. Zhang and D. Li, *Electromagnetic Theory for Microwaves and Optoelectronics, 2nd Edition*. Springer, 2008.

# Appendix

## A. CST Microwave Studio (Simple Manual)

In this appendix we will shortly introduce and explain how to use CST Microwave Studio for simulations according to the electromagnetic behavior of 3D cavities (Hohlraum-Resonators). For demonstration purposes we use the copper cavity (waveguide resonator) version 2 as used in this thesis.

When creating a new project with CST Studio Suite, in version 2012 simply the category **Resonator** is used, providing all necessary settings. For version 2013 an additional user interface is presented, where presumably **Microwaves & RF**, **Circuit & Components** and **Waveguide & Cavity Filters** have to be chosen. Finally the proper solver has to be used, which is the **Eigenmode-Solver**.

In order to design now the cavity, we start with the brick tool as shown in figure A.1 (tool-box, red frame) and define the origin of the coordinate system first. Next, the desired dimensions of the overall cavity are defined, where from the materials library the specific material of the brick is selected, being in our case copper. Up to now the brick is completely filled with copper (figure A.1 (a)). To create a Hohlraum-Resonator out of the brick, additional tools like the cylinder tool (in the same row as the brick tool) are used. Moving to the **Transform WCS** button (figure A.1, blue frame), the origin of the coordinate system indicated by  $u$ ,  $v$  and  $w$  has to be changed. Thus, to create a cylindrical cavity inside the copper brick, the origin of the coordinate system is placed inside of the cubed model. After setting the dimensions of the cylinder, the program will ask if the defined region has to be cut out. We confirm this inquiry and replacement of the old material via a new one, e.g. vacuum.

A cross section through the copper brick enables the view to the cavity, where for this purpose the tab **View** is selected and the button **Cutting Plane** is enabled (figure A.1 (b), green frame). Furthermore, arbitrary orientations of the model could be defined using the additional tools of the **View** tab.

To fill the cavity with additional materials, like e.g. dielectrics, the same procedure as previously described could be used. For example, define the origin of the coordinate system to the desired position and select a tool from the tool-box as e.g. the cylindrical tool. Define the dimensions and replace the current material using a new one as e.g. sapphire. Figure A.1 demonstrates the cross section through the copper brick, where we replaced the copper material by other materials like sapphire, teflon and vacuum or air using the steps described previously.

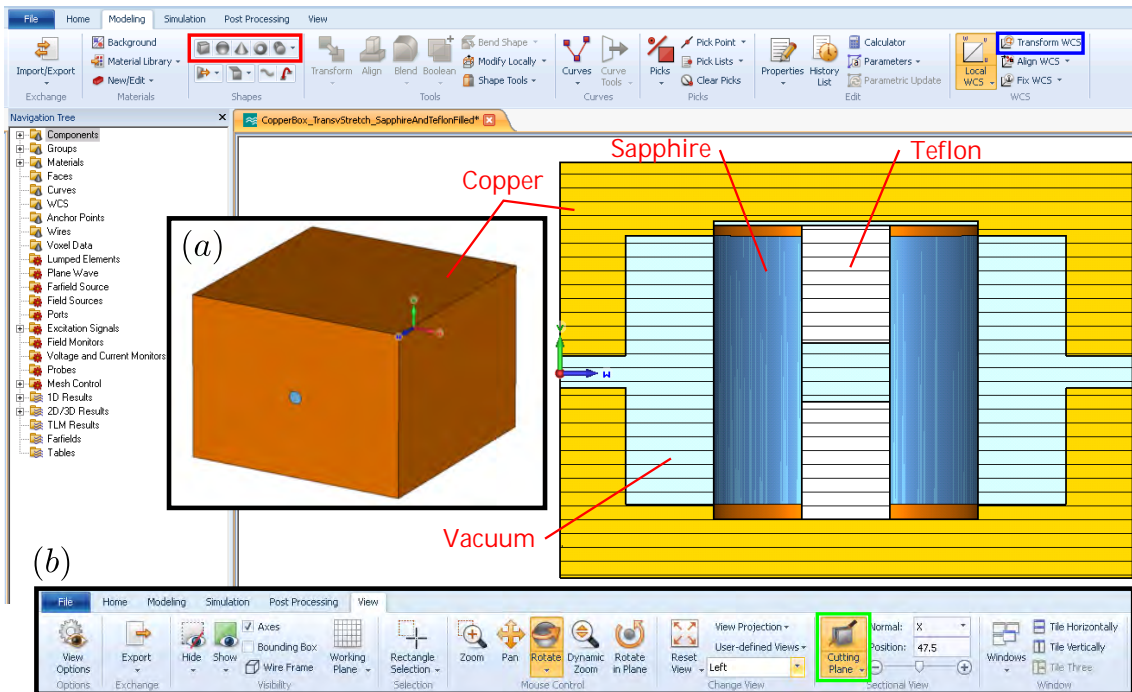


Figure A.1.: CST Microwave Studio user interface. The yellow box is the cross section of a copper cavity filled with sapphire, teflon and vacuum or air. (a) shows the bulk copper brick. Different shapes can be modeled using the tool-box (red frame) as found from the **Modeling** tab. (b) **View** tab, which is used to define and adjust different orientations of the model.

In case of the used material sapphire, no default entry was found. Thus, from the **Modeling** tab again, such a material could be defined by the user (figure A.2, red frame):

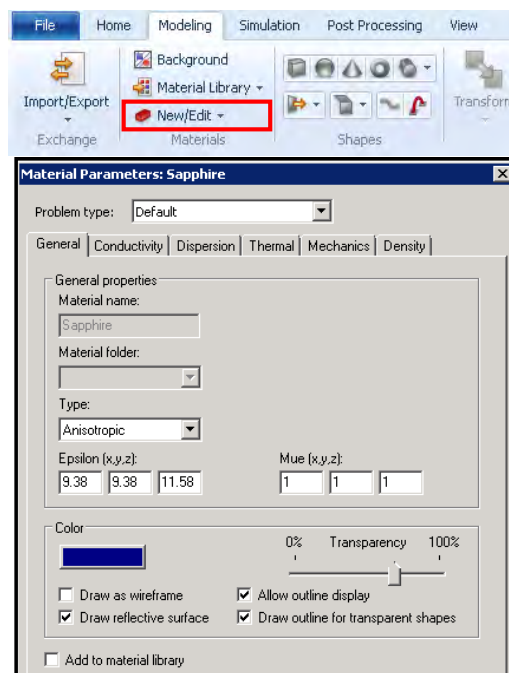


Figure A.2.: CST Microwave Studio material parameters. Using the **Modeling** tab, new materials could be defined via the **New/Edit** button (red frame). At the material parameters window, the desired properties of the material could be defined (e.g. sapphire).

If for example defining an anisotropic material, the coordinate system ( $x, y$  and  $z$ ) has to be correlated with the used values defining the anisotropy in the respective direction, or vice versa.

For the simulation of the corresponding resonant frequencies of the cavity, we change to the **Simulation** tab:

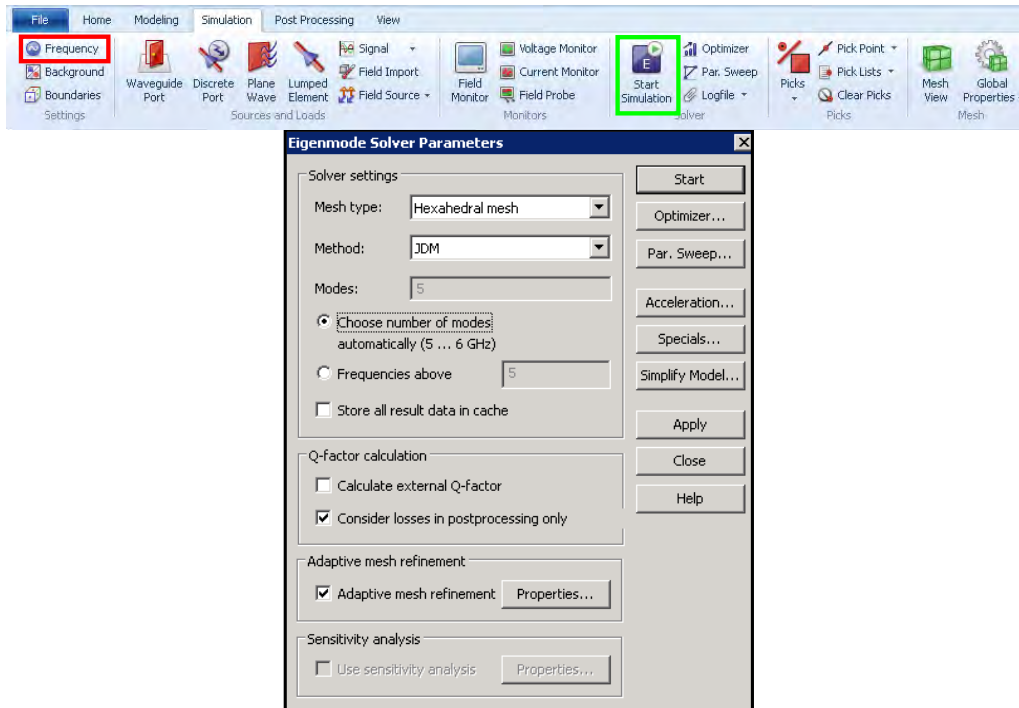


Figure A.3.: CST Microwave Studio **Simulation** tab. The desired frequency range for the simulation can be defined via the **Frequency** button (red frame), whereas additional simulation parameters (gray window) are enabled via the **Eigenmode Solver** button (green frame). Simulations using the JDM Method are recommended as well as the adaptive mesh refinement or the postprocessing loss calculations.

The upper part of figure A.3 shows the **Simulation** tab, where first of all the desired frequency range for the simulation is defined (red frame). By clicking onto the **Start Simulation** button (green frame), the eigenmode solver window is enabled. A recommended way according to the simulations is the usage of the JDM Method. Using JDM, the number of modes will be selected automatically in the defined frequency range. In order to speed up the calculations, losses should be only considered for postprocessing. The usage of the adaptive mesh refinement is recommended, but could also be adjusted by the user from the **Simulation** tab. All other parameters can be used as default, when starting the simulation with the start button.

After the simulation finished successfully, the corresponding resonant frequencies are found at the navigation tree (figure A.4, blue frame). Every mode is separated in its electric (e) and magnetic (h) field components. By clicking onto the corresponding folder (e or h), the field distribution is indicated by arrows inside the cavity. The color of the arrow represents the field strength, whereas the resonance frequency is found at the inset of the model window (figure A.4, red frame).

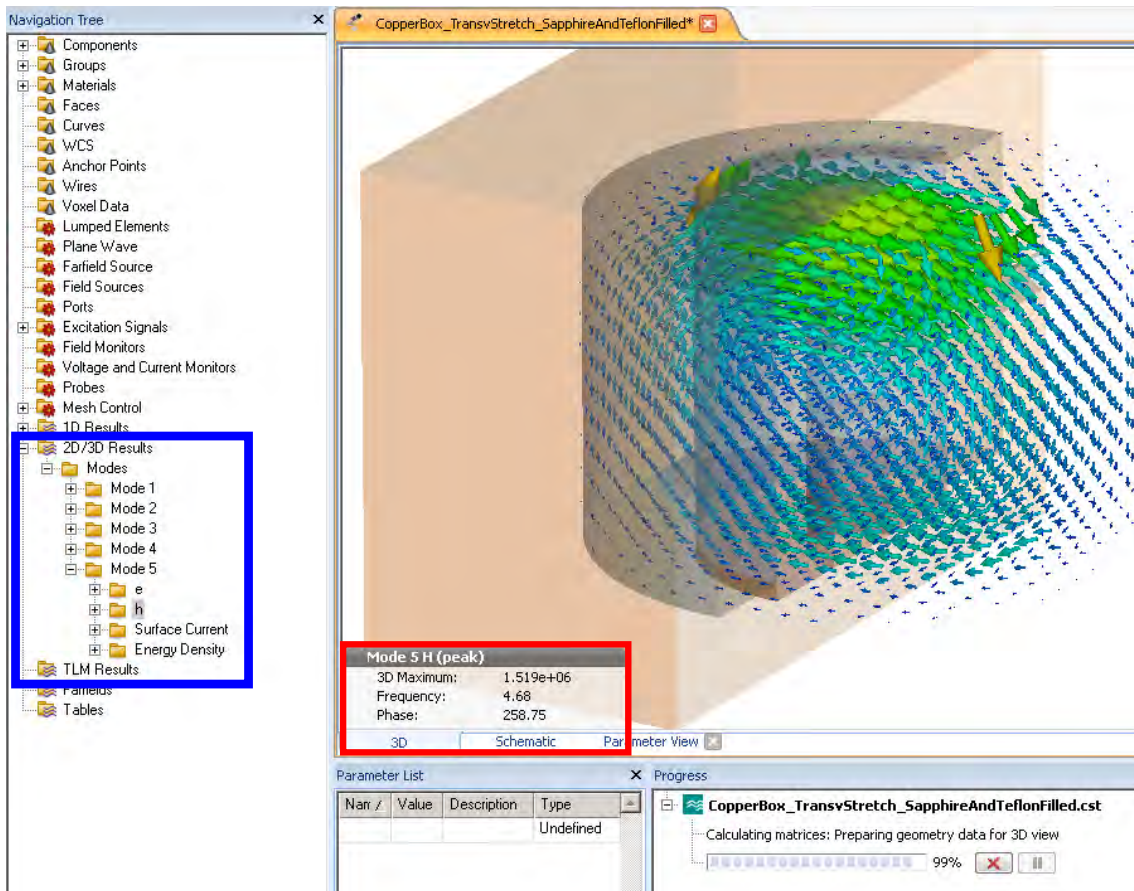


Figure A.4.: CST Microwave Studio simulation of an eigenmode with the corresponding magnetic field contributions. The simulated eigenmodes are found at the navigation tree (blue frame) for a predefined frequency range. Every mode folder contains the electric and magnetic field contributions of the resonance. The resonant frequency is observed from the inset (red frame).

Right clicking on the corresponding folder for the electric (e) or magnetic (h) field enables further settings as e.g. the animation of the field distribution or additional plot properties. It is also possible to store the animations as gif data or a movie. For this purpose the **Home** tab in combination with the **Macro** button is used. From the drop down menu we then use **Report and Graphics, save Video**.

In order to go further into details using CST, the help section is highly recommended. This section provides additional training proposals as start-up videos or tutorials with simple examples.

## B. Design Drawings of Waveguide Resonator Version 1

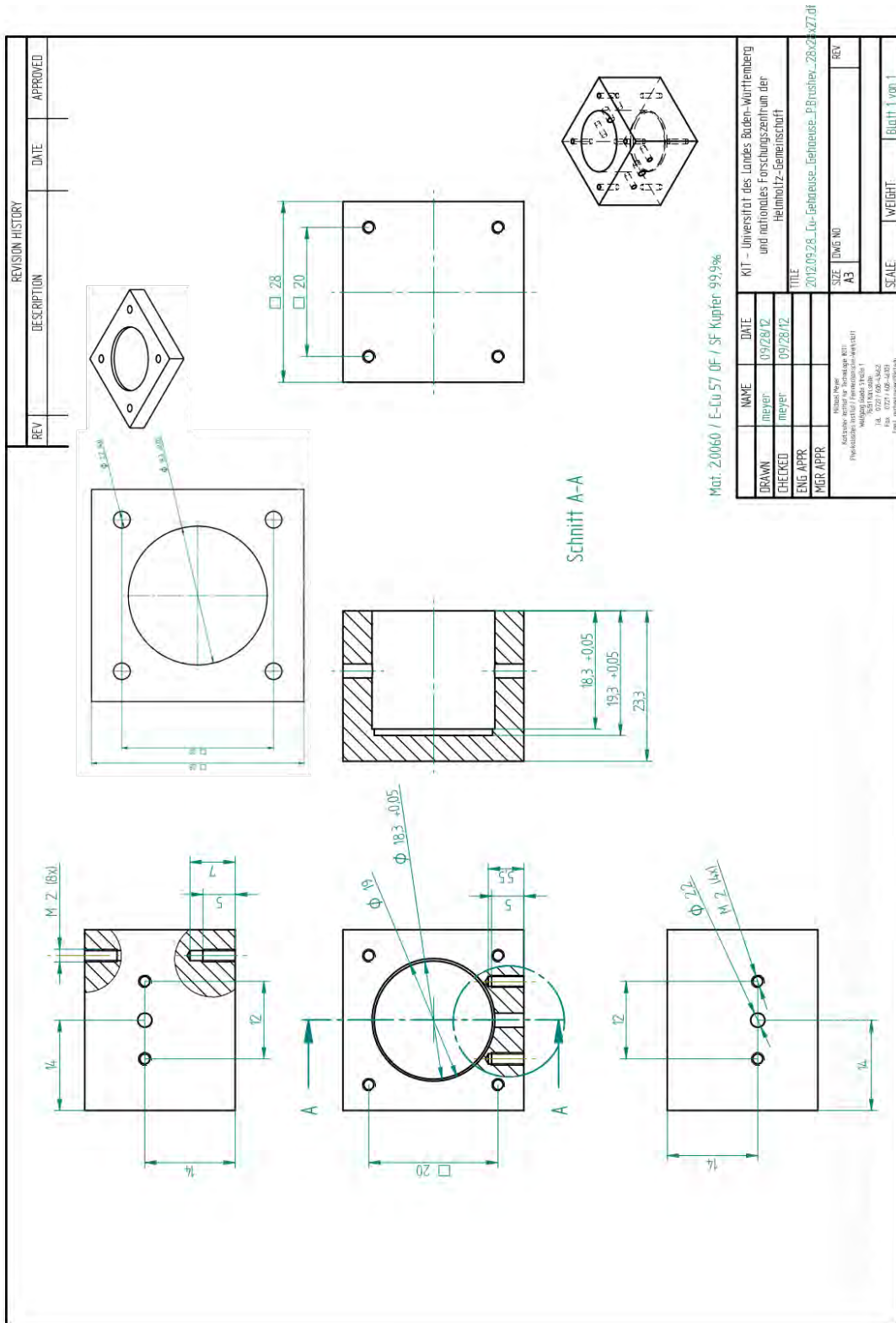


Figure B.5.: Shop drawings of waveguide resonator version 1



## D. Design Drawing of the Sample Holder

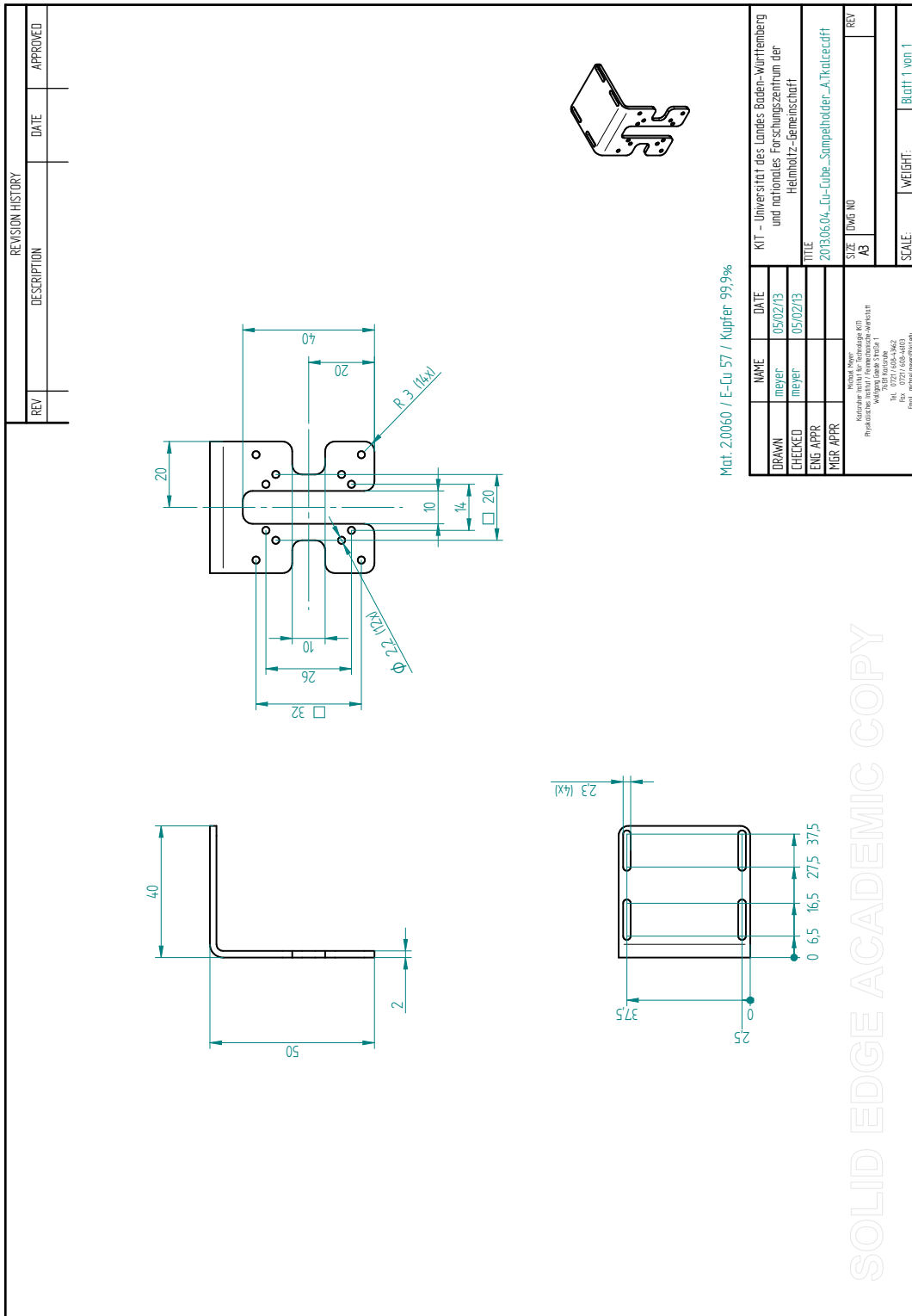


Figure D.7.: Shop drawings of the sample holder as used for the waveguide resonators



## 8. Acknowledgments

---

I would like to thank Prof. Alexey Ustinov for having me as a student in his group. It was a big pleasure for me to work together with excellent physicists on a very interesting topic.

Prof. Pavel Bushev earns my thanks for motivating me in his lecture to learn more about his field of research. His kindness and the way of teaching physics affected my decision to start my master thesis in Prof. Ustinovs' group. Pavel always helped and supported me during my work and did not hesitate to explain and answer me every question I asked.

I would also like to thank Sebastian Probst for his helping hands in experiments and revealing physical discussions. He introduced me to the experimental setups in detail and he was always at hand for additional questions. His ambition, suggestions and support highly motivated and pushed me during my thesis.

Furthermore, I would like to thank Daniel Rieger for giving me a helping hand on assembling and disassembling the cryostat during my cool down marathon. He was a very nice and funny workmate. I would like to express my gratitude to the whole 'Fluxon' group for a convenient working atmosphere and very interesting presentations in the coffee room. Special thanks contribute to Dr. Hannes Rotzinger for giving me some helpful advices. I also have to say thanks to Michael Meyer and this group at the workshop for manufacturing the waveguide resonator and for supporting me with shop drawings.

Finally, I like to thank my brother and my parents for believing in me and supporting me throughout my studies. Especially I would like to thank my beautiful girlfriend for highly supporting me during my studies. She never complained that I have to spend my weekends with Karoline (the name of the cryostat) rather than with her.